Worcester Polytechnic Institute
Digital WPI

Major Qualifying Projects (All Years) | Major Qualifying Projects

April 2019

Design, Realization, and Application of an Ultra-High-Speed Shock Tube for Middle-Ear Mechanics

Eli Wonnacott Frank
Worcester Polytechnic Institute

Jacquelyn Yvette Roberge
Worcester Polytechnic Institute

Jessica Catherine Walsh
Worcester Polytechnic Institute

John Joseph Perkoski
Worcester Polytechnic Institute

Follow this and additional works at: https://digitalcommons.wpi.edu/mqp-all

Repository Citation
Frank, E. W., Roberge, J. Y., Walsh, J. C., & Perkoski, J. J. (2019). *Design, Realization, and Application of an Ultra-High-Speed Shock Tube for Middle-Ear Mechanics*. Retrieved from https://digitalcommons.wpi.edu/mqp-all/7128

This Unrestricted is brought to you for free and open access by the Major Qualifying Projects at Digital WPI. It has been accepted for inclusion in Major Qualifying Projects (All Years) by an authorized administrator of Digital WPI. For more information, please contact digitalwpi@wpi.edu.

Design, Realization, and Application of an Ultra-High-Speed Shock Tube for Middle-Ear Mechanics

Major Qualifying Project: CF-IRP-2019

Submitted to the Faculty of:
Worcester Polytechnic Institute

In Partial Fulfillment of the
Degree of Bachelor of Science

By

Eli Frank
John Perkoski
Jacquelyn Roberge
Jessica Walsh

Date: April 25, 2019

Approved:

_____

Professor Cosme Furlong

WPI

Massachusetts Eye and Ear

Abstract

The Tympanic Membrane (TM) is an important middle-ear structure that is highly susceptible to trauma due to environmental changes and acoustic pressures, yet minimal investigations have been conducted on its fracture mechanics. WPI researchers, in collaboration with Massachusetts Eye and Ear, are conducting advanced research toward understanding the TM fracture mechanics in real-time by using 3D Quantitative High-Speed Optical techniques. In this project, we designed, constructed, and characterized an ultra-high-speed Shock Tube to produce controlled acoustic shock waves, enabling us to perform accurate and repeatable investigations on the mechanics of the TM at high loading rates. Rankine-Hugoniot relations and computational fluid dynamics were applied to design and predict the behavior of the apparatus, while a series of high-frequency pressure sensors were adapted into the system to record and confirm the computational results. High-speed cameras operating at >35,000fps were incorporated with Schlieren photography methods to image the density differentiation of the produced acoustic pressure waves. The developed apparatus and methods were validated through rupture tests on known samples, and finally applied to actual human TMs to study ear damage by high level sound.

Acknowledgements

We would like to thank all the members of Massachusetts Eye and Ear, specifically J.T. Cheng and John Rosowski, for their guidance and support throughout this project. We also would like to thank our advisor to this project, Professor Cosme Furlong, for helping to bring this project to fruition. Finally, we would like to thank all of the WPI professors and faculty who have assisted us in every endeavor.

Our group also recognizes the following individuals for contributing to the quality and overall success of this project:

Professor Adriana Hera
Professor Brian Savilonis
Peter Hefti
Barbara Fuhrman
Haimi Tang
Anthony Salerni
Daniel Ruiz-Cadalso
Koohyar Pooladvand

Authorship

All team members contributed equally to this project

Copyright © 2019

By Eli Frank, John Perkoski, Jacquelyn Roberge, and Jessica Walsh

CHSLT – Center for Holographic Studies and Laser micro-mechaTronics

Mechanical Engineering Department

Worcester Polytechnic Institute

Worcester, MA 01609-2280

All rights reserved

Table of Contents

Abstract 1

Acknowledgements 2

Authorship 2

Table of Contents 3

List of Figures 6

Objective 9

1. Introduction 9

2. Background 11
    2.1. Sound Waves 11
    2.2. Hearing Mechanics of the Human Ear 11
    2.3. Decibels and Sound Pressure Level 13
    2.4. Experimental Tympanic Membrane Research 14
        2.4.1. Shock Waves 14
        2.4.2. Shock Tubes 16
        2.4.2. Shock Tubes in Research 18

3. Methodology 21
    3.1. Use of Schlieren Techniques to Visualize Acoustic Pressure 21
    3.2. Characterization of Initial WPI System 24
    3.3. Design 29
        3.3.1. Functional Specifications and Constraints 30
        3.3.2. Numerical Methods 30
        3.3.3. Design 31
        3.3.4. ANSYS Fluent Simulation 32
    3.4. Shock Tube Realization 36
    3.5. Experimental Configuration 37
        3.5.1. Pressure Recording 37
        3.5.2. Data Acquisition 39

4. Results 43
    4.1. Experimental Results for Shock Tube Characterization 43
    4.2 ANSYS Results for Shock Tube Validation 46
    4.3. PFA Analysis for Thermodynamic Validation 48
    4.4. Study of Shock Tube Application to an Artificial Membrane 49
    4.5. Study of Shock Tube Application to a Cadaver Membrane 50

5. Discussion 53

6. Conclusion and Recommendations for Future Work 56

7. References 58

8. Appendix 61
Appendix A: 61
Compressible Flow Experiment 61
Numerical Modeling in Matlab 61
Theoretical ANSYS Simulation 63
Conducting Compressible Flow Experiment 66
MatLAB Simulation of Compressible Flow 68
Appendix B: Safety Protocol 73
Appendix C: CAD of Diaphragm Mount 75
Appendix D: Diaphragm Insertion Instructions 77
Appendix E: LabVIEW of Pressure Calibration 80
Appendix F: Shock Tube Labview Code 86
Appendix G: Operating Procedure 89

List of Figures

Figure 1. Sound wave 11

Figure 2. Anatomy of the inner ear 12

Figure 3. Uncoiled cochlea and basilar membrane 13

Figure 4: Normal shock wave 15

Figure 5. Friedlander waveform 16

Figure 6. Shock Tube anatomy 17

Figure 7. Position, velocity, pressure, and temperature behavior within the Shock Tube 18

Figure 8. Shock wave pressure vs time graphs 19

Figure 9. Shock wave characteristics 20

Figure 10. Single mirror Schlieren setup 22

Figure 11. Schlieren setup consisting of point light source, DSLR camera, and razor blade held with fixtures to table and projected on 10 inch mirror 120 inches away 23

Figure 12. Schlieren image of a hair dryer 24

Figure 13. Schlieren image of a hair dryer against a board 24

Figure 14. Main pressure delivery system 25

Figure 15. Sound wave mechanism 25

Figure 16. Sound wave mechanism Schlieren photography setup 26

Figure 17. Schlieren photography of the acoustic wave produced by a horn 27

Figure 18. PCB pressure vs time graph for the sound pressure mechanism 28

Figure 19. Pressure Difference Mechanism 28

Figure 20. Inline pressure vs time for pressure difference mechanism 29

Figure 21. Diaphragm and flange mount schematic 30

Figure 22. 2D axisymmetric model 32

Figure 23. 2D axisymmetric revolve feature 33

Figure 24. 2D axisymmetric mesh, end of Shock Tube 34

Figure 25. 2D axisymmetric mesh boundary conditions 34

Figure 26. Shock Tube driving and driven lengths 36

Figure 27. Experimental Shock Tube configuration 37

Figure 28. Experimental schematic with sampling and Schlieren imaging configuration 37

Figure 29. Pressure sensor placement 38

Figure 30. Static pressure transducer wiring diagram 38

Figure 31. Electronic wiring diagram 40

Figure 32. Labview front panel input characteristics 40

Figure 33. Labview front panel 41

Figure 34. Shock tube Schlieren configuration 42

Figure 35. P1 driving static pressure vs time 43

Figure 36. P3 static pressure vs time 35 mm inside the shock tube 44

Figure 37. P4 stagnation pressure vs time 50 mm outside the shock tube 45

Figure 38. P4 stagnation pressure vs time 100 mm outside the shock tube 46

Figure 39. ANSYS Fluent initial conditions 47

Figure 40. Pressure vs time for experimental and ANSYS 35 mm inside tube 47

Figure 41. Pressure vs time for experimental and ANSYS 50 mm outside the tube 48

Figure 42. PFA software tracking the speed of a shockwave 49

Figure 43. Teflon test setup 50

Figure 44. Teflon tape sample rupture sequence 50

Figure 45. Experimental TM setup with DIC 51

Figure 46. Ruptured TM sample 51

Figure 47. TM secured with reconfigured putty and clamp system 52

Figure 48. TM excitation 50 mm from end of shock tube 52

Figure 49. Experimental comparison to theoretical Friedlander waveform 53

Figure 50. Experimental and computational results compared with Schlieren 54

Figure 51. Schlieren diagram of a shock exiting a shock tube 55

Figure 52. New sample rupturing configuration 57

Objective

To design, construct, and characterize an acoustic loading apparatus to deliver a known and controlled transient acoustic force, representative of a blast, in order to enable accurate and repeatable investigations on the mechanics of the Tympanic Membrane at high loading rates.

1. Introduction

Human hearing mechanics are complicated, requiring the synchronized movement of multiple components within the ear. The Tympanic Membrane (TM) is one of the most important components in hearing mechanics and is also the most susceptible to trauma, yet there is little understanding of its real time fracture mechanics. Damage of the TM is often due to intense sound pressure exposure, leading to a condition known as Noise Induced Hearing Loss (NIHL). NIHL can affect everyone, from military personnel who are exposed to loud weapons and IEDs, to civilians in industry who are exposed to loud machinery.

The increased use of improvised explosive devices (IED) in warfare has subsequently increased the number of blast related hearing injuries in active military personnel. A study conducted by the U.S. Army Center for Health Promotion and Preventative Medicine found that over 60% of wounded-in-action service members have Tympanic Membrane damage, tinnitus, and/or hearing loss (Hefler, Jordan, & Lee, 2005). Damage to the Tympanic Membrane can cause acute hearing loss, pain, and dizziness, and while some Tympanic Membrane injuries can spontaneously heal overtime, permanent hearing loss can also occur. Hearing loss in veterans is not only a personal issue, but also an economic issue. In 2006, there were over 800,000 veterans receiving compensation for service related hearing loss and tinnitus, totaling in over one billion dollars (Saunders & Griest, 2009).

Civilians in construction, logging, mining, and farming are also at risk for Noise Induced Hearing Loss due to the loud nature of their professions. In 2001, over 30 million workers were paid over 240 million dollars in annual disability payments due to Noise Induced Hearing Loss (Saunders & Griest, 2009). Outside of the workplace, civilians can be exposed to dangerous levels of acoustic pressure without realization. Police sirens measure 97 dB SPL inside of the vehicle, jack hammers measure 100 dB SPL one meter away, and night clubs can measure upwards of 103 dB SPL one meter away from the speakers. While these sounds are not loud enough to rupture the TM, exposure to them is often spread out over a longer period of time, which gradually deforms the Tympanic Membrane, permanently shifting one's threshold of hearing (Young, Freedman, & Ford, 2016).

The Occupational Safety and Health Administration, Mine Safety and Health Administration, Federal Railroad Administration, and Department of Defense created regulations in attempt to lower NIHL

in the workplace, however these regulations are often ineffective, and do not fully address safety concerns (Saunders & Griest, 2009). Until the fracture mechanics of the Tympanic Membrane are characterized and better hearing protective devices are created, NIHL will continue to drastically alter the lives of those affected, costing individuals their sense of hearing and taxpayers millions of dollars in disability payments.

Previous studies on the rupture of the Tympanic Membrane have been conducted to determine the mechanical properties of the Tympanic Membrane. While these studies were successful, the analysis of the Tympanic Membrane was done after the rupture occurred. This analysis neglects the effect of crack initiation and propagation in the Tympanic Membrane and the frequency response of the Tympanic Membrane.

The Center for Holographic Studies and micro-mechaTronics (CHSLT) at Worcester Polytechnic Institute in partnership with Massachusetts Eye and Ear (MEE) are using full-field-of-view 3D High-Speed Digital Image Correlation (3D-HSDIC) to record the movement of the Tympanic Membrane in real time. The results show the strain rate and displacement of the Tympanic Membrane from initial loading to complete rupture and will be used to characterized the mechanical properties of the Tympanic Membrane.

The goal of this project is to develop an acoustic loading apparatus to deliver transient acoustic forces capable of rupturing a human cadaver Tympanic Membrane sample. The acoustic forces will be accurate, repeatable, and representative of the sounds that damage human Tympanic Membranes in the workplace and in military combat. Our loading apparatus will be used in conjunction with the CHSLT's 3D-HSDIC system to enable the accurate and repeatable investigations on the mechanics of the TM at high loading rates. These investigations will be used to understand how to create more effective hearing protection to protect military personnel and civilians from NIHL and Tympanic Membrane rupture.

2. Background

2.1. Sound Waves

The hearing process begins when sound waves enter the outer ear. Sound waves are longitudinal mechanical waves that create compressed sections of high pressure and rarefaction sections of low pressure along the direction of propagation, shown in Figure 1. There are multiple ways to quantify the sound pressure of a sound wave: static pressure, dynamic pressure, and stagnation pressure. Static pressure is the pressure of a wave or a fluid with reference to the atmospheric pressure. Dynamic pressure is the pressure associated with the kinetic energy of a wave or a fluid. Stagnation pressure is the pressure felt when a moving fluid is brought to rest, or when all of the kinetic energy is transferred to pressure. The three pressure measurements are related by Equation 1 (Sengpiel).

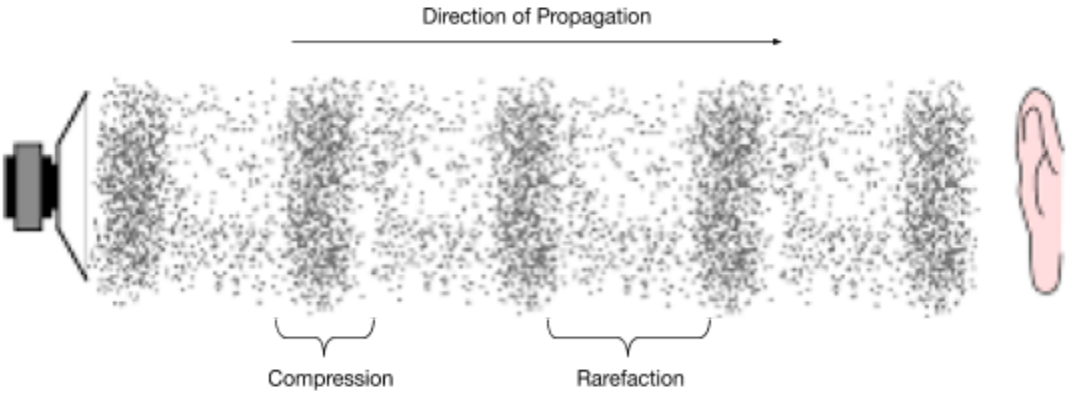

Figure 1. Sound wave

$$P_{stagnation} = P_{static} + P_{dynamic} \quad (1)$$

2.2. Hearing Mechanics of the Human Ear

The anatomy of the inner ear is depicted in Figure 2. A functioning ear combines multiple processes to translate the sound pressure of sound waves into mechanical movements and subsequently into electrical impulses. Sound waves are first “funnelled” into the ear canal by the auricle, also called the pinna. Sound waves reflect off of the auricle in different ways depending on where the sound originates, creating distinctive patterns that allow the brain to interpret and determine the direction of sound (Young, Freedman, & Ford, 2016).

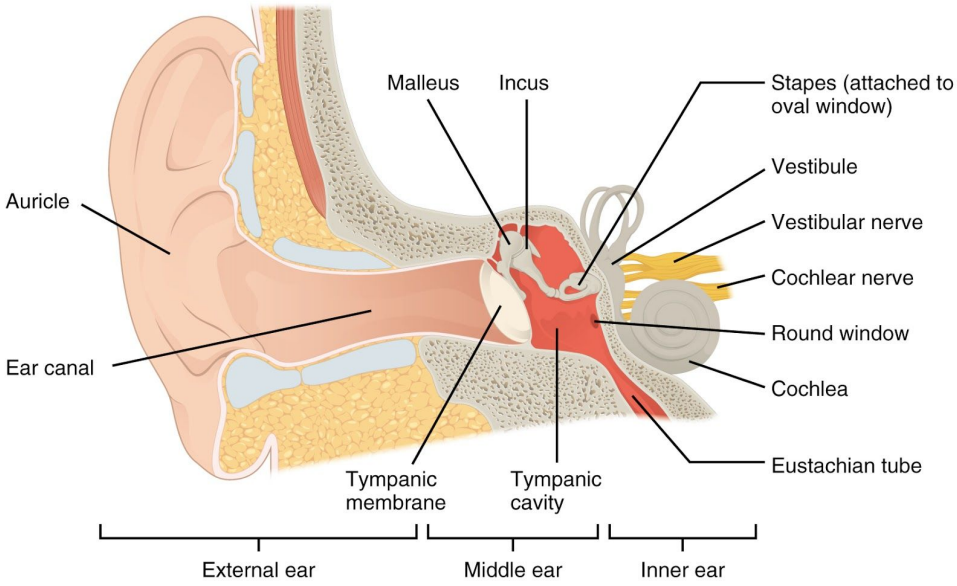

Figure 2. Anatomy of the inner ear

Once sound waves are funneled into the ear canal, they hit and vibrate the Tympanic Membrane (TM). The TM is a thin piece of skin about 10 millimeters wide, and is connected to the tensor tympani muscle, which pulls on the TM in order to keep it tight so that the whole membrane vibrates regardless of what part is hit by a sound wave (Harris, 2019). The compression region of a sound wave “pushes” the TM inward toward the eustachian tube while the rarefaction region of a sound wave “pulls” the TM outward toward the ear canal. A higher frequency sound wave pushes and pulls the TM more rapidly, while a higher pressure sound wave pushes and pulls the TM a greater distance.

The TM is connected to the ossicles, a series of bones in the middle ear. The ossicles amplify the pressure from the TM and transfer it to the cochlea, a fluid filled spiral cavity in the inner ear. When the TM is pushed inward by the compression section of a sound wave the motion of the ossicles compresses the fluid inside the cochlea, creating a pressure wave. This pressure wave travels along the surface of the basilar membrane inside of the cochlea.

The basilar membrane is a rigid surface that extends the full length of the cochlea and is composed of 20,000 to 30,000 reed-like fibers. These fibers are short and stiff near the base of the basilar membrane and become long and flexible near the end of the membrane. The length and stiffness of the fibers specify the resonant frequency of the fiber. As shown in Figure 3, the resonant frequency is highest at the base of the membrane and lowest at the end of the membrane. A pressure wave traveling along the surface of the basilar membrane only moves the fibers that correspond with the frequency of the pressure wave. These fibers then move the small hairs of the organ of the corti near the fiber, which send electrical impulses through the cochlear nerve to the cerebral cortex where the brain interprets the specific impulses into sound (Harris, 2019).

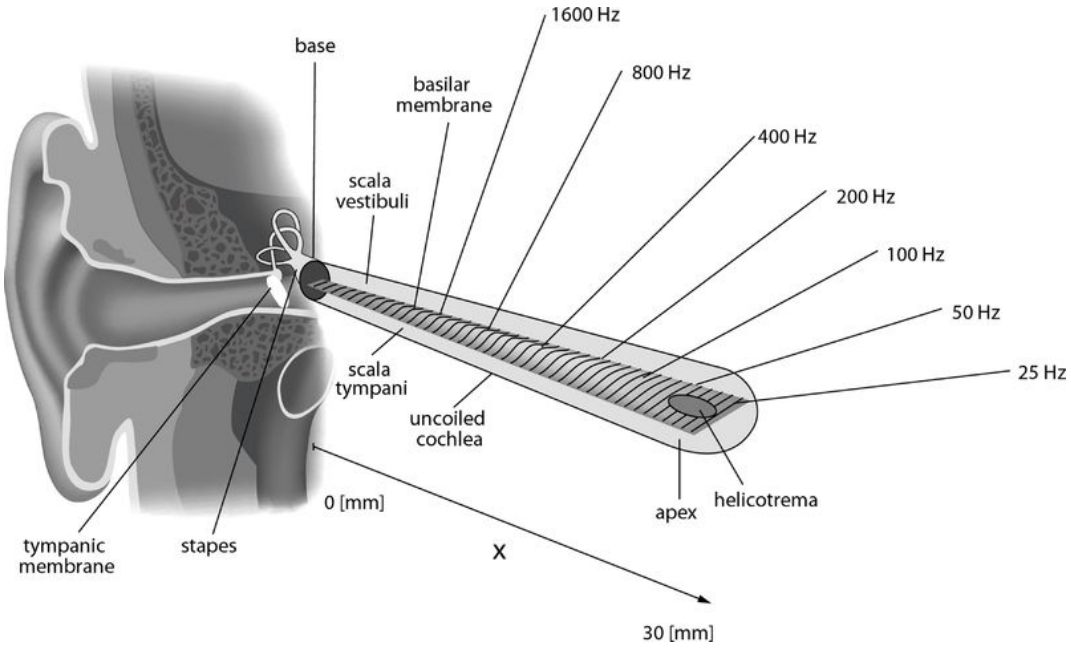

Figure 3. Uncoiled cochlea and basilar membrane

2.3. Decibels and Sound Pressure Level

The human ear is able to interpret a large range of sound pressures, from leaves rustling meters away to a military jet taking off 30 meters away. Since the range of human hearing is so large, a logarithmic scale called the decibel scale was created to more effectively compare the pressure of sounds. The Sound Pressure Level (SPL) as measured in decibels (dB SPL) is given by Equation 2, where P is the measured sound pressure and P_0 is the reference sound pressure. The reference sound pressure is the quietest sound audible by the human ear and is equal to 20 μPa (Young, Freedman, & Ford, 2016).

$$Lp = 20log(P/P_0) \qquad (2)$$

For reference, a normal conversation measured one meter away has a sound pressure of about 0.02 Pa or 60 dB SPL, street traffic measured one meter away has a sound pressure of about 0.2 Pa or 80 dB SPL, and a fired rifle measured one meter away has a sound pressure of about 200 Pa or 140 dB SPL (Young, Freedman, & Ford, 2016). The sound pressure of the three examples was measured one meter away from the source of the sound, moving further away from the source of the sound decreases the Sound Pressure Level proportional to the distance. Equation 3 shows the relationship between Sound Pressure Level and distance from the source of the sound. In Equation 3, L_{p1} is the SPL measured distance r_1 away from the sound source, and L_{p1} is the dB SPL measured distance r_2 away from the sound source (Sengpiel).

$$L_{p2} = L_{p1} - 20log_{10}(r_1/r_2) \qquad (3)$$

Exposure to loud sounds for a short period of time or moderately loud sounds for a longer period of time can cause damage to the fibers in the basilar membrane. These hair cells are unable to grow back, meaning that the hearing loss cannot be improved once damaged, emphasizing the importance of hearing protection and preventative actions (Noise-Induced Hearing Loss, 2017). The Occupational Safety and Health Administration (OSHA) created a series of noise standards for workplace environments to limit workers' exposure to loud noises. They state that sounds under 90 dB SPL are safe regardless of their duration. 90 dB SPL is the permissible exposure limit, meaning that workers can work in an environment with sounds measuring 90 dB SPL for 8 hours. After 90 dB SPL, OSHA states that every 5 dB SPL increase in sound pressure halves the amount of time a worker may be exposed to the sound. For example, workers can only be in an environment with sounds measuring 95 dB SPL for 4 hours. 140 dB SPL is the threshold for pain, and at this sound pressure, workers without hearing protection will experience immediate pain. 197 dB SPL is the average rupture pressure for the Tympanic Membrane, and at this sound pressure, workers without hearing protection will have immediate rupture of the Tympanic Membrane ("Occupational Noise Exposure").

2.4. Experimental Tympanic Membrane Research

In order to study the rupture of the Tympanic Membrane there must be a reliable and accurate method to acoustically load Tympanic Membrane specimens. The method used to load the Tympanic Membrane must also be capable of reaching a sound pressure of more than 150 dB SPL. Scientists often use shock waves to meet these requirements.

2.4.1. Shock Waves

A shock wave is a wave that propagates faster than the speed of sound in a given medium, creating drastic changes in pressure, temperature, and density. The speed of a shock wave is characterized by the Mach number, the ratio of the speed of a wave and the local speed of sound. The Mach number is given by Equation 4 where v is the speed of the wave and a is the local speed of sound (Hall, 2018).

$$M = v/a \qquad (4)$$

When the Mach number of a wave is greater than one, there is an instantaneous change across the wave in pressure, temperature, and density of the medium as shown in Figure 4. The total enthalpy and the total temperature of a shock wave are constant, however, since the flow is non-isentropic, the upstream pressure p_1 and velocity V_1 are less than the downstream pressure p_2 and velocity V_2 (Hall, 2018).

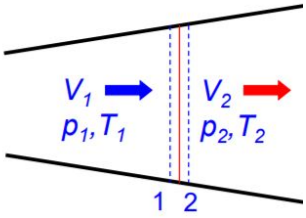

Figure 4: Normal shock wave (Hall, 2018)

The shock wave shown in Figure 4 is a normal shock wave. A normal shock wave occurs when the wave is perpendicular to the flow direction. In a normal shock wave, the upstream and downstream flows are treated as isentropic conditions. The entropy production is accounted by the drop in downstream pressure. All parameters are determined experimentally and tabulated for a normal shock wave through air, given the heat capacity ratio and Mach number. As shown in Equation 5 and Table 1, the parameters downstream are ratios of the upstream parameters (Jagadeesh, 2008).

$$\frac{p_{0_1}}{p_1} = \left(1 + \frac{\gamma - 1}{2} M_1^2\right)^{\frac{\gamma}{\gamma - 1}} \quad \frac{p_{0_2}}{p_2} = \left(1 + \frac{\gamma - 1}{2} M_2^2\right)^{\frac{\gamma}{\gamma - 1}} \tag{5}$$

Table 1. Shock Equation Parameters

P_1	Upstream Static Pressure
p_{01}	Upstream Stagnation Pressure
P_2	Downstream Static Pressure
p_{02}	Downstream Stagnation Pressure
γ	Specific Heat Capacity Ratio
M_1	Initial Mach Number

Figure 5 shows the ideal pressure vs time graph of a shock wave, called a Friedlander waveform, at a point distanced away from the source of the shock wave (Nakagawa, et al., 2011). Initially, the pressure is at the ambient air pressure. Following this, there is an instantaneous increase in pressure to peak pressure when the shock wave reaches the point. Next, the pressure decreases exponentially until the pressure reaches ambient pressure. This is the positive duration of the shock wave. Finally, the pressure continues along this decrease, and becomes less than ambient air pressure. This portion of the graph is known as the negative duration and lasts until it returns back to ambient pressure (Jagadeesh, 2008).

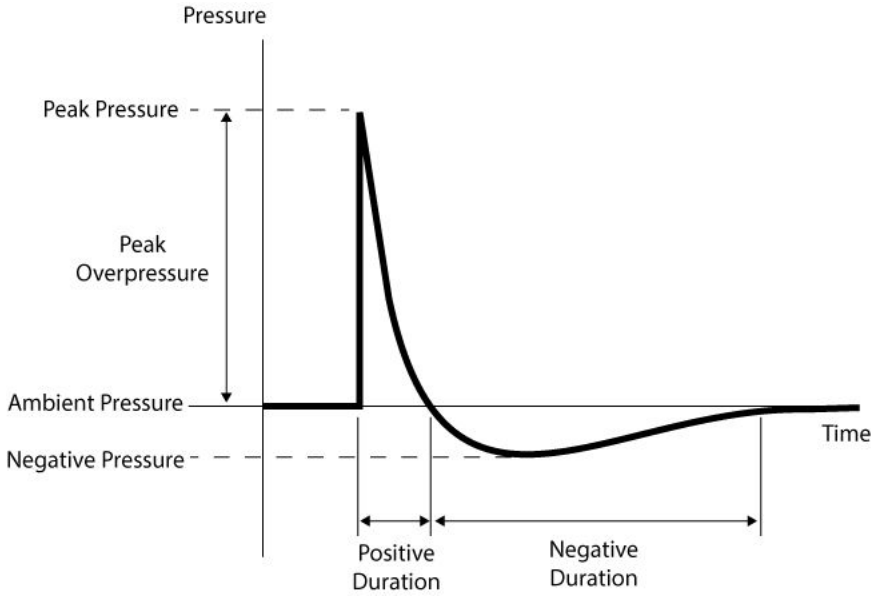

Figure 5. Friedlander waveform

The Friedlander waveform can be described by Equation 6, where P_{so} is the peak overpressure, t_0 is the positive phase duration, b is the decay coefficient, and t is the elapsed time. The decay coefficient can be determined using a non-linear fit of an experimental pressure vs time curve for the positive duration.

$$P_s(t) = P_{so}(1 - (1/t_0))e^{-b(t/t_0)} \qquad (6)$$

2.4.2. Shock Tubes

There are three main experimental methods used to create shock waves; micro explosives, blast tubes, and Shock Tubes. Due to experimental constraints, we are not able to use the explosives required for micro explosives or for blast tubes. For this reason, we focused our research on Shock Tubes. A Shock Tube is a long tube with a high pressure gas in a driving section and a low pressure gas in a driven section separated by a diaphragm, as depicted in Figure 6. The diaphragm is then either removed or ruptured to release the high pressure gas from the driving section into the low pressure driven section. The high pressure gas expands into the low pressure section creating a shock wave that propagates down the length of the driven section.

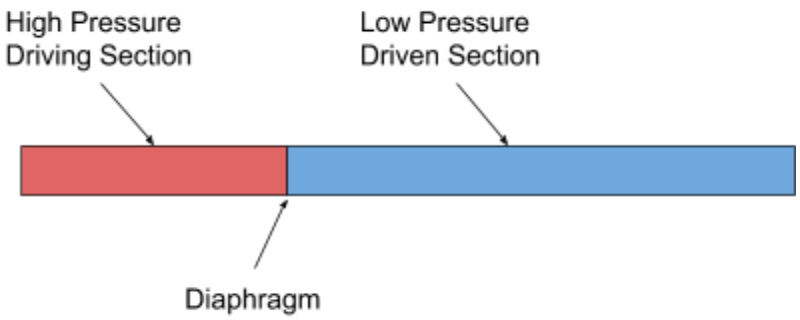

Figure 6. Shock Tube anatomy

There are several experimental methods used to release the high pressure gas into the low pressure section. The most common method uses the pressure differential between the two sections to strain a diaphragm of a known material. In this way, the diaphragm material and thickness can be chosen to rupture once the driving section reaches a specific pressure. With a circular Shock Tube cross section, the diaphragm can be modeled as a thin circular disk in order to estimate the rupture pressure of the diaphragm.

Figure 7 graphs the general behavior of the Shock Tube, in regards to wave position, velocity, pressure and temperature. One can model velocity and pressure vs position in the tube since shock waves are a non-isentropic process. Shown in figure 7, after the shock wave has occurred, pressure and velocity remain constant while inside the tube. When the incident shock occurs, expansion waves are sent backwards to the rear of the tube and are reflected back out the other end of the tube (Bokil, 2010).

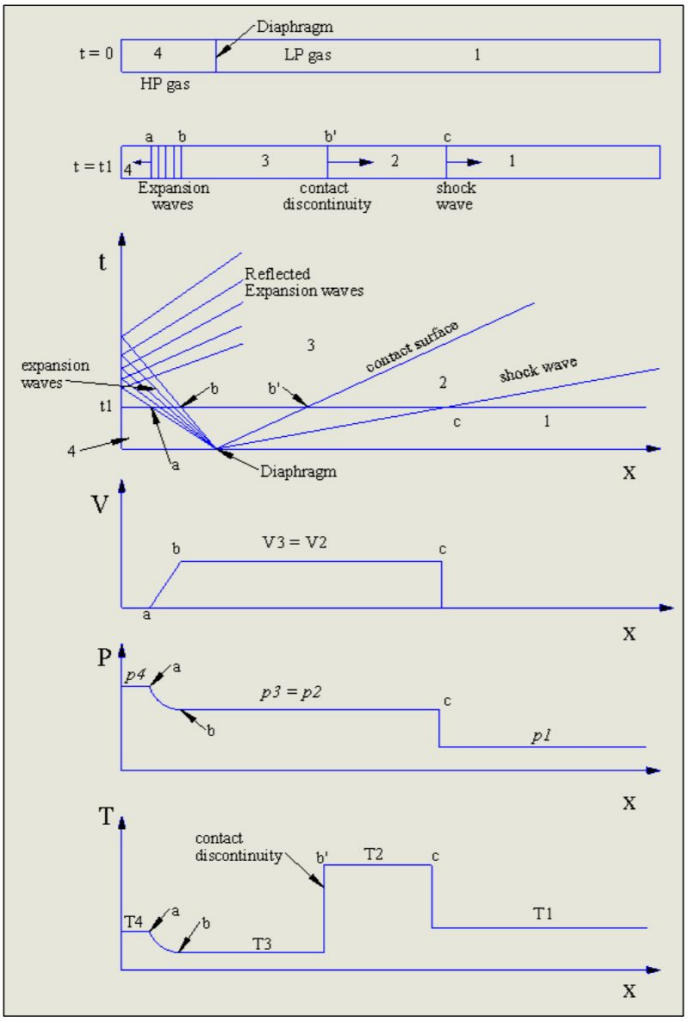

Figure 7. Position, velocity, pressure, and temperature behavior within the Shock Tube (Bokil, 2010)

2.4.2. Shock Tubes in Research

The following section outlines different Shock Tube configurations that were used in several TM rupture studies. In these case studies, a number of Shock Tubes were designed to rupture TM samples, however the characterization of the TM damage was completed post rupture. Post rupture analysis of the TM ignores the initiation and propagation of the cracks leading to rupture and neglects the frequency response of the TM. It is important to note that there is a need to to create a Shock Tube system which incorporates 3D High Speed Digital Image Correlation to visualize the movement of the TM in real time.

The University of Oklahoma has conducted two relevant studies focused on different aspects of the TM's rupture mechanics. In the first study, a Shock Tube was used to study the viscoelastic properties of human cadaver Tympanic Membranes before and after exposure to blast waves. Within this study, compressed Nitrogen was used, along with polycarbonate diaphragms ranging

from 130 to 260 μm in thickness. The device that was ultimately created was capable of generating pressures of at least 207 kPa (200 dB SPL) with a blast duration of 0.7 ms. The pressure applied to the biological samples was controlled by varying the distance of the sample from the blast. The TM sample was placed in a “head block” for support and a pressure sensor was placed at the entrance of the ear canal to monitor the blast. The TM samples in this study were subjected to subsequent blasts with increasing pressure of 15 kPa until rupture. The average rupture pressure of four human cadaver TM samples was 97.3 kPa (194 dB SPL). Post rupture, the TMs were placed in a Split Hopkinson Tensor Bar (SHTB) to determine the modulus of elasticity and maximum strain of the TM (Luo, Jiang, Nakmali, Gan, & Lu, 2015).

In the second study conducted by the University of Oklahoma, a Shock Tube was used to study the effect of blast wave direction on TM damage. In this study, a Nitrogen driven Shock Tube was used to rupture human cadaver TM samples along three directions: vertical, horizontal, and front on. The TM samples were placed in a “head block” for support with three pressure sensors to record overpressures. The first pressure sensor was placed at the entrance of the ear canal (P0), the second was placed directly in front of the TM (P1), and the third was placed directly behind the TM in the middle ear (P2). Figure 8 shows the pressure vs time graphs for the three loading directions. From the graphs it is observed that the peak pressure value for P1 is greater than the peak pressure observed from P0. The pinna and auditory canal separated P0 from P1, which brought researchers to the conclusion that the sound pressure levels were amplified by these organs. This study also found that the direction of blast had an influence on the threshold rupture pressure of the TM. The mean threshold was 139 kPa (197 dB SPL) in the vertical direction, 138 kPa (197 dB SPL) in the horizontal direction, and 115 kPa (195 dB SPL) in the front direction (Gan, Leckness, Nakmali, & Ji, 2018). With these varying rupture levels, it can be determined that the ear’s orientation from the blast also plays a large role in the rupture mechanics observed.

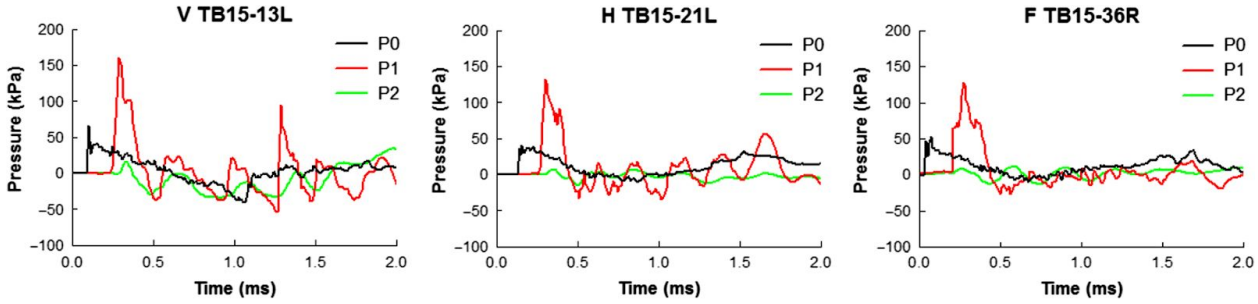

Figure 8. Shock wave pressure vs time graphs (Gan, Leckness, Nakmali, & Ji, 2018)

Members of the University of Oklahoma have also collaborated with researchers at the University of Texas to develop a Shock Tube to rupture the TM of mice. The Shock Tube was made out of a 2.72 meter long PVC tube with an outer diameter of 11.5 cm. Using compressed air released by a toggle valve, this device was able to deliver blasts of 186 kPa (199 dB SPL) to the specimen. To characterize the blast, they measured both the static and the stagnation pressure just below the specimen, 11 cm from the end of the tube. They also used a high-speed video recording system to image the blast at 1,000 fps. In Figure 9, graphs A and B show the pressure vs time graphs from

pressure sensor and graphs C and D show the relationship between the driving pressure and Blast Peak Pressure and Blast Duration. In graph A and B, the pressure vs time data matches the theoretical Friedlander waveform. Graph C shows that there is a linear relationship between the tank pressure (driving pressure) and the blast peak pressure. And graph D shows that the is a linear relationship between blast peak pressure and blast duration. After administering the blast, researchers conducted histological studies to examine auditory thresholds and cellular damage of the cochlea and TM (Cho, et al., 2013) .

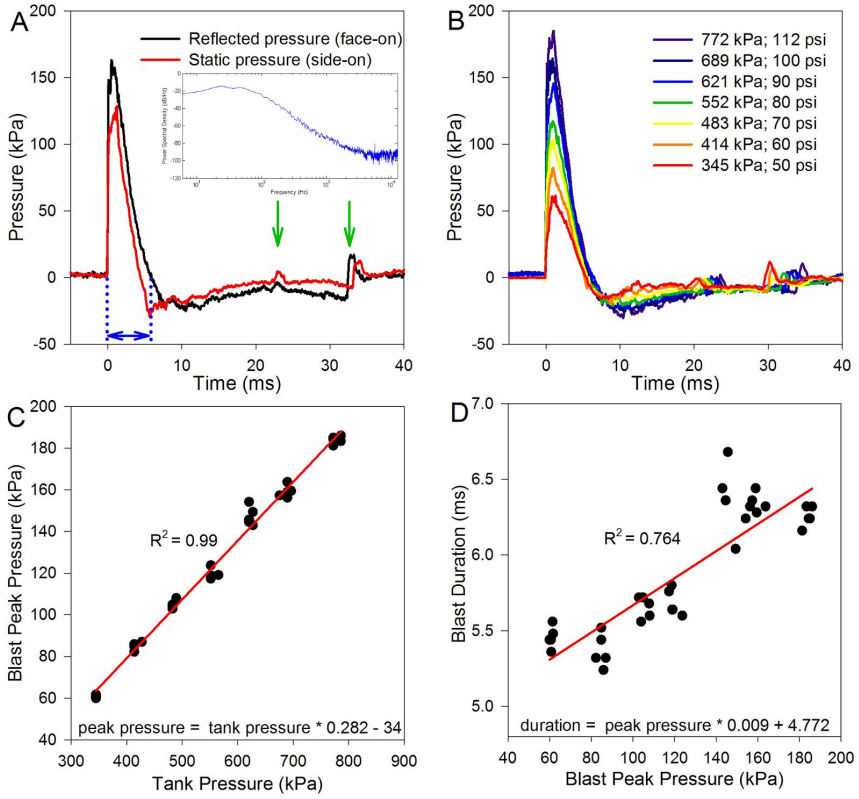

Figure 9. Shock wave characteristics (Cho, et al., 2013)

3. Methodology

Based on the background research, our team designed a Shock Tube to create transient acoustic forces to rupture the Tympanic Membrane. Before designing the Shock Tube, we created and tested a single mirror Schlieren photography configuration to image the refractive index of compressed gases for the purpose of visualizing the produced shock fronts. Next, we conducted a compressible flow experiment to develop a procedure to quantitatively and qualitatively measure high speed compressed flow, detailed in Appendix A. We then designed and analyzed a Shock Tube using numerical methods and simulations. Finally, we constructed the Shock Tube and conducted experiments using pressure sensors to monitor the thermodynamic properties within the tube. High speed cameras were used with our Schlieren configuration to visualize the blast. The following sections describe the methods used to develop the Shock Tube.

3.1. Use of Schlieren Techniques to Visualize Acoustic Pressure

We used Schlieren photography to quantitatively and qualitatively analyze sound waves and acoustic pressures. Schlieren photography is a method of photography used to visualize the movement of fluids with different refractive indices. Schlieren photography can be used to visualize a variety of different environments, from the shock waves produced by jets as they break the speed of sound to the thermal plume given off by a candle.

A Single Mirror Schlieren Setup, shown in Figure 10, has four main components; a point light source (1), a circular mirror (2), a knife edge (or razor blade) (3), and a camera (4). The point light source is directed at a circular mirror and is placed away from the mirror at a distance of twice the mirror's focal length. The circular mirror reflects and focuses the light onto a camera's light sensor. To increase the contrast of the Schlieren effect, half of the focused light is blocked from hitting the camera's light sensor by a razor blade.

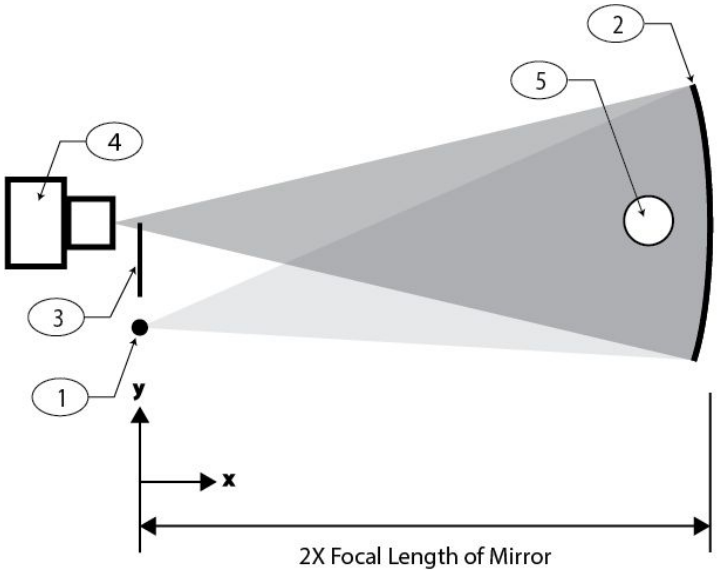

Item	Description	Qty	Unit
1	Point Light Source	1	PC
2	Circular Mirror	1	PC
3	Razor Blade	1	PC
4	Camera	1	PC
5	Test Area	-	-

Figure 10. Single mirror Schlieren setup

Under normal circumstances, the light from a point light source would propagate uniformly through a homogeneous medium (Settles, 2013). However, a change in the refractive index of the fluid in the test area, can change the light's direction. If this light is deflected past the edge of the razor blade, the additional light that enters the camera will be seen as streaks of light ("Schlieren Optics", 2019). The brightness of the streaks is proportional to the change in the density and subsequently the change of the refractive index of the fluid in the test area. Equation 7 describes the relationship between the refractive index and the density for most gases. In this equation, n is the index of refraction, ρ is the density, and k is the Gladstone-Dale coefficient. The angular deflection of the light due to the change in density is given by Equation 8. In Equation 8, δ is the angular deflection, L is the length of the density change along the x-axis, and $d\rho/dx$ is the density gradient along the y-axis ("Schlieren Optics", 2019).

$$n - 1 = k\rho \quad (7)$$

$$\delta = kL\, d\rho/dx \quad (8)$$

Before using the Single Mirror Schlieren Setup to analyze sound waves, we tested the experimental methodology using a heat gun and a DSLR camera. First, we determined the focal length of the 10 inch (25.4 cm) diameter mirror using the Equation 9, where f is the focal length, d_o is the object distance, and d_i is the image distance. The point source light was first set at an arbitrary length from the mirror and directed at the mirror's center. The focal point of the reflected light was located by finding the position where it was the smallest using an opaque surface. The light image grew when the surface was moved forward to backwards from the focal point. The distances of the image to the mirror and the object to the mirror were measured and plugged into Equation 9, resulting in the focal length measuring 60 inches (152 cm). For the purpose of the Schlieren setup,

the light source and the razor blade were placed in line with each other at twice the focal length from the mirror, 120 inches (304 cm).

$$1/f = 1/d_0 + 1/d_i \quad (9)$$

The Schlieren setup is depicted in Figure 11. The point light source consisted of a small flashlight covered in aluminum foil with a pinhole. The light source was held into place with stands and directed at the center of the mirror. The reflected light was aligned such that it was in line with light source, partially blocked by the razor blade, entering the center of the DSLR camera lense. We used a Nikon D3400, with the aperture set to F9, exposure compensation set to -3, manual focus and the Nikon AF-P Nikkor 18-55 mm lense. The images resulting from this configuration can be seen in Figures 12 and 13.

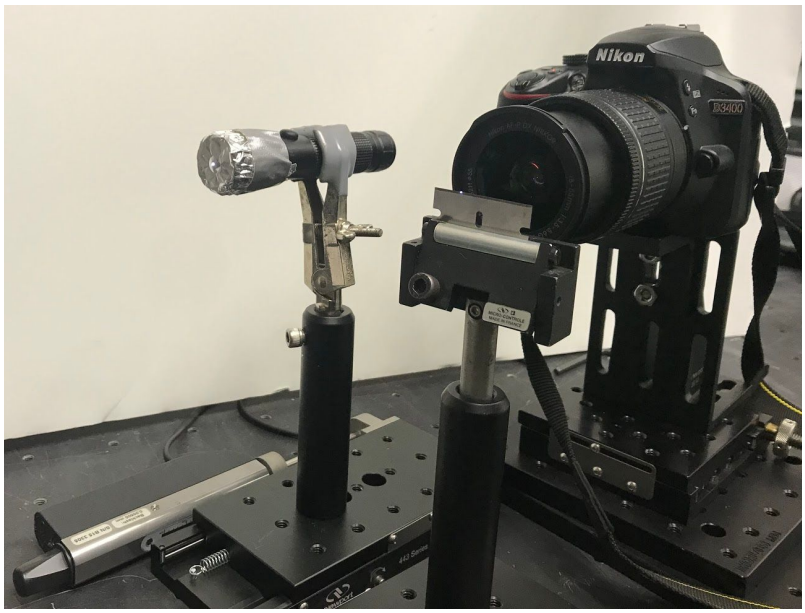

Figure 11. Schlieren setup consisting of point light source, DSLR camera, and razor blade held with fixtures to table and projected on 10 inch mirror 120 inches away

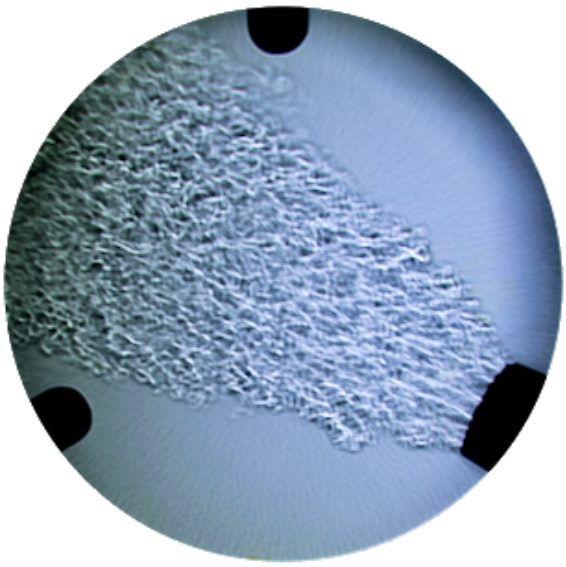

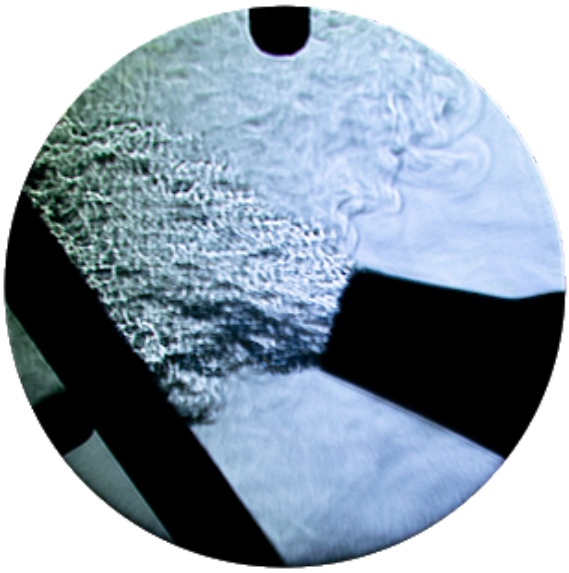

[Left to Right] Figure 12. Schlieren image of a hair dryer, Figure 13. Schlieren image of a hair dryer against a board

After testing the Schlieren imaging methodology, we substituted the DSLR camera with a Photron SA5 high speed camera. The SA5 high speed camera has a max frame rate of 1,000,000 frames per second, which allowed us to record the propagation of sound waves. In the next sections, we used Schlieren photography to qualitatively analyze the shape of sound waves and quantitatively measure the speed of sound waves using Photron motion analysis software.

3.2. Characterization of Initial WPI System

Before we began the development of a Shock Tube, we first characterized the original apparatus that Worcester Polytechnic Institute's Center for Holographic Studies and Laser micro-mechaTronics (CHSLT) used to rupture Tympanic Membrane samples. The original system was used to complete 3D High-Speed Digital Image Correlation studies of Tympanic Membrane samples under two loading conditions using pressurized air.

The main pressure delivery system of the apparatus is shown in Figure 14. High pressure air from a wall source (85-110 psi) is fed through flexible tubing (3), to a pressure regulator (2), and into a SPEEDAIRE pressure tank with a 10 gallon capacity (1). The pressurized air from the tank is fed through a 1/2 inch flexible tubing (5) to a 1/2 inch steel pipe (6). The pressure in the steel pipe is released with a Norgren 13J Solenoid controlled by a function generator (7).

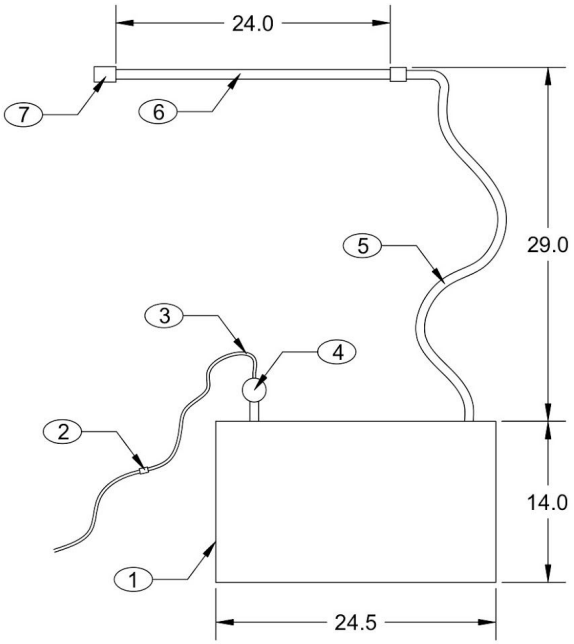

ITEM	DESCRIPTION	QTY	UNIT
1	SPEEDAIR Pressure Tank	1	PC
2	Air Tak Pressure Regulator	1	PC
3	1/4 in OD Flexible Tubing	12	FT
4	ARO Pressure Gauge	1	PC
5	1/2 ID Flexible Pipe	3	FT
6	1/2 ID Steel Pipe	2	FT
7	Norgren 13J Solenoid	1	PC

Figure 14. Main pressure delivery system

Attached to the solenoid were two interchangeable pressure loading devices. The first device used an air horn to load the sample with a high intensity sound wave, Figure 15. A high frequency PCB 102B16 pressure sensor (Ai0) was used to measure the “Inline Pressure” and a ¼ in PCB condenser microphone (Ai1) placed five millimeters away from the Tympanic Membrane was used to measure the “Acoustic Pressure”.

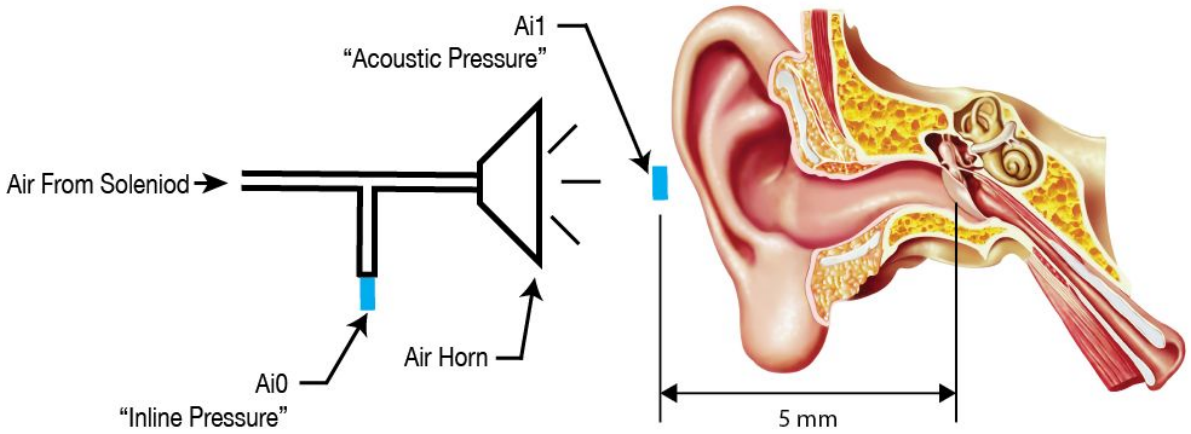

Figure 15. Sound wave mechanism

We used high speed Schlieren Photography to investigate the formation and propagation of the acoustic waves produced by the sound wave mechanism. We used a similar single mirror

Schlieren Photography setup shown in Figure 16, as discussed in Section 3.1, to image the acoustic waves created by the horn. A National Instruments Data Acquisition device was used to synchronize the opening of the solenoid with the start of data acquisition from a PCB Pressure Sensor and the start of the recording of a Photron SA5 High Speed Camera.

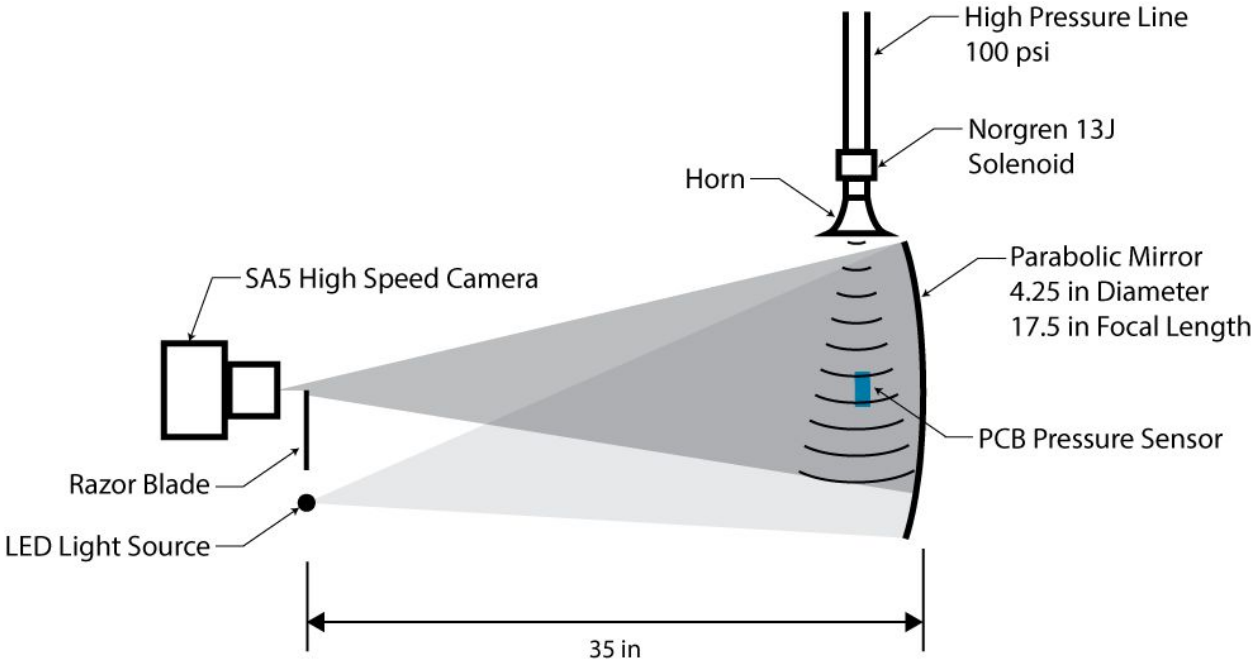

Figure 16. Sound wave mechanism Schlieren photography setup

A still image from the recorded high speed Schlieren video is shown in Figure 17. In the image, there are two distinct lines, the first line is the acoustic wave created by the horn, the second line is a “ghost” wave. This “ghost” wave does not exist, rather it is a result of the small focal length of the parabolic mirror used in the Schlieren setup. We used Photron’s analysis software to trace the path of the wave as it propagated across the mirror to determine the speed of the wave. This analysis determined the average speed of the wave to be 353 m/s, 3% within the theoretical speed of sound at room temperature.

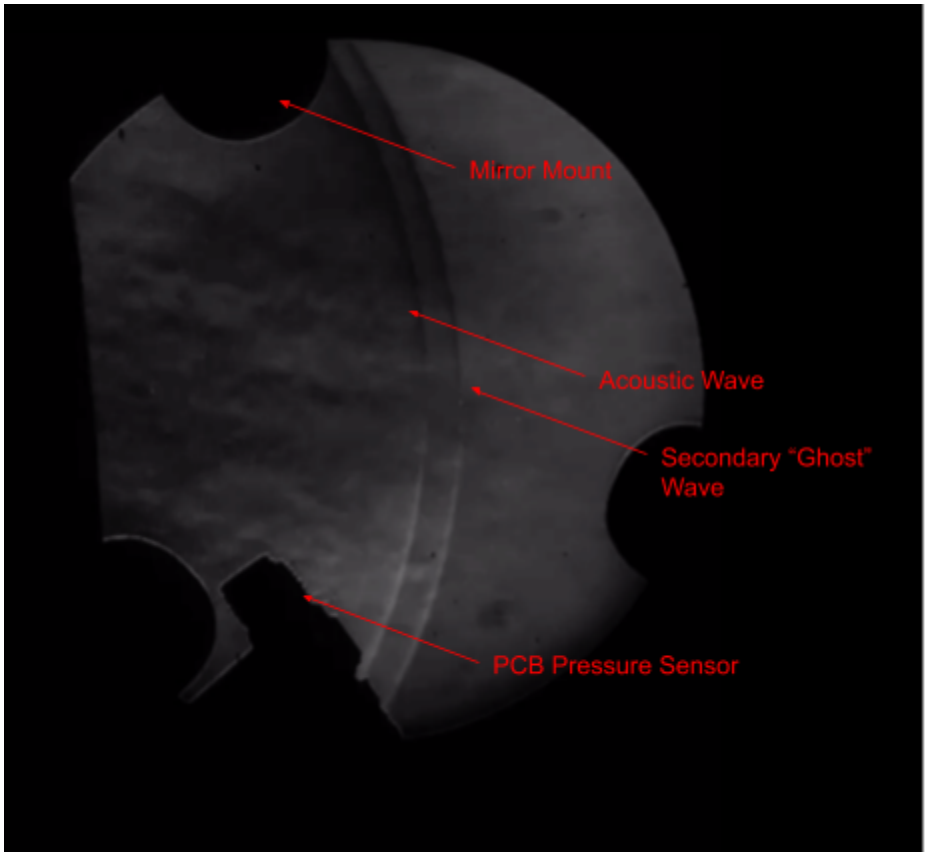

Figure 17. Schlieren photography of the acoustic wave produced by a horn

The PCB Pressure Sensor was aligned in relation to the acoustic waves to measure the stagnation pressure of the waves with a sampling rate of 1.5 MHz. This sampling rate was chosen to achieve sufficient resolution on the Pressure vs Time graph, Figure 18, and to satisfy the Nyquist Criterion. The Pressure vs Time graph contains a 3 ms section of data with three distinct peaks corresponding to three distinct sound waves created by the horn. The peak pressure of the sound waves was 440 Pa (147 dB SPL). The sound pressure produced by this setup was unable to rupture Tympanic Membrane samples, instead it was used to excite the membrane to test the experimental setup and data acquisition.

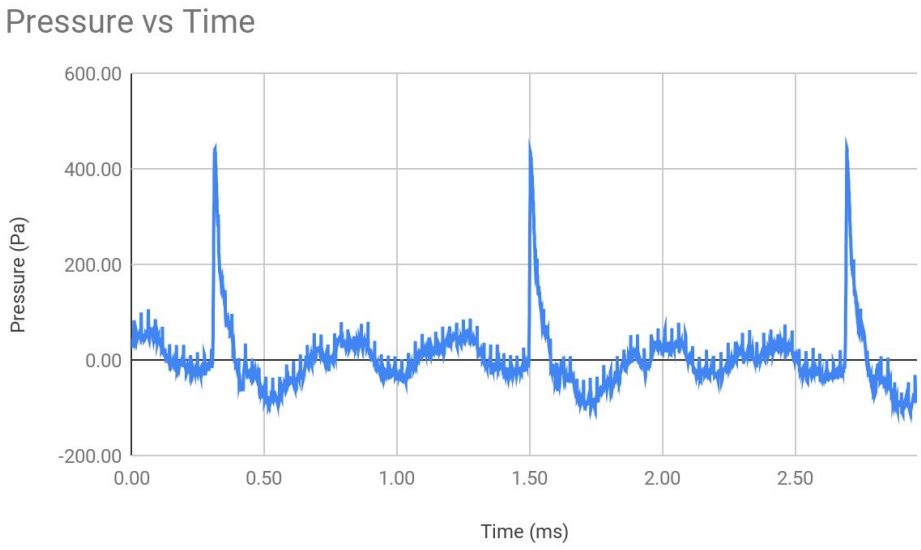

Figure 18. PCB pressure vs time graph for the sound pressure mechanism

The second device used a high pressure line placed inside a hole in the facial recess to create a pressure difference, Figure 19. A high frequency PCB pressure sensor (Ai0) was used to measure the “Inline Pressure” and a ¼ in PCB condenser microphone (Ai1) placed five millimeters away from the Tympanic Membrane was used to measure the “Acoustic Pressure”.

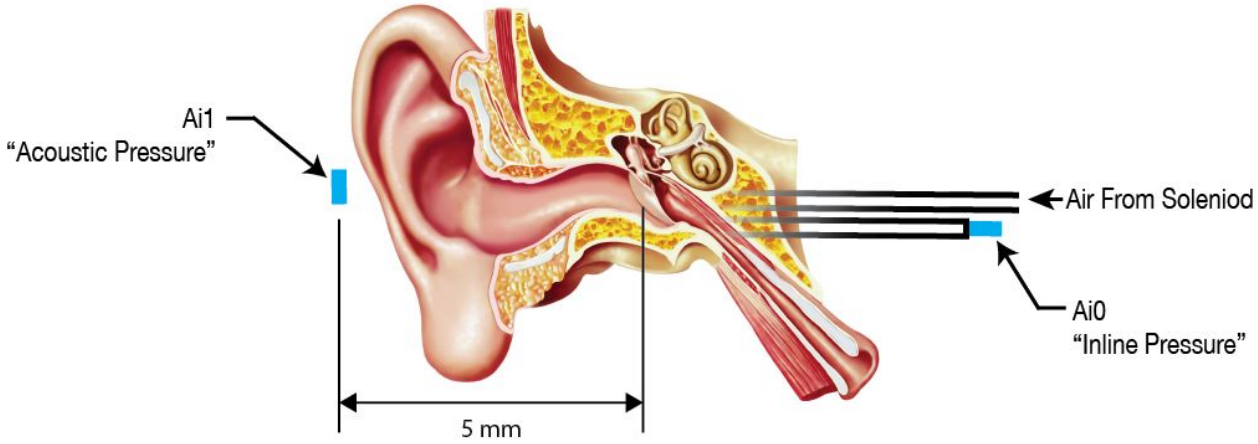

Figure 19. Pressure Difference Mechanism

The Pressure Difference mechanism was able to rupture human Tympanic Membrane samples. One successful rupture experiment was conducted with a Tank Pressure of 20 psi (127.9 kPa). The resulting inline pressure measurements are shown in Figure 20 for a one second period of time. At 40 ms, the solenoid was opened, releasing high pressure air into the facial recess. The solenoid was open for 245 ms, and closed at 285 ms. The inline pressure at initial release was 7.5

psi (51.7 kPa) and decreased to 6.4 psi (44.1 kPa) right before the solenoid closed. After closing, the inline pressure reached a peak negative pressure of -0.95 psi (6.5 kPa). The ¼ in PCB condenser microphone recorded atmospheric pressure during the full sample period.

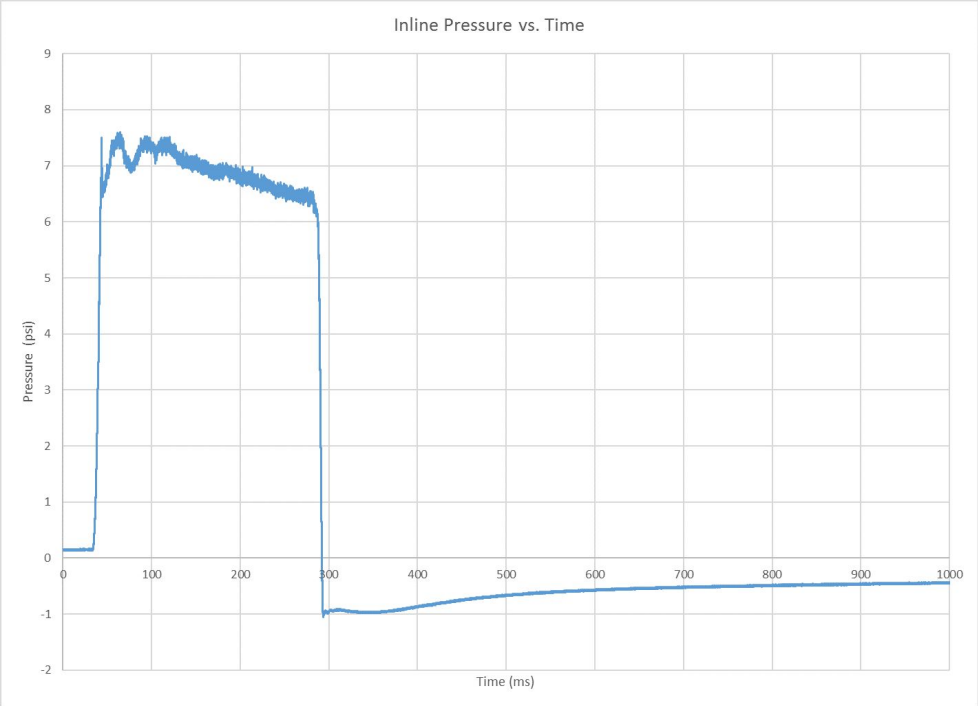

Figure 20. Inline pressure vs time for pressure difference mechanism

Although the pressure difference mechanism was able to rupture Tympanic Membrane samples, the loading scenario was not representative of the type of events in which human Tympanic Membranes rupture. As previously discussed, a large majority of Tympanic Membrane damage is due to loud acoustic noises in the workplace and in combat. In order to more accurately model the loading scenario in which a Tympanic Membrane would rupture, we created a Shock Tube.

3.3. Design

Based on previous research and our analysis of the system used by CHSLT to rupture Tympanic Membranes, we began the design of a Shock Tube. We chose to design an air driven Shock Tube that would use the pressure difference between the driving and driven sections to rupture the diaphragm. This diaphragm rupture method allows for control over the driving pressure while still keeping the design simple and cost of materials low. The sound pressure produced by a Shock Tube is directly proportional to the rupture pressure of the diaphragm, this means that by controlling the diaphragm rupture pressure, we are able to control the sound pressure at exit (Cho, et al., 2013).

In order to design the Shock Tube, we first created a set of functional specifications to guide the development of the Shock Tube. Next, we completed numerical and finite element analysis

simulations to understand the effect of design parameters. Finally, we constructed and analyzed a physical prototype.

3.3.1. Functional Specifications and Constraints

Through research and preliminary experiments, we created a set of initial functional specifications and constraints to guide the development of a loading apparatus.

1. The apparatus will produce varying acoustic pressures, reaching pressures capable of rupturing human Tympanic Membrane samples (>150 dB SPL)

2. The acoustic force produced by the apparatus must not harm the high speed imaging cameras

3. The apparatus must not obstruct the field of view of the cameras

4. The Shock Tube configuration must be designed so that the tube and components can be mounted safely onto an 4 foot by 6 foot optics table that has screw holes 1 inch on center

Our team understood the potential danger that existed in realizing this Shock Tube. Our ultimate sound pressure level goal could possibly inflict damage on our own ears and the expensive equipment in the lab. With this knowledge, we developed a Safety Protocol to mitigate any possible hazardous incidents, Appendix B.

3.3.2. Numerical Methods

We used numerical methods to predict and understand the influence of design characteristic on the performance of the Shock Tube. Using the Thin Disk Theory, equation 10, we were able estimated the rupture pressure in the driving section based on the material properties of a given diaphragm (Beardmore, 2013).

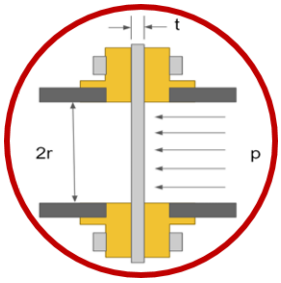

Figure 21. Diaphragm and flange mount schematic

$$p = \frac{\sigma_m * (4t^2)}{r^2} \quad (10)$$

We used the Rankine-Hugoniot relations to describe the conditions across both sides of the non-isentropic shock wave and to estimate the Mach number of the incident shock. Using the adiabatic gas law and assuming particle velocities and pressures are continuous since there is no flow of air across the diaphragm we can model the pressure differential as seen in Equation 11 (Kurian). In Equation 11, P_4 is the pressure of the driving section, P_1 is ambient pressure on the low pressure side of the diaphragm, γ_1 and γ_4 are the specific heat capacity ratios of air in the two regions and can be modeled as equal, c_1 and c_4 are the local speed of sounds of air in the two regions, and M_S is the estimated Mach number.

$$\frac{P_4}{P_1} = \frac{2\gamma M_1^2 - (\gamma - 1)}{(\gamma + 1)} \left\{ 1 - \frac{\gamma - 1}{\gamma + 1} \frac{c_1}{c_4} \left(M_1 - \frac{1}{M_1} \right) \right\}^{-\left(\frac{2\gamma}{\gamma - 1}\right)} \tag{11}$$

3.3.3. Design

The length of the driven and driving sections, the diameter of the tube, and the geometry of the diaphragm holder were the most important design components of the Shock Tube. To determine the length of the driver and driven section, the most important concept to take into consideration was the length ratio. In this ratio, the length of the driven section is divided by the length of the driver section. To have a fully functioning Shock Tube, this ratio must be greater than 1, meaning that the driven section must be larger than the driver section (Bokil, 2010). Another study found that the optimal driver/driven ratio, the inverse of what was previously discussed, existed between 0.25 and 0.75. This same study used PVC piping 2 inch in diameter (Huynh, Gregory, & Zhuang, 2013).

To fit within the design parameters and to keep the Shock Tube small enough to fit on 4 ft by 6 ft optics table, we chose the length of the driver section to be one foot, and the length of the driven section to be three feet. With this design, the driven/driver ratio equalled 3 and the inverse driver/driven ratio equalled 0.33. We used the studies suggested diameter of 2 inches, as it has been experimentally validated and can be easily fabricated using commercial products. We verified the behavior of the Shock Tube with the chosen geometry using an ANSYS Fluent Simulation before beginning construction.

We used Reynolds Heavy Duty Aluminum Foil as the diaphragm material due to its availability and use in other Shock Tubes. The aluminum foil had an average thickness of 0.033 mm. Using the Thin Disk Theory, we predicted the diaphragm would rupture at 79.5 kPa. Based on our initial Thin Disk Theory calculations, and assuming a constant specific heat capacity ratio of 1.4, we used the Rankine-Hugoniot relations to calculate an estimated Mach number of 1.14. We used the Mach number calculated from Equation 11 to estimate the stagnation pressure, P_2, behind the created shock wave in Equation 12. This number was found to be 35 kPa. From this value, we would expect a sound pressure level of approximately 185 dB SPL at the opening of the Shock Tube.

$$\frac{P_2}{P_1} = 1 + \frac{2\gamma}{\gamma + 1}\left(M_S^2 - 1\right) \quad (12)$$

3.3.4. ANSYS Fluent Simulation

We used ANSYS Fluent to simulate the behavior of the initial Shock Tube design. This simulation was used to validate the numerical methods previously described and to characterize the transient pressure, velocity, and density values at different points in the Shock Tube. The simulation results were also compared to the experimental results.

ANSYS is a finite element analysis simulation software that uses the finite element method to numerically solve boundary value and partial differential equations. ANSYS Fluent is a component software of ANSYS that is used to model flow, turbulence, heat transfer, and reactions. A general finite element simulation consists of four basic parts; a base model, a mesh, a setup, and a solution. In this simulation, we used a 2D axisymmetric model made in ANSYS Design Builder. A representation of the model is shown in Figure 22. An axisymmetric model is used to simplify a 3D revolved feature, shown in Figure 23, into its 2D cross section. The simplified model can be solved faster then the 3D feature without losing accuracy.

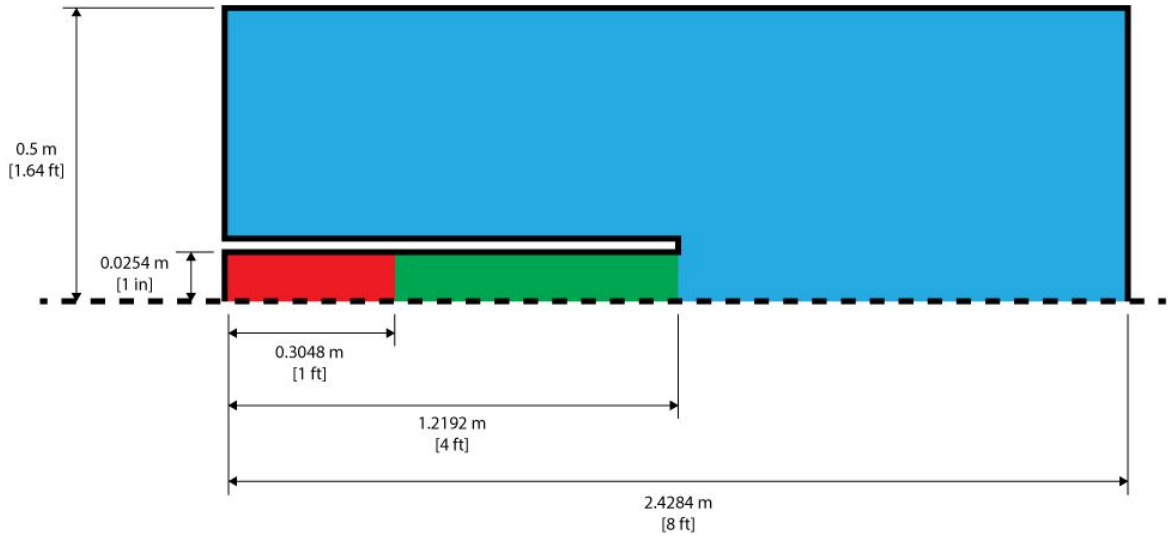

Figure 22. 2D axisymmetric model

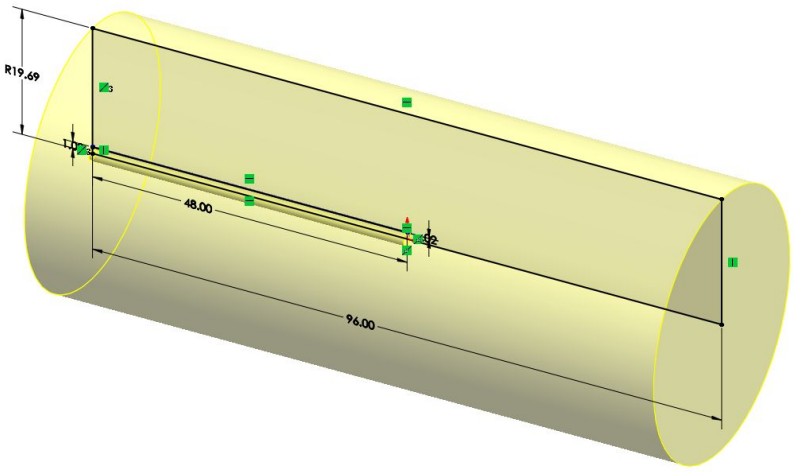

Figure 23. 2D axisymmetric revolve feature

The 2D axisymmetric model was meshed using an 10 layer inflation layer along the edge of the Shock Tube and variable sizing in the atmosphere sections. The inflation layer along the edge of the Shock Tube decreases the mesh size leading up to the edge to obtain a more accurate solution of the fluid-surface boundary layer, shown in Figure 24. The variable sizing in the atmosphere sections was used to increase the mesh density in high fluid flow areas, with an average element size of 5 mm, and to decrease the mesh density in low fluid flow areas, with a max element size of 176 mm. By changing the mesh size in certain locations, we could achieve higher discretization in important areas while also decreasing overall solve time. The mesh had a total of 443,494 nodes and 42,845 elements. The three outer walls shown in Figure 25 were set as pressure outlets in the simulation solution to represent realistic atmospheric conditions and the axis was set to fulfill axisymmetric conditions.

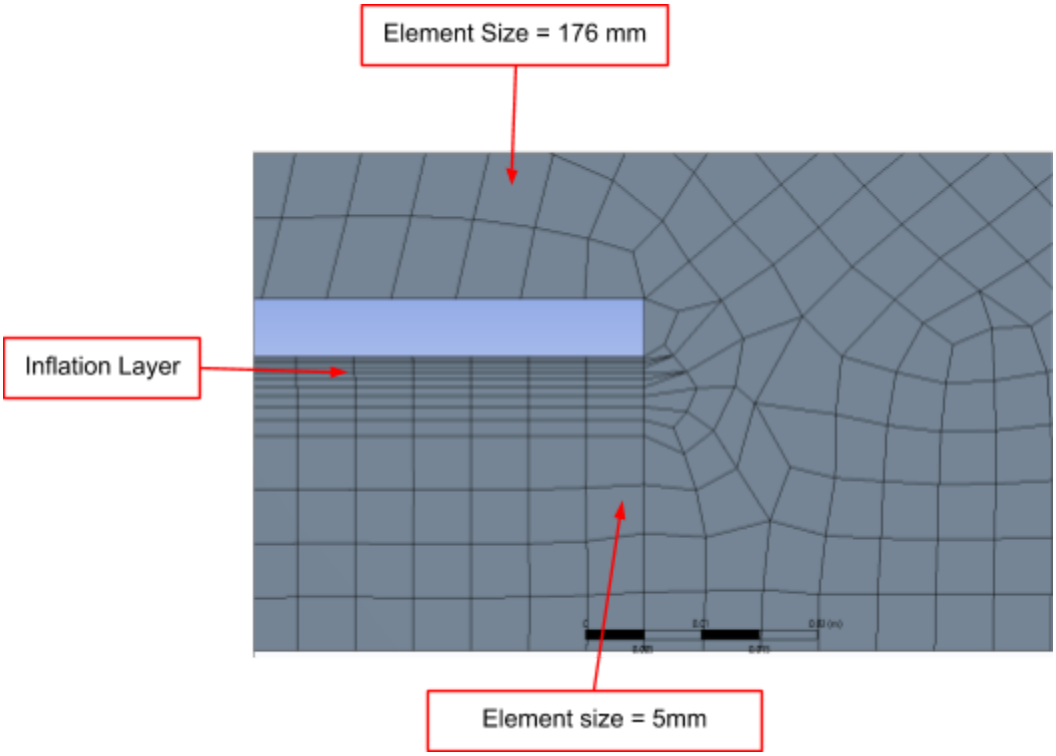

Figure 24. 2D axisymmetric mesh, end of Shock Tube

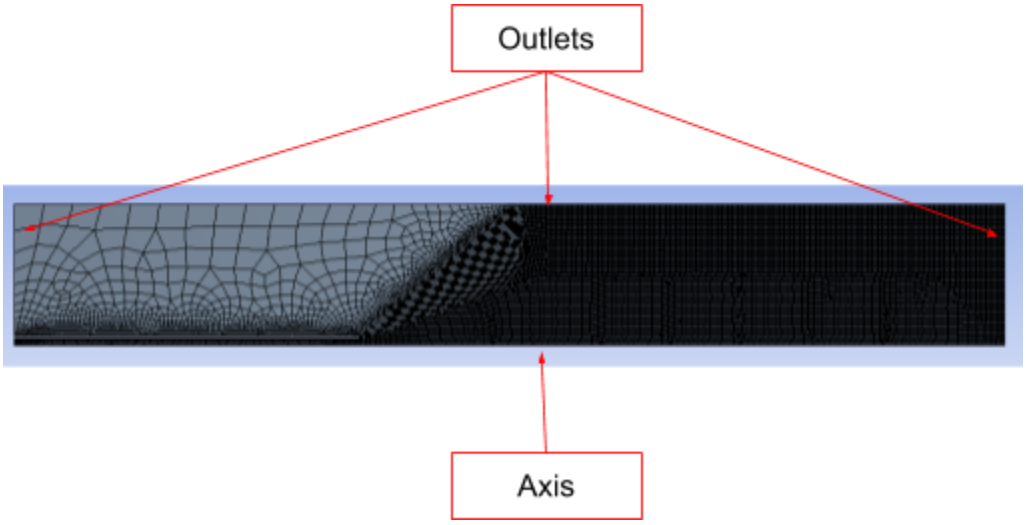

Figure 25. 2D axisymmetric mesh boundary conditions

Before applying specific models, we first solved for the Knudsen number. The Knudsen number is a dimensionless quantity that characterizes the boundary conditions in a fluid flow and determines if the Navier-Stokes equations can be applied to a simulation model. The Knudsen number is given by Equation 12 where λ is the mean free path and L is the characteristic length. For Knudsen numbers below 0.001, the continuum hypothesis is true and the Navier-Stokes equations can be

applied. Based on the geometry of our Shock Tube model, the maximum Knudsen number is 3.3e-6, meaning that the Navier-Stokes equations may be used (Rapp, 2017).

$$K_n = \lambda / L \qquad (12)$$

To solve the system, we used a transient density based model with the energy model and a shear stress transport (SST) K-Omega turbulence model. The ANSYS Fluent density-based solver solves the governing equations of continuity (13), momentum (14), and energy simultaneously (14). Each iteration contains four main steps. First, the fluid properties of the model are updated based on the current or initialized solution. Second, the continuity, momentum, and energy equations are solved simultaneously. Third, the equations for scalars, such as turbulence and radiation, are solved for. Finally, convergence is checked. Steps one through four are repeated until the convergence criteria of the governing equations are met (Density-Based Solver, 2006).

$$\frac{\partial \rho}{\partial t} + \nabla \cdot (\rho \vec{u}) = 0 \qquad (13)$$

$$\frac{\partial}{\partial t}(\rho \vec{u}) + \nabla \cdot (\rho \vec{u}\vec{u}) = \nabla \cdot (-p\mathrm{I} + \Gamma) \qquad (14)$$

$$\frac{\partial}{\partial t}(\rho E) + \nabla \cdot (\rho \vec{u} E) = \nabla \cdot \left[(-p\mathrm{I} + \Gamma) \cdot \vec{u}\right] - \nabla \cdot \vec{q} \qquad (15)$$

The SST K-Omega turbulence model is a two-equation eddy-viscosity model, and one of the most commonly used turbulence models. This model especially suited for situations with adverse pressure gradients, separating flow, and for low reynolds flows without the need for extra damping functions (Menter, 1993). In this simulation, we also assumed air to be an ideal gas with a constant specific heat to simplify the simulation. Assuming a constant specific heat means that the specific heat of the the air in the simulation will not change with temperature. This assumption is valid when the operating temperature range of the air is small. Assuming air acts as an ideal gas means that there is a direct correlation between pressure, volume, temperature, and quantity of gas as given by the Ideal Gas Law, Equation 16. In this equation, p is the absolute pressure, V is the volume, n is the number of moles of the gas, R is the universal gas constant, and T is the absolute temperature. It is safe to assume a gas will obey the ideal gas law if the compressibility factor, Equation 17, is close to unity.

$$pV = nRT \quad (16)$$

$$Z = pV/nRT \quad (17)$$

3.4. Shock Tube Realization

After numerical methods and simulations confirmed the desired performance of the Shock Tube geometry, we designed, fabricated, and assembled the Shock Tube, Figure 26. The driving section of the Shock Tube was made from one foot of schedule 80 PVC tubing. One end of the section was connected to a high pressure line otherwise closed to the atmosphere and the other end threaded to allow for the attachment of a diaphragm flange mount. The driven section was made from a second section of schedule 80 PVC tubing that was three feet in length, with one end open to the atmosphere and the other end open and threaded to allow for flange mount attachment.

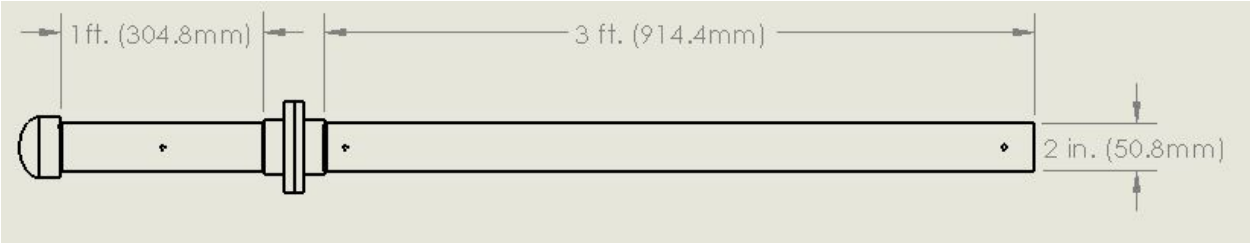

Figure 26. Shock Tube driving and driven lengths

One of the integral parts of the Shock Tube is the diaphragm mount that can be seen in Appendix C. We designed a custom mount for our Shock Tube out of 1045 steel. The mount was designed with a circular bolt pattern consisting of six holes to ensure equal pressure distribution across the mounted diaphragm. We chose steel as the diaphragm holder material for its high yield stress and hardness. Six 5/16-18 High-Strength Serrated-Flange Hex Head Screws 1.5 in long and six 5/16-18 High-Strength Steel Flange Nuts were used to hold both sides of the flange together. A 3 in X-Profile Oil-Resistant Buna-N O-Ring was used to seal the diaphragm. Reynold Wrap Heavy Duty aluminum foil was used as the diaphragm material in the Shock Tube. The foil had an average thickness of 0.33 mm. Prior to each experiment, the diaphragm was loaded following the procedure in Appendix D.

After the construction of the Shock Tube shown in Figure 27, we developed a mounting system to prevent recoil effects. To secure and counteract Shock Tube recoil, the Shock Tube was clamped with four Heavy Duty Beta Clamps, made out of steel with an aluminum cushion. We drilled holes through the Aluminum cushion of each clamp to mount the clamps to 3 in Aluminum T-slotted framing using bolts and drop in fasteners. The T-slotted framing was secured to the optics table using corner gussets. This recoil mounting system also lifted the Shock Tube to the desired height for Schlieren imaging and sample rupturing.

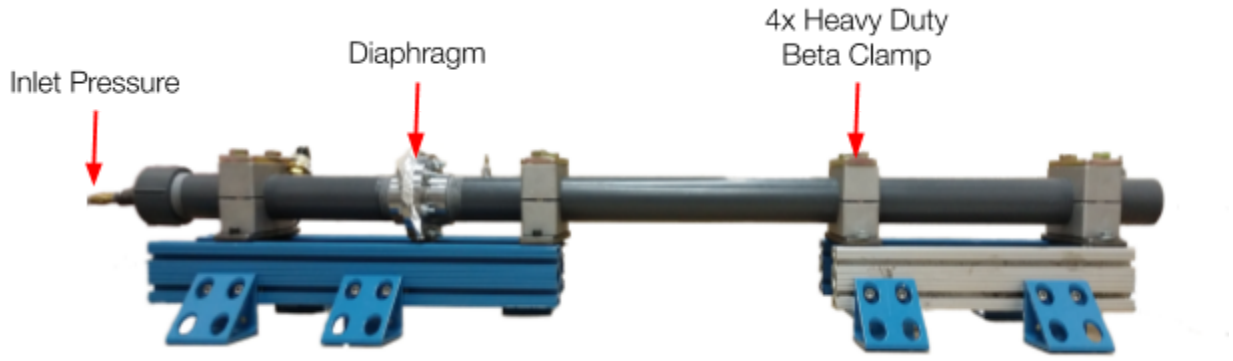

Figure 27. Experimental Shock Tube configuration

Figure 28 shows the final experimental arrangement, including the Shock Tube, rupture-imaging camera, Schlieren photography configuration, and sample placement. The Shock Tube was oriented on the optics table with room to place the Schlieren imaging setup at the exit of the Shock Tube to photograph the shock wave. The sample was placed at a distance from the tube exit to allow for imaging from another high speed camera to capture the interaction between the sample and shockwave and potential rupture. It is important to note that the inlet pressure into the Shock Tube is controlled by releasing wall pressure into a holding tank that's valve is opened and released into the driver section upon blast initiation.

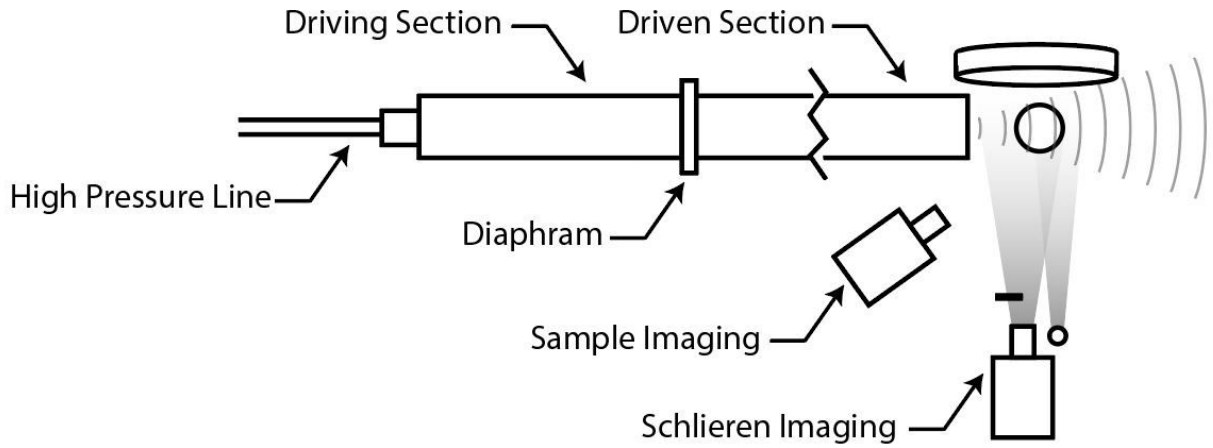

Figure 28. Experimental schematic with sampling and Schlieren imaging configuration

3.5. Experimental Configuration

3.5.1. Pressure Recording

Our group used a total of four pressure sensors to monitor the behavior of the Shock Tube. The placement of the sensors can be seen in Figure 29. The first pressure sensor, P1, was an Omega PX181B Pressure Sensor that was placed along the driver section, 1065 mm from the end of the

tube. This pressure sensor was used to monitor the static pressure in the driver section. The PX181B pressure sensor requires calibration before accurate measurements in the driving section can be made. We calibrated the sensor using a LabView Program given in Appendix E. The calibration requires a linear regression analysis for the linear equation in Equation 19, where V is volts and EU is Engineering Units.

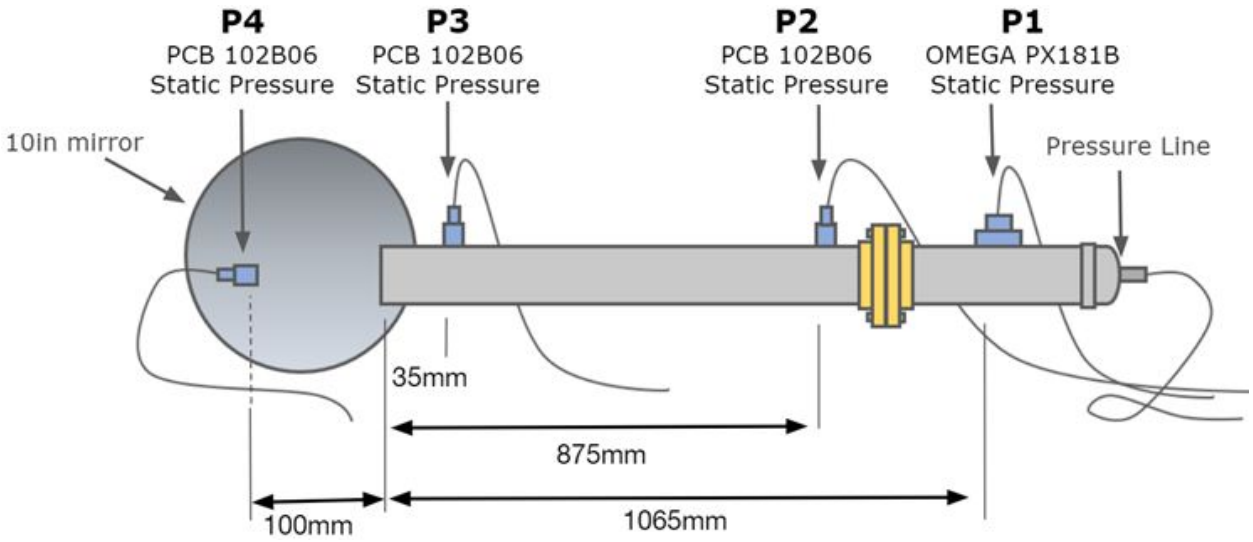

Figure 29. Pressure sensor placement

$$psi = V_{output}/(V/(EU)) - (Intercept) * EU \qquad (19)$$

The regression is based off plotting the ratio of output voltage to excitation voltage against a tank's pressure gauge readout. The slope and y-intercept from the linear regression analysis are used to adjust the mV readout from the transducer. The sensor is wired to the Data Aquisition Device according to the diagram in Figure 30. The sensor requires two analog inputs for output voltage and ground reference and one output for excitation voltage.

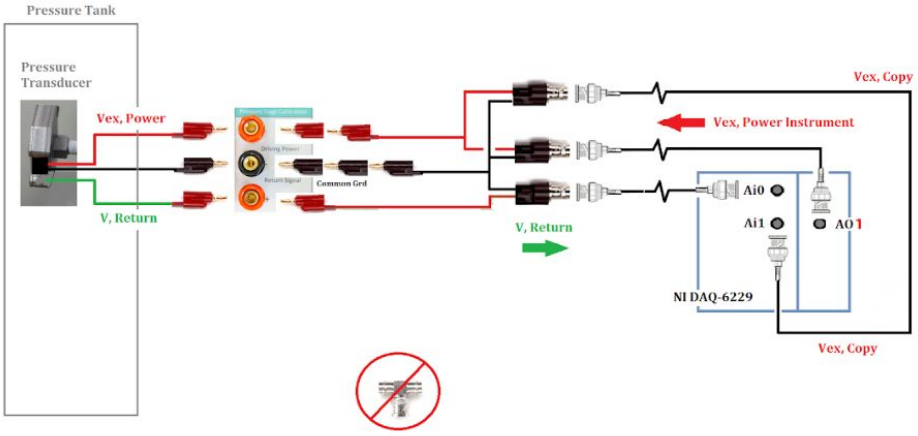

Figure 30. Static pressure transducer wiring diagram

The second pressure sensor, P2, was a PCB 102B06 Piezotronic sensor that was placed along the driven section, immediately past the diaphragm flange mount, 875 mm from the end of the tube. This sensor was placed here to detect the rupture of the diaphragm top trigger the recording of the Photron high speed cameras.

The third pressure sensor, P3, was a PCB 102B06 Piezotronic sensor that was placed at the end of the tube, 35 mm before the exit. The placement of this sensor allowed for the monitoring of the shock while in the tube. Theoretically once the shock is developed, there is no change in the values within the tube, so the exact placement of this sensor was chosen based on ease of placement.

The fourth pressure sensor, P4, was a PCB 102B16 Piezotronic sensor that was placed outside of the tube 100 mm away from the exit. It was placed here to measure the acoustic pressures that the sample is to experience. This pressure sensor could also be moved to variable distances away from the exit of the tube to understand the overpressure profile at different distances away from the exit of the Shock Tube.

The pressure sensors used in our in experimental setup were carefully chosen for the respective application. The Omega PX181B (P1) sensor was chosen for its ability to continuously and accurately read gauge pressure while compensating for temperature effects. The sensor requires an excitation voltage between 9 and 30 V DC and outputs a reading ranging from 1 to 5 V DC. The sensor readout Vout/Vex can be calibrated in order to have an accurate V/psi reading.

The two PCB 102B06 and one PCB 102B16 sensors were chosen for their ability to record high dynamic pressures at high sampling rates. Both the 102B06 and 102B16 are ground isolated and do not require a mV adjustment. The PCB 102B06 sensors are capable of reading dynamic pressures up to 3,450 kPa with a sensitivity of 1.45 mV/kPa. The PCB 102B16 sensor is capable of reading pressures up to 689.4 kPa and a sensitivity of 7.25 mV/kPa.

3.5.2. Data Acquisition

We used a National Instruments USB 6366 Data Acquisition (NI DAQ) and a PCB 482C Signal conditioner to collect the voltage signals from the four presser sensors and to trigger the Photron SA5 High Speed Camera. The USB 6366 NI DAQ has multiple analog-to-digital converters which allow for multiple analog output channels without ghosting effects. A simplified electronic wiring diagram is shown in Figure 31. The two PCB 102B06 and the one PCB 102B16 sensors were connected to the ICP channels of the PCB Signal Conditioner with a 10x gain. The three output channels from the Signal conditioner were connected to three analog input channels in the NI DAQ. The OMEGA PX181B pressure sensor was connected as described previously and the trigger channel of the Photron SA5 was connected directly to an analog output channel from the NI DAQ.

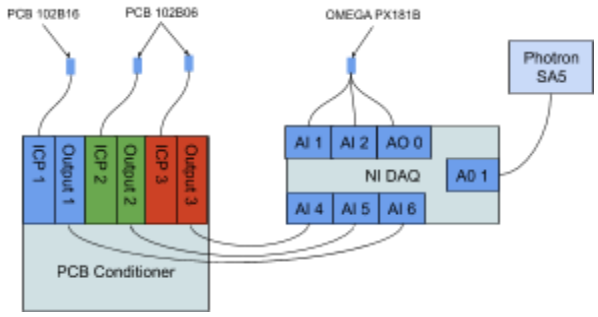

Figure 31. Electronic wiring diagram

We used two custom built Labview programs, one to acquire and visualize the pressure sensor data and trigger the Photron SA5 Camera at a low sampling rate and one to acquire and visualize the pressure sensor data at a high sampling rate. The first program allows for various user inputs, Figure 32. The first user inputs are the analog input channels, the sampling rate, and the samples per channel. We used a sampling rate of 50 kHz with 25,000 samples per channel in order to avoid overwrite and overflow errors. The second user inputs are the trigger analog output channel and the voltage trigger level. These two inputs control the channel that will trigger the Photron SA5 and the voltage level of the triggering pressure sensor that will start the camera recording. Once the voltage of the pressure sensor read the user defined voltage level, the NI DAQ outputted 5V DC from the user defined Analog Output channel. The final user inputs are the static pressure analog output channel and the slope and intercept values. The analog output channel is the excitation voltage for the OMEGA PX181B pressure sensor and the slope and intercept values are the same values determined from the calibration of the sensor.

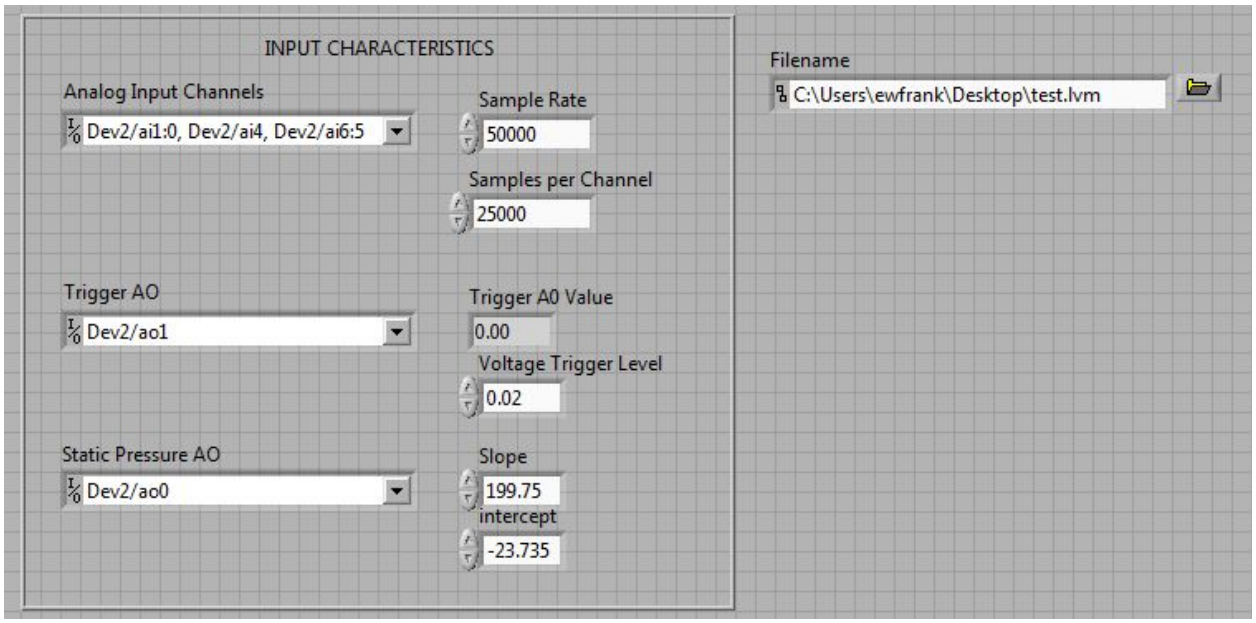

Figure 32. Labview front panel input characteristics

The Labview front panel has five graphs to show the voltage level of the four pressure sensors, shown in Figure 33. The top three graphs show the voltage level of the three PCB pressure sensors. The bottom left graph shows the ratio of the OMEGA PX181B pressure sensor input voltage and excitation voltage. The bottom right graphs shows the calibrated pressure of the OMEGA PX181B pressure sensor in psi. The Labview block diagram is shown in Appendix E.

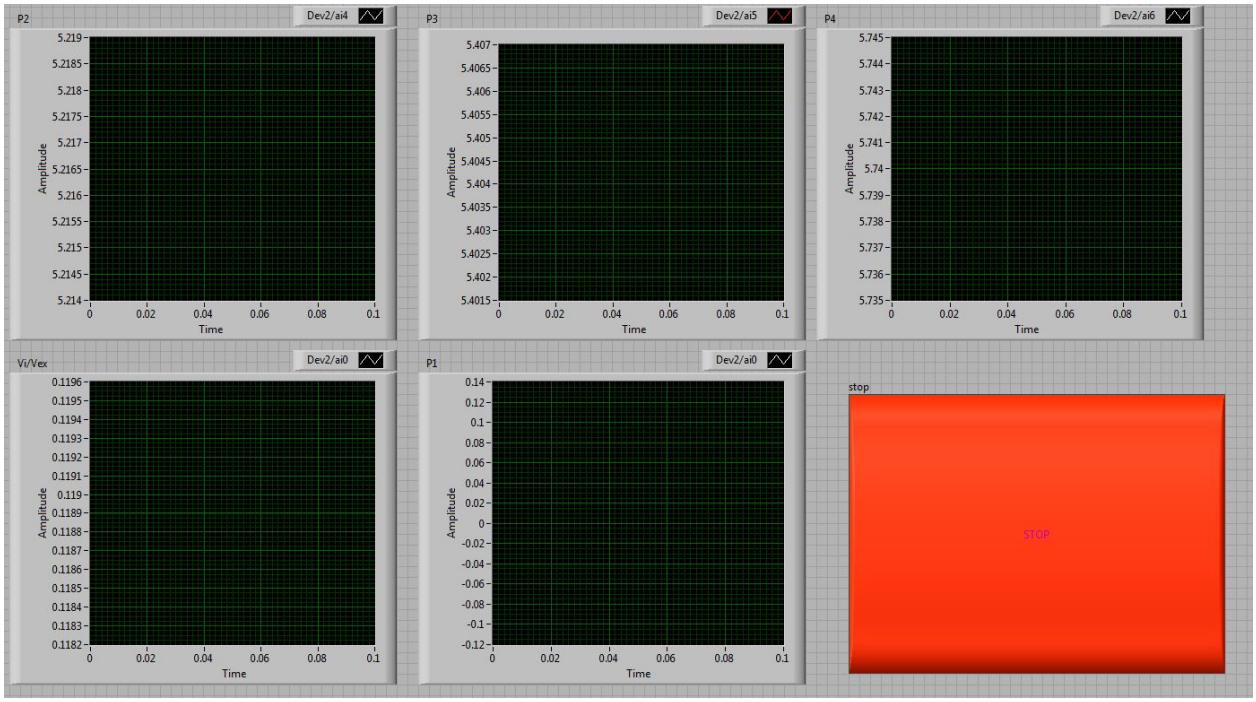

Figure 33. Labview front panel

We used the Photron FASTCAM Viewer software (PFV) to record and save Schlieren videos and to control the frame rate, shutter speed, resolution, and trigger mode of the SA5. In order to maximize the frame rate of the Schlieren videos we used a variable frame rate based on the resolution. The trigger mode of the camera was set to manual with 75% of the frames recorded before trigger.

Schlieren Photography was configured with the Shock Tube using the 10 in mirror with a focal length of 60 in. The mirror was placed 120 in away, twice the focal length, from the LED light source. We used a razor blade to deflect a portion of the light emitted by the LED. We used the Photron SA5 High Speed Camera to capture images of acoustic waves and air flow exiting the Shock Tube. The setup is shown in Figure 34.

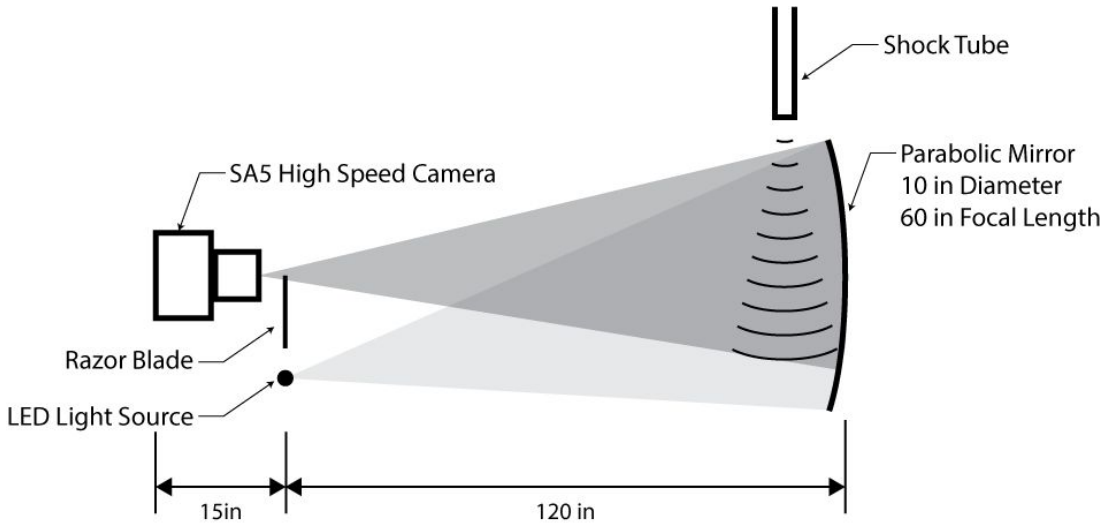

Figure 34. Shock tube Schlieren configuration

We used a second Labview program to acquire and visualize the experimental pressure sensor data at a high sampling rate. This program recorded the driving pressure data (P1) and the data of one other pressure sensor. The program has multiple input characteristics, similar to the first Labview program. We used a sample rate of 1,000,000 Hz with 1,500,000 samples per channel to record 1.5 seconds of experimental data. This runtime allowed us to record the full experiment without the need for precise synchronization. The Labview block diagram and front panel are given in Appendix F.

4. Results

After the construction of the Shock Tube, we conducted several experiments to understand the performance of our system. A detailed description of the experimental procedure can be found in Appendix G. In this section, we present the results of the experimental measurements and ANSYS Fluent simulation. We also present images from the blast of an artificial and cadaver membrane to validate our apparatus.

4.1. Experimental Results for Shock Tube Characterization

Figure 35 shows the P1 static pressure in the driving section vs time of three consecutive diaphragm ruptures recorded at 50 kHz. In the graph, time 0 was set as the time when the pressure in the driving section was at a maximum, corresponding to the rupture of the aluminum diaphragm. Pressure values before time 0 correspond to the slow increase of pressure in the driving section of the Shock Tube controlled by a ball valve. The maximum driving pressure of Shock 15 was 84.95 kPa, the maximum driving pressure of Shock 18 was 84.46 kPa, and the maximum driving pressure of Shock 19 was 86.15 kPa. The average maximum driving pressure was 84.80 kPa with a standard deviation of 820 Pa.

The data from P1 showed that the pressure increased in the driving section, with a different slope depending on how quickly the manual ball valve was opened. After the pressure in the driving section reached a peak value, the pressure values decreased rapidly corresponding to the rupture of the aluminum diaphragm. After the rupture of the diaphragm, the pressure values in the driving section oscillated about the x-axis in response to the reflected shock waves created when the shock wave exited the Shock Tube.

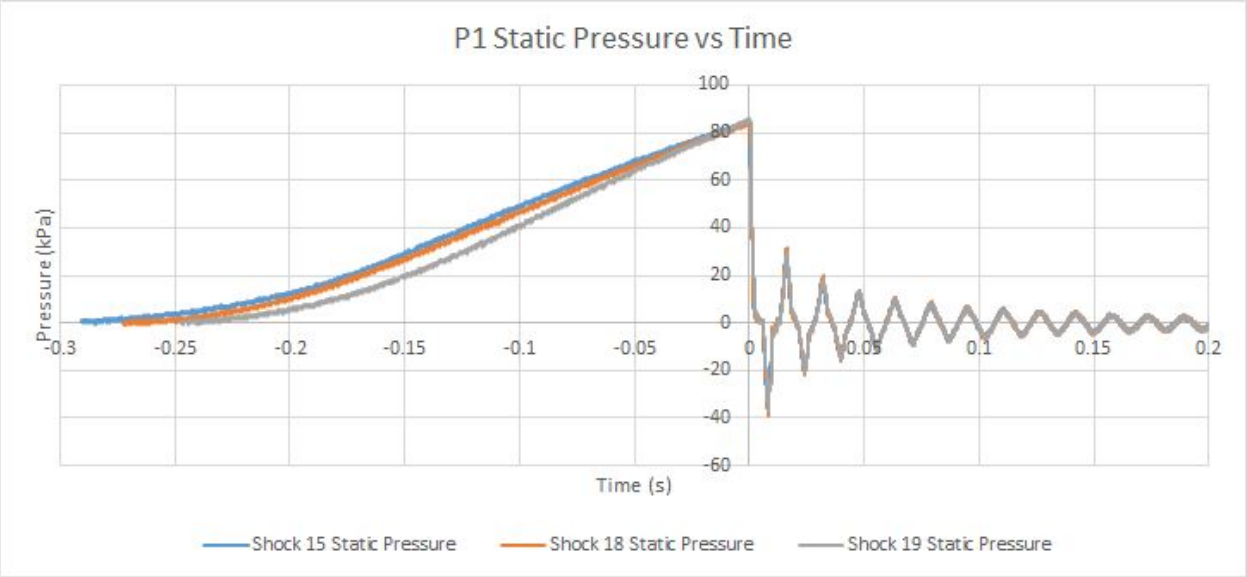

Figure 35. P1 driving static pressure vs time

Figure 36 shows the P3 static pressure 35 mm inside the Shock Tube vs time of three experimental diaphragm ruptures recorded at 1 MHz. In the graph, time 0 was set as the time when the pressure in the driving section was at a maximum, corresponding to the rupture of the aluminum diaphragm. The maximum pressure of Shock 15 was 42.3 kPa, the maximum pressure of Shock 18 was 40.8 kPa, and the maximum pressure of Shock 19 was 41.8 kPa. The average maximum pressure was 41.64 kPa with a standard deviation of 780 Pa.

The data from P3 showed one distinct peak in the first 10 ms after diaphragm rupture. At 2.1 ms there was a sharp increase in pressure to peak pressure followed by a plateau of high pressure. At the end of the pressure plateau, there was a sharp decrease in pressure decreased to a negative local minimum. After the local minimum, there was a slight increase in pressure followed by a second decrease in pressure to minimum pressure.

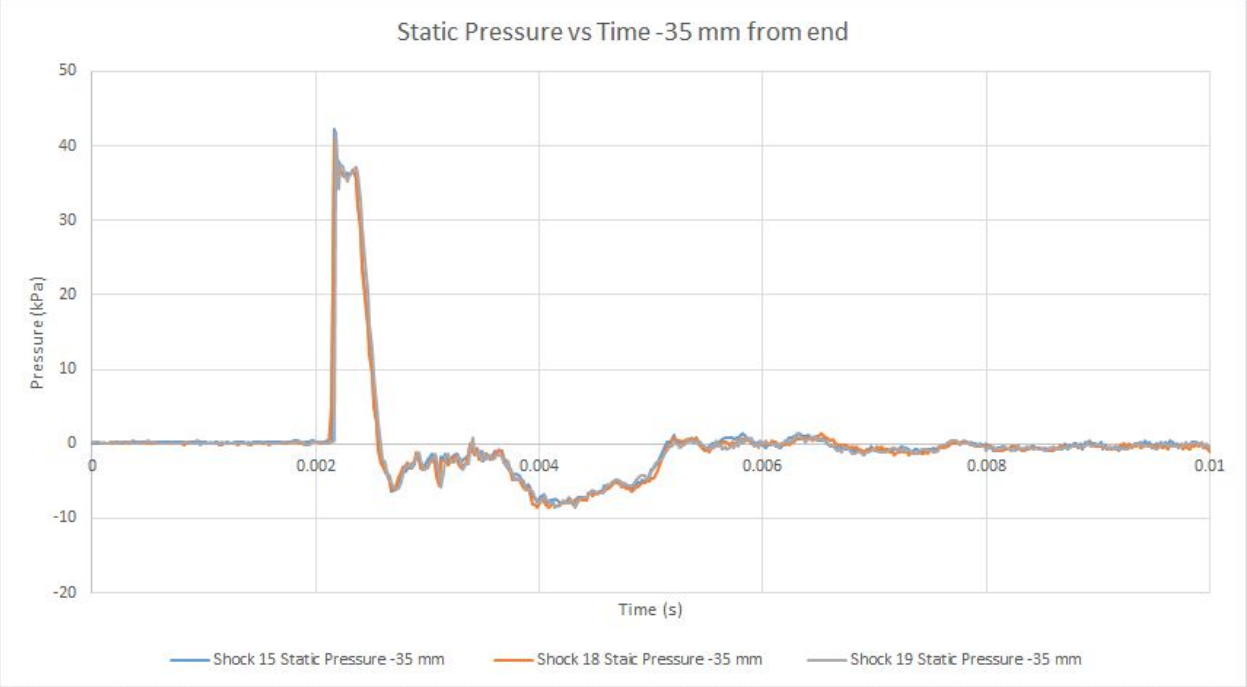

Figure 36. P3 static pressure vs time 35 mm inside the shock tube

Figure 37 shows the P4 stagnation pressure 50 mm outside the Shock Tube vs Time of three experimental diaphragm ruptures recorded at 1 MHz. In the graph, time 0 was set as the time when the pressure in the driving section was at a maximum, corresponding to the rupture of the aluminum diaphragm. The maximum pressure of Shock 45 was 79.6 kPa, the maximum pressure of Shock 47 was 78.6 kPa, and the maximum pressure of Shock 48 was 79.3 kPa. The average maximum pressure was 79.2 kPa with a standard deviation of 538 Pa.

The data from P4, 50 mm from the end of the tube, showed two distinct overpressures in the first 10 ms after diaphragm rupture. At 2.45 ms there was a sharp increase in pressure to maximum

pressure followed abruptly by a fall to atmospheric pressure. After reaching atmospheric pressure, the pressure increased to a local maximum, then slowly decreased back to atmospheric pressure.

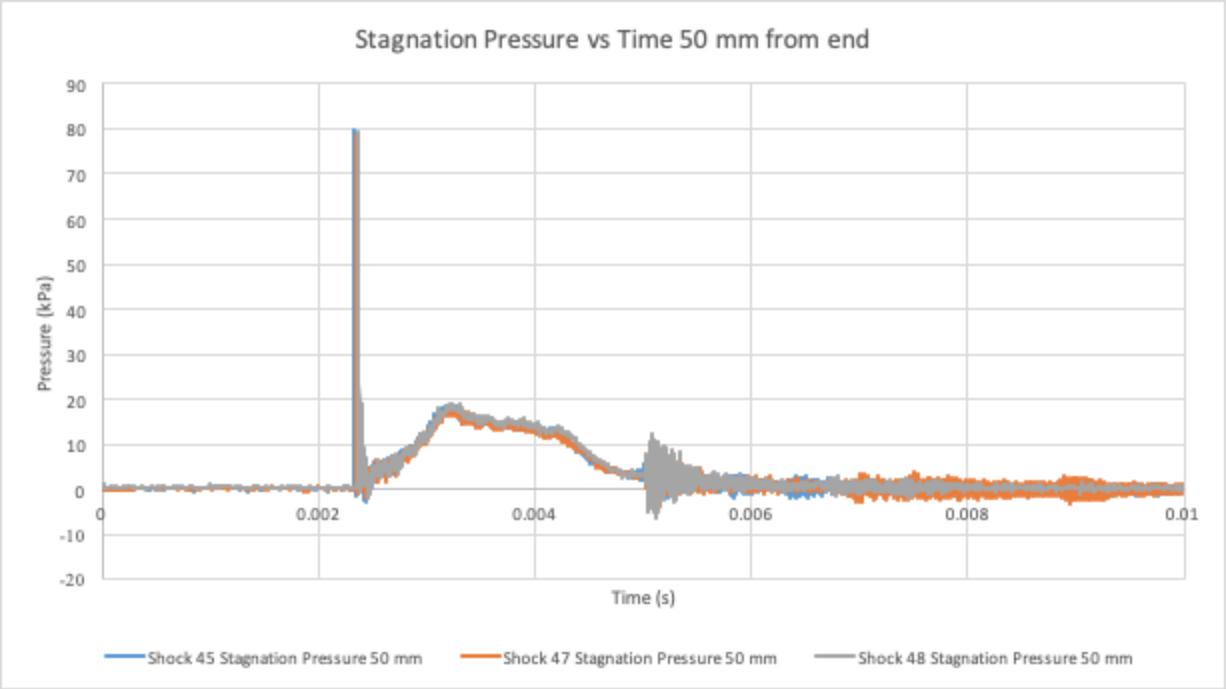

Figure 37. P4 stagnation pressure vs time 50 mm outside the shock tube

Figure 38 shows the P4 stagnation pressure 100 mm outside the Shock Tube vs Time of three experimental diaphragm ruptures recorded at 1 MHz. In the graph, time 0 was set as the time when the pressure in the driving section was at a maximum, corresponding to the rupture of the Aluminum diaphragm. The maximum pressure of Shock 36 was 27.3 kPa, the maximum pressure of Shock 38 was 27.7 kPa, and the maximum pressure of Shock 40 was 27.6 kPa. The average maximum pressure was 27.5 kPa with a standard deviation of 188 Pa.

The data from P4, 100 mm from the end of the tube, showed two distinct overpressures in the first 10 ms after diaphragm rupture. At 2.13 ms there was a sharp increase in pressure to maximum pressure followed abruptly by a fall to atmospheric pressure. After reaching atmospheric pressure there was an increase in pressure to 18.3 kPa, a local maximum. After the first local maximum there was a decrease in pressure followed by an increase in pressure to 14.83, a second local maximum. After the second local maximum the pressure decreased then increased slightly to a third local maximum of 4.3 kPa before returning to atmospheric pressure.

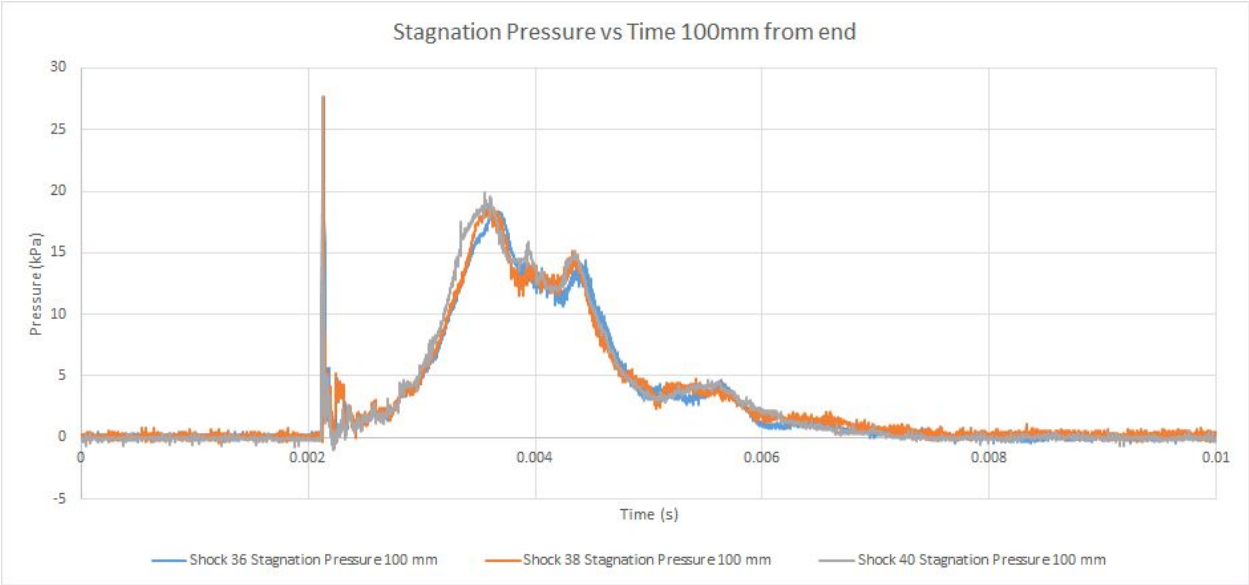

Figure 38. P4 stagnation pressure vs time 100 mm outside the shock tube

4.2 ANSYS Results for Shock Tube Validation

We used the results from the experiments of the Shock Tube as the initial conditions of the ANSYS Fluent Simulation described in Section 3.3.4. First, the driver section shown in red in Figure 39 was created using the adapt region command in ANSYS Fluent. Next, the mesh was initialized using a hybrid initialization and the region created was patched with the initial pressure and temperature values determined from the Shock Tube experiments. From experimental data, the aluminum disk used as the diaphragm material in the Shock Tube ruptured at an average pressure of 85 kPa. The initial pressures in the driven section and the atmospheric section were set to atmospheric pressure, 0 kPa. The initial temperature of the driver, driven, and atmospheric section were set to average room temperature, 24.85 C (298 K). Once initial conditions were set, the time step was set to 50 microseconds, the max iterations per time step was set to 350, and the number of time steps was set to 30,000 for a simulation time of 0.015 seconds.

The convergence of the simulation was determined by completing multiple simulations of varying mesh density and time step. The resulting pressure vs time graphs at 35 mm inside the tube were compared to balance simulation accuracy with simulation time. The final simulation took 26 hours to run. The results of the simulation were used to determine transient pressure values at points corresponding to the pressure sensor locations in the Shock Tube experiments and to create density contour maps.

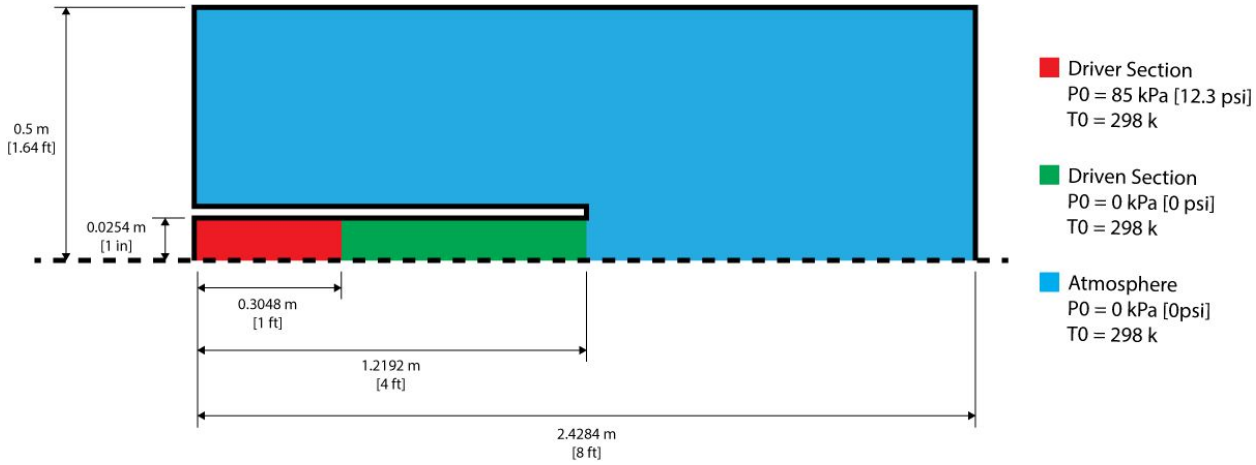

Figure 39. ANSYS Fluent initial conditions

Figure 40 shows the averaged experimental data of three shocks plotted against the ANSYS simulation results at 35 mm inside the Shock Tube (P3). The maximum experimental pressure was 38.9 kPa and the maximum ANSYS pressure was 34.5 kPa, a relative difference of 12.1%. The positive duration of the experimental data was 0.44 ms and the positive duration of the ANSYS simulation was 0.50 ms, a relative difference of 12.8%. The minimum experimental pressure was -8.13 kPa and the minimum ANSYS pressure was -8.23 kPa, a relative difference of 1.22%.

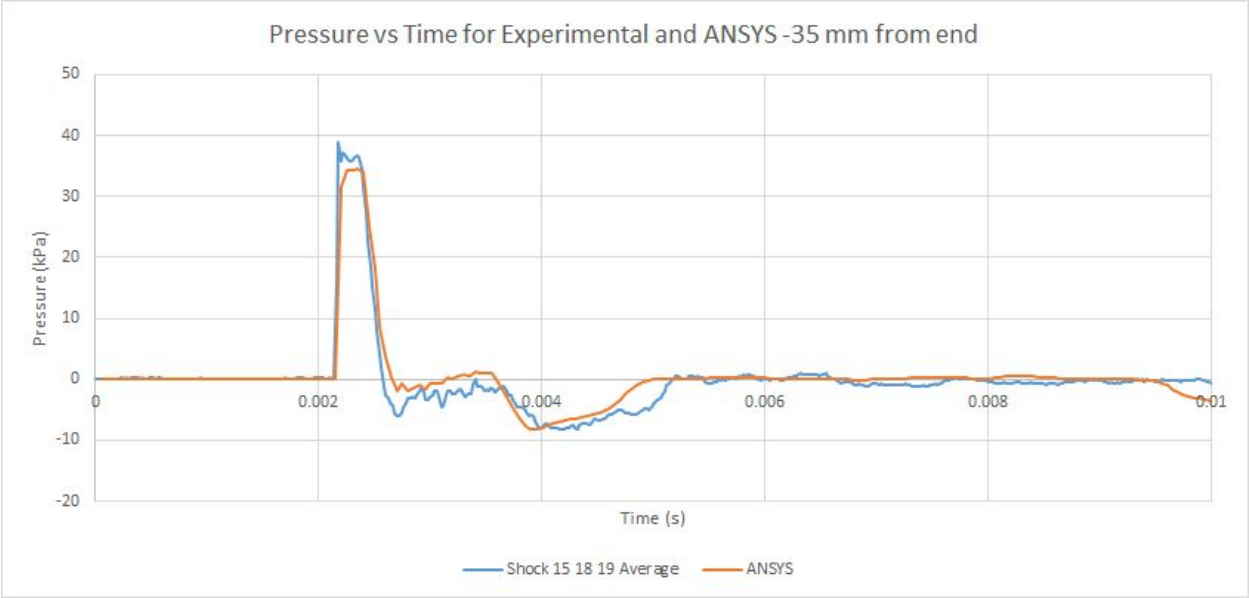

Figure 40. Pressure vs time for experimental and ANSYS 35 mm inside tube

Figure 41 shows the averaged experimental data of three shocks plotted against the ANSYS simulation results at 50 mm outside the Shock Tube (P4). The maximum experimental pressure of the shockwave was 78.6 kPa and the maximum ANSYS pressure of the shock wave was 10.3 kPa, a relative difference of 153%. The maximum experimental pressure of the second

overpressure was 18.2 kPa and the maximum ANSYS pressure of the second overpressure was 18.2 kPa, a relative difference of 11.6%.

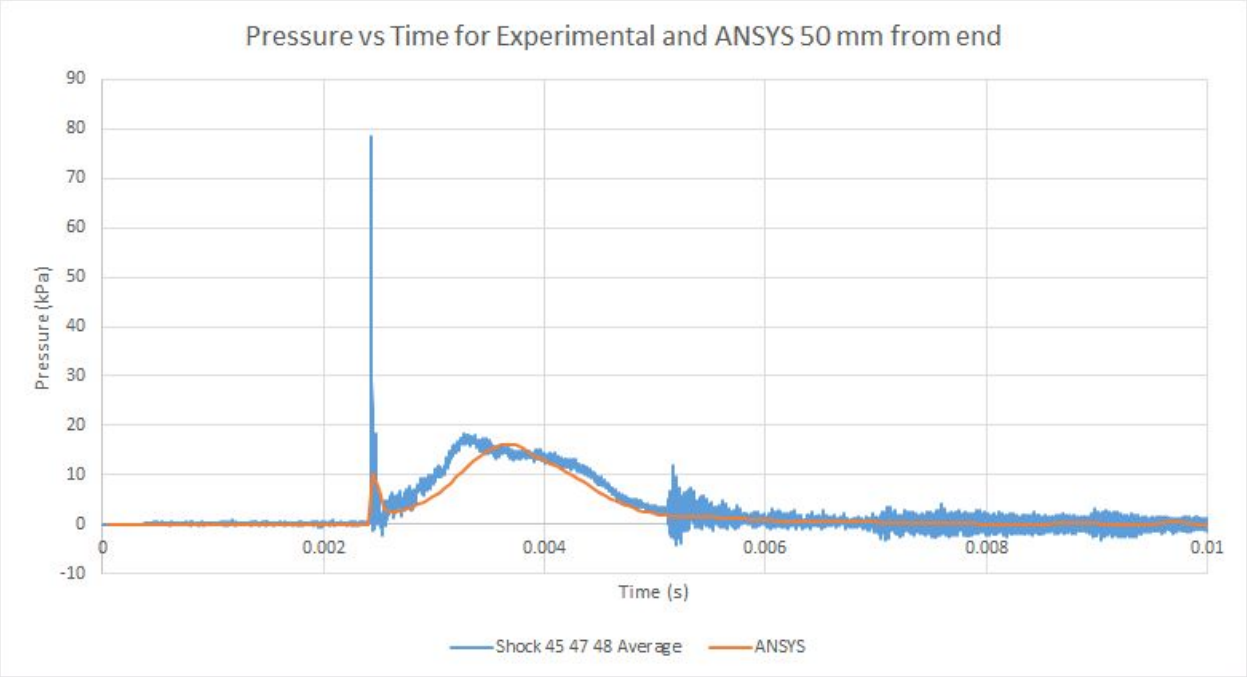

Figure 41. Pressure vs time for experimental and ANSYS 50 mm outside the tube

4.3. PFA Analysis for Thermodynamic Validation

We used Photron FastCAM Analysis (PFA), a motion analysis software, to quantify the Schlieren photography results captured by the Photron SA5 camera. The software uses trackers to track the distance a point travels between frames. Using the frame rate, PFA calculates the distance, velocity, and acceleration of each point. We used this software's capabilities to calculate the speed of the acoustic waves that propagated from the end of the Shock Tube. Figure 42 shows a screenshot from the software with three trackers placed along the front of the shock wave.

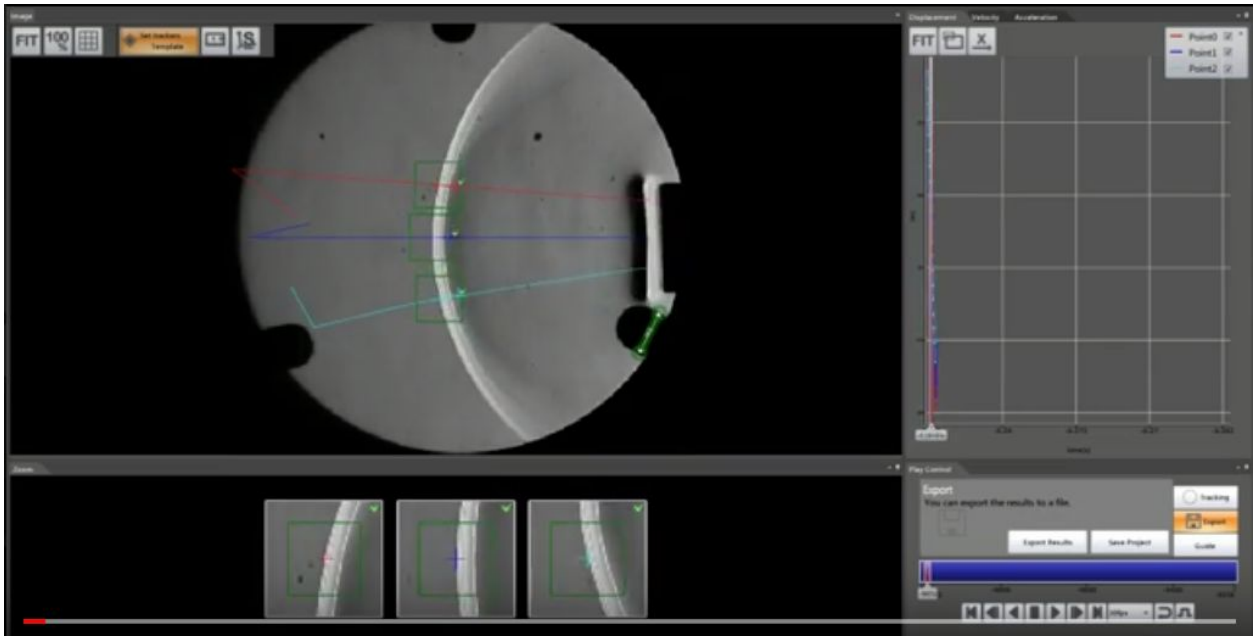

Figure 42. PFA software tracking the speed of a shockwave

The three trackers calculated the average speeds to be 371.84 m/s, 375.49 m/s, and 373.65 m/s, for an overall average speed of 373.66 m/s. Given that the speed of sound is 343 m/s, the speed of the first wave exiting the Shock Tube breaks the sound barrier at a Mach number of 1.09. A relative difference of 4.4% when compared to the calculated Mach number of 1.14.

4.4. Study of Shock Tube Application to an Artificial Membrane

We conducted experimental trials with our Shock Tube against Teflon samples. We used Teflon due to its similar microstructure to the human TM. We placed a Teflon sample in a circular 10 mm diameter holder designed to eliminate stress concentrations. The holder and Teflon sample were placed 50 mm away from the end of the Shock Tube directly facing the opening as seen in Figure 43.

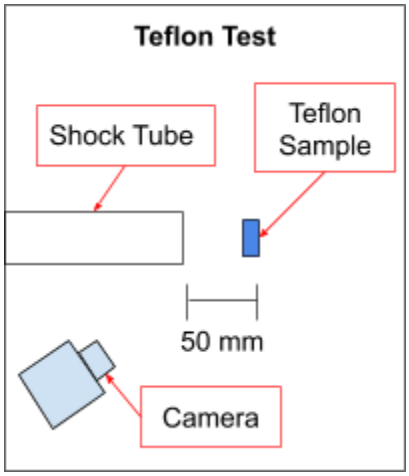

Figure 43. Teflon test setup

Figure 44 shows the rupture sequence after exposure to 80 kPa (192 dB SPL). At this distance the Teflon sample ruptured, proving the Shock Tube is capable of breaking samples with a high pressure front.

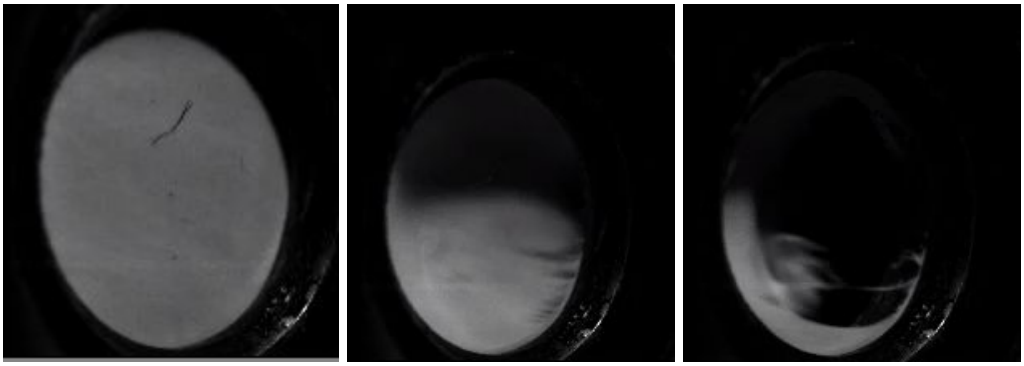

Figure 44. Teflon tape sample rupture sequence

Although the microstructure of Teflon closely resembles that of the TM, the material properties of Teflon vary between the axial and radial directions. The TM properties remain more constant in both directions. This difference in structure causes discrepancies in the deformations and behaviors during the blast.

4.5. Study of Shock Tube Application to a Cadaver Membrane

After experimenting on the known Teflon samples, our team tested the Shock Tube on human cadaver TMs provided by Massachusetts Eye and Ear. In the first test, the TM sample was placed 50 mm away from the end of the tube at slight angle to allow for imaging of the membrane, shown in Figure 45. After several blast attempts we were unable to rupture the cadaver TM. In a second test, we reoriented the sample to directly face the shock wave. While this caused more motion of the TM, it still failed to rupture.

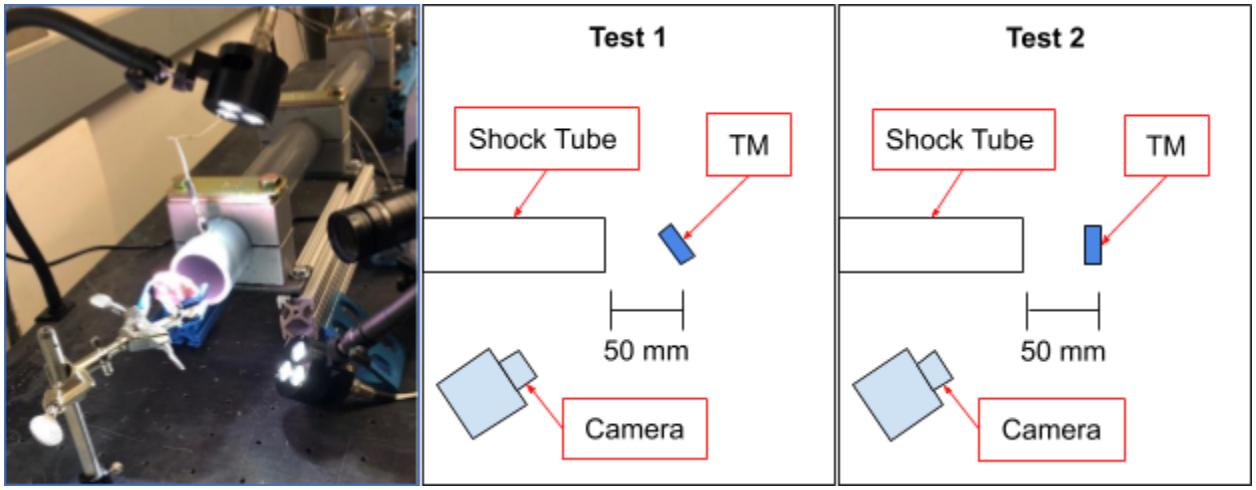

Figure 45. Experimental TM setup with DIC

In order to prove that the Shock Tube was capable of providing sufficient acoustical pressures, in test three, we placed the TM sample facing the end of the tube at point blank range (0 mm). At this distance the TM was loaded with an acoustic pressure of 196 dB SPL. As seen in Figure 46, the shock wave ruptured the TM, however, at this distance we were unable to record high speed videos due to the visual interference with the Shock Tube.

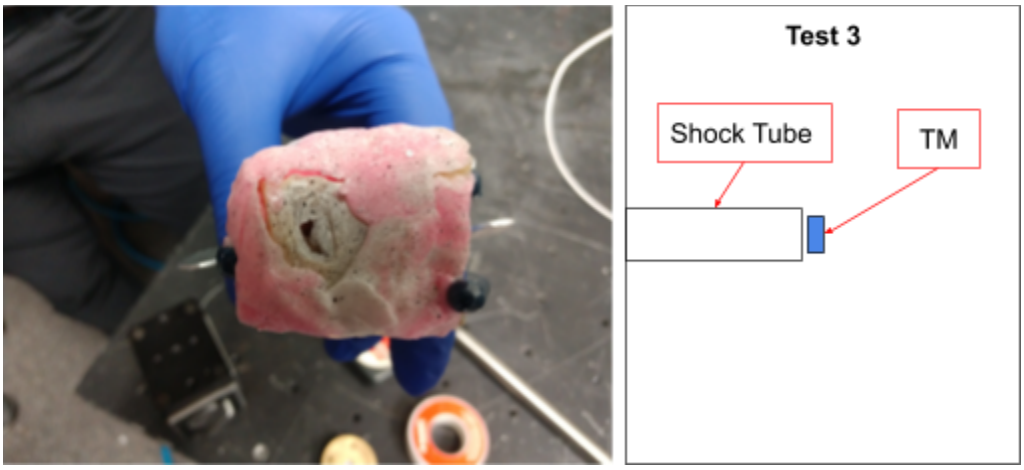

Figure 46. Ruptured TM sample

In order to rupture the TM farther away from the end of the Shock Tube to allow for high speed video recording, we needed to increase the overpressure outside of the Shock Tube. To increase the overpressure outside the Shock Tube, we increased the driving pressure by using two Aluminum diaphragms. The Thin Disk Theory from Equation 10 implies that doubling the thickness of the diaphragm material will quadruple the rupture pressure. However, the new rupture pressure was approximately only double at 158 kPa, as compared to 84.8 kPa with a single diaphragm.

We placed a second cadaver TM sample 50 mm away from the end of the tube and oriented the silicone putty on the sample to expose the canal behind the TM, shown in Figure 47. This ensured that the atmospheric conditions existed on both sides of the TM. At this distance directly facing the tube, the sample underwent large out-of-plane motion in response to the shock wave, but rupture still did not occur. Figure 48 shows the out of plane motion sequence from the double diaphragm blast. We can see that the surface of the TM is damaged during the displacement.

Figure 47. TM secured with reconfigured putty and clamp system

Figure 48. TM excitation 50 mm from end of shock tube

5. Discussion

Using the pressure sensor data from P1, P3, and P4 we were able to characterize the behavior inside and outside of the Shock Tube and determine that the device was highly repeatable. Using the data from P4, we were able to confirm that the Shock Tube created a shock wave. Figure 49 shows the P4 stagnation pressure 50 mm outside the Shock Tube vs Time for Shock 47 compared to the theoretical Friedlander waveform. The behavior of the experimental pressure matches with the expected behavior until the negative duration of the Friedlander waveform. We believe this difference between the theoretical and experimental is due to the fact that the P4 pressure sensor measured the stagnation pressure of the shock wave. The stagnation pressure includes the pressure inherent in stopping the moving fluid. This increase in pressure would shift the the negative pressure typical of a Friedlander waveform above the x-axis.

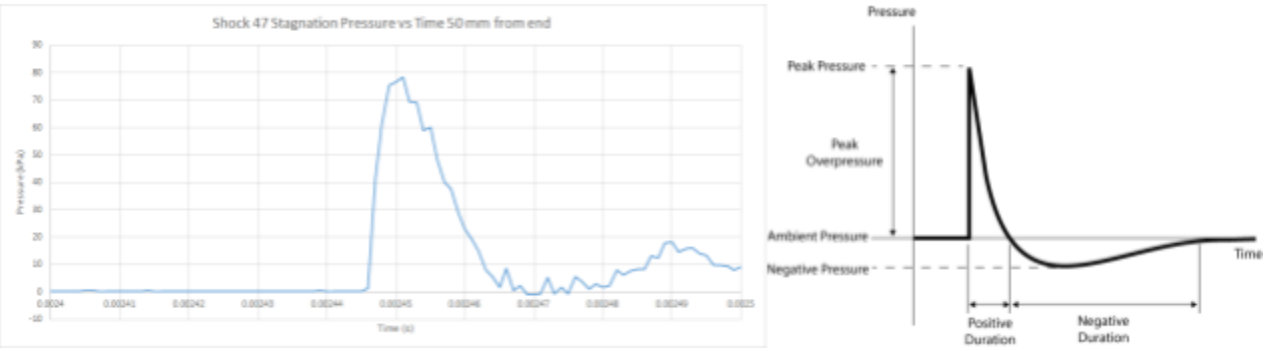

Figure 49. Experimental comparison to theoretical Friedlander waveform

With the use of high speed Schlieren Imaging and ANSYS Fluent simulations, we can visually see the shock wave and verify its behavior with recorded pressure measurements. Figure 50 shows the comparison between the experimental stagnation pressure results, 100 mm away from the end of the tube, with high-speed Schlieren images and images from a density contour map created from the ANSYS simulation.

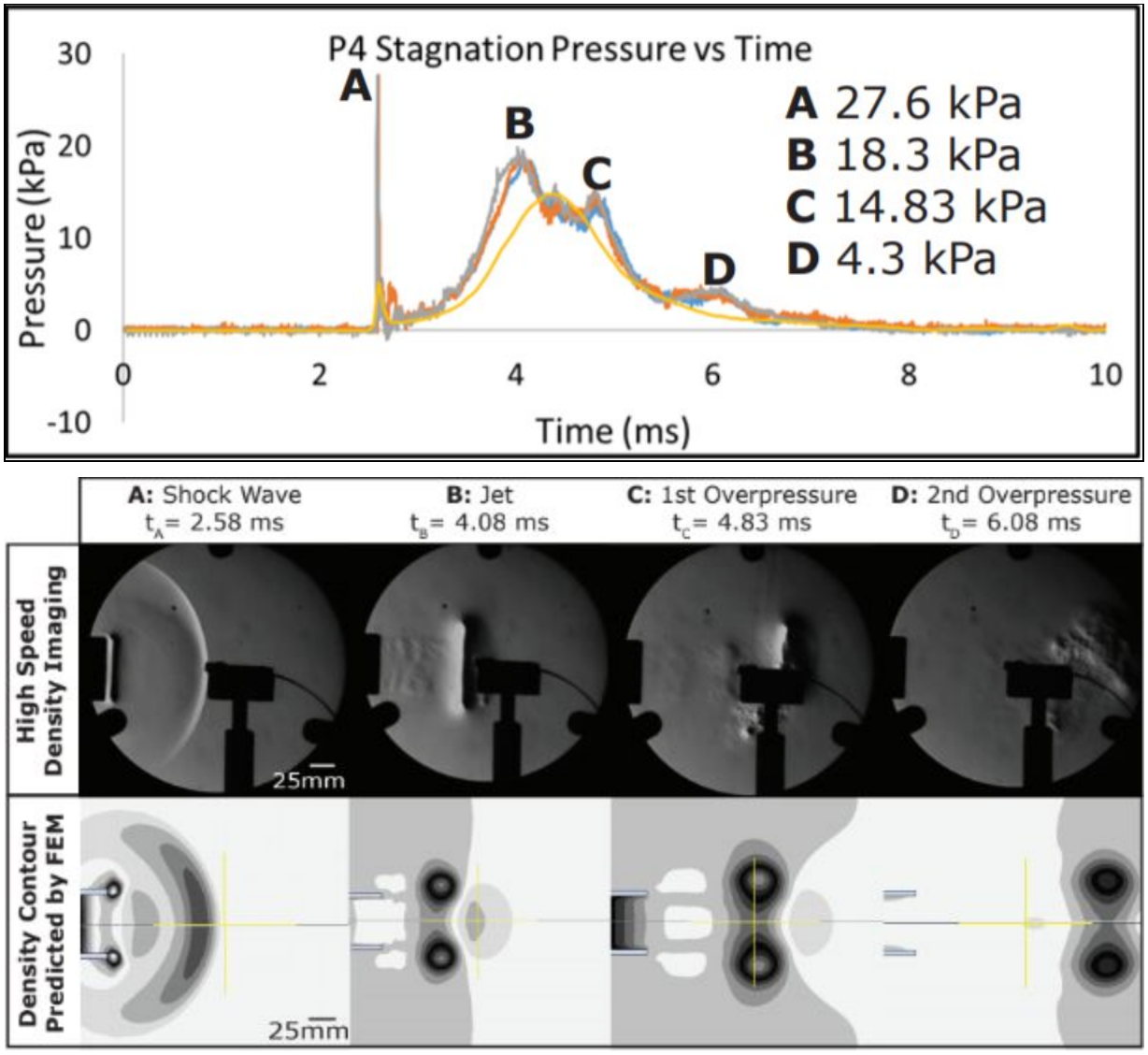

Figure 50. Experimental and computational results compared with Schlieren

Point A on the graph was the shock wave pressure peak, 2.58 ms after the rupture of the diaphragm. The time of this peak corresponded to the Schlieren image A and the density contour image A. Point B was a high pressure jet following the shock wave, 1.5 ms after the shock wave. The time of this peak corresponded to the Schlieren image B and the density contour image B. The jet behaved like a vortex ring and can be seen in both the Schlieren imagery and contour map.

The expelled jet or vortex ring is created when a high density medium is pushed into a fluid through a tube into a stationary region of the same fluid. The vortex ring travels at a much slower rate than the preceding shockwave. The smaller pressure peaks (C and D) following the initial vortex ring are a result of the reflected waves exiting the tube. Figure 51 shows a typical vortex ring as it exits an orifice, labeled with its physical phenomena. The geometry of the typical vortex ring matches our experimental Schlieren imaging (Arakeri, Das, Krothapalli, & Lourenco, 2004).

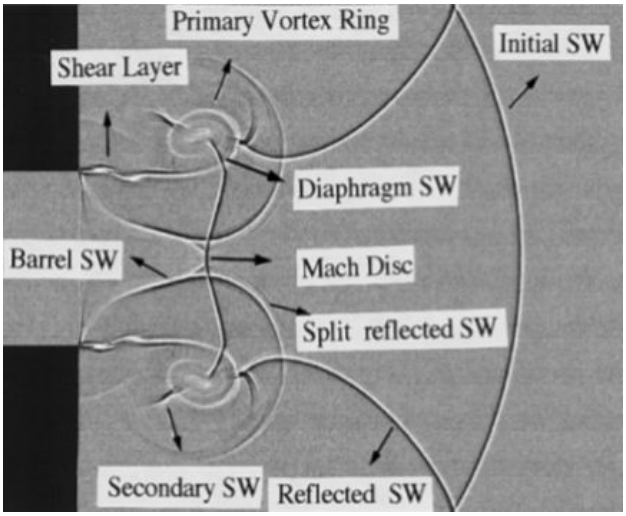

Figure 51. Schlieren diagram of a shock exiting a shock tube (Holmberg, 2010)

Following the first two peaks, were points C and D, the first and second overpressure at time 4.83 ms and 6.08 ms after rupture respectively. The time of points C and D corresponded to the Schlieren images C and D and to the density contour images C and D.

The ANSYS Fluent simulation was able to closely match the experimental values inside of the tube. At the P3 position in the Shock Tube, the ANSYS simulation was able to predict the peak pressure to within 12%, the positive duration to within 12%, and the minimum pressure to within 1.5%. The error between experimental and simulation may be due to boundary effects of the tube or due to the simulation assumptions. Inside the tube, we were able to use the ANSYS simulation as a predictor of shock behavior.

Outside of the tube, the simulation was unable to accurately predict the exact behavior of the blast. At the P4 position, 50 mm from the end of the Shock Tube, there were large differences between the experimental and simulation values. The difference may be due to atmospheric influences as the shock wave exited the Shock Tube. Outside the tube, we are not able to use the ANSYS simulation to predict pressures of the shock wave, however, we are able to use the simulation to predict the timeline at which pressure phenomenon occur.

6. Conclusion and Recommendations for Future Work

Our team designed, constructed, and characterized a Shock Tube with adjustable blast capabilities, dependent upon the chosen diaphragm. The Shock Tube has met our objectives and constraints, as it can produce blasts that reach pressures greater than 150 dB SPL, while fitting within a confined lab space. Using a single aluminum diaphragm, we were able to rupture a human cadaver TM at the end of the Shock Tube with a pressure of 196 dB SPL. Our Shock Tube will enable future Tympanic Membrane fracture studies to ultimately lead to the creation of better hearing protection.

After completing multiple experiments to characterize and validate the Shock Tube, we developed several recommendations to improve the experimental procedure. First, we recommend the use of a different diaphragm material. Using one Aluminum diaphragm, we were able to rupture human cadaver Tympanic Membranes at the end of the Shock Tube, however, at this distance, we were unable to image the rupture. We recommend the use and characterization of a different diaphragm material that will rupture at a higher driving pressure, creating a higher overpressure at the exit of the tube. With higher overpressure at the exit of the Shock Tube, the Tympanic Membrane can be ruptured farther away from the end of the Shock Tube, allowing room for imaging.

Second, we recommend the investigation of a smaller Schlieren configuration to fit in a more compact area. The mirror we used in our study requires a distance of 10 feet. With further investigation and potentially different configurations, the Schlieren can be optimized to fit within the constraints of the optics table dimensions.

Finally, we recommend the the Tympanic membrane sample to be oriented perpendicular to the oncoming shock wave as it will rupture at a lower pressure in this orientation (Gan, Leckness, Nakmali, & Ji, 2018). The new orientation will not only allow the TM sample to be ruptured farther from the end of the Shock Tube, but will also allow for easier imaging since the camera can directly face the surface of TM. A possible new experimental configuration, taking into account this reorganization is shown as a schematic in Figure 52.

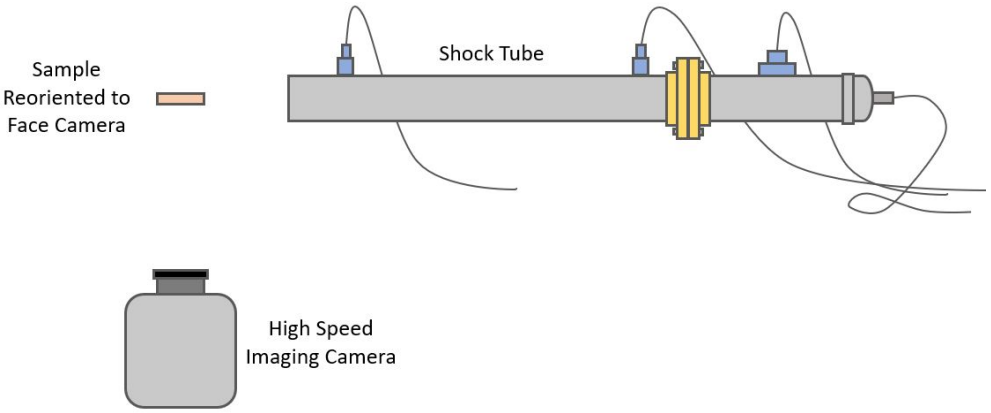

Figure 52. New sample rupturing configuration

With the addition of these recommendations, we are confident that our Shock Tube will enable the novel research on middle-ear fracture mechanics.

7. References

Arakeri, J. H., Das, D., Krothapalli, A., & Lourenco, L. (2004). Vortex ring formation at the open end of a Shock Tube: A particle image velocimetry study. Physics of Fluids,16(4), 1008-1019. doi:10.1063/1.1649339

Beardmore, R. (2013, February 20). Loaded Flat Plates. Retrieved from http://www.roymech.co.uk/Useful_Tables/Mechanics/Plates.html
Saunders, G., & Griest, S. (2009). Hearing loss in veterans and the need for hearing loss prevention programs. *Noise and Health, 11*(42), 14. doi:10.4103/1463-1741.45308

Bokil, M. (2010). Characterization of the Pressure Wave From a Shock Tube Using Numerical Simulations. The University of Utah Graduate School. Retrieved from https://www.researchgate.net/profile/Eric_Hall4/post/What_is_the_difference_between_shock_wave_and_blast_wave/attachment/59d61da679197b8077978b4b/AS:272115930992641@1441888902565/download/CHARACTERIZATION OF THE PRESSURE WAVE FROM A Shock Tube USING NUMERICAL SIMULATIONS.pdf.

Broadband Noise Source Models. (2006, August 20). Retrieved from https://www.sharcnet.ca/Software/Fluent6/html/ug/node795.htm

Cho, S., Gao, S. S., Xia, A., Wang, R., Salles, F. T., Raphael, P. D., . . . Oghalai, J. S. (2013). Mechanisms of Hearing Loss after Blast Injury to the Ear. PLoS ONE,8(7). doi:10.1371/journal.pone.0067618

Gan, R. Z., Leckness, K., Nakmali, D., & Ji, X. D. (2018). Biomechanical Measurement and Modeling of Human Eardrum Injury in Relation to Blast Wave Direction. Military Medicine,183(Suppl_1), 245-251. doi:10.1093/milmed/usx149

Hall, N. (Ed.). (2018, April 6). Normal Shock Wave. Retrieved from https://www.grc.nasa.gov/www/k-12/airplane/normal.html

Harris, T. (2019). How Hearing Works. Retrieved from https://health.howstuffworks.com/mental-health/human-nature/perception/hearing.htm

Helfer, T. M., Jordan, N. N., & Lee, R. B. (2005). Postdeployment hearing loss in U.S. Army soldiers seen at audiology clinics from April 1, 2003, through March 31, 2004. Am J Audiol 14: 161–168.

Holmberg, A. D. (2010). Development and Characterization of Shock Tubes For Laboratory Scale Blast Wave Simulation. Engineering Mechanics Dissertations & Theses. Retrieved from https://digitalcommons.unl.edu/cgi/viewcontent.cgi?article=1027&context=engmechdiss.

Huynh, D. (2013). Experimental Design of a Shock Tube For the Time Response Study of Porous Pressure-Sensitive Paint (J. Gregory & M. Zhuang, Eds.). The Ohio State University. Retrieved November 11, 2018, from https://kb.osu.edu/bitstream/handle/1811/54404/1/David_Huynh_Honors_Thesis.pdf.

Jagadeesh, G. (2008, August). Fascinating World of Shock Waves. Resonance. Retrieved from https://www.ias.ac.in/article/fulltext/reso/013/08/0752-0767

Kurian, J. (n.d.). Shock Tube. Experimental Aero(Gas) Dynamics,1-26. Retrieved from https://nptel.ac.in/courses/101106040/chapter 3.pdf.

Luo, H., Jiang, S., Nakmali, D. U., Gan, R. Z., & Lu, H. (2015). Mechanical Properties of a Human Eardrum at High Strain Rates After Exposure to Blast Waves. Journal of Dynamic Behavior of Materials, 2(1), 59-73. doi:10.1007/s40870-015-0041-3

Menter, Florian. (1993). Zonal Two Equation k-w Turbulence Models For Aerodynamic Flows. AIAA Paper. 1993. 10.2514/6.1993-2906.

Nakagawa, A., Manley, G. T., Gean, A. D., Ohtani, K., Armonda, R., Tsukamoto, A., . . . Tominaga, T. (2011). Mechanisms of Primary Blast-Induced Traumatic Brain Injury: Insights from Shock-Wave Research. Journal of Neurotrauma,28(6), 1101-1119. doi:10.1089/neu.2010.1442

Noise-Induced Hearing Loss. (2017, February 7). Retrieved from https://www.nidcd.nih.gov/health/noise-induced-hearing-loss

Occupational Noise Exposure. (n.d.). Retrieved from https://www.osha.gov/SLTC/noisehearingconservation/

Rapp, B. E. (2017). In Rapp B. E. (Ed.), Chapter 6 - thermodynamics. Oxford: Elsevier. doi://doi.org/10.1016/B978-1-4557-3141-1.50006-X

Realizable K-Epsilon Model. (2009, January 23). Retrieved from http://www.afs.enea.it/project/neptunius/docs/fluent/html/th/node60.htm#13902
Density-Based Solver. (2006, September 20). Retrieved from https://www.sharcnet.ca/Software/Fluent6/html/ug/node988.htm

Schlieren Optics. (2019). Retrieved from https://sciencedemonstrations.fas.harvard.edu/presentations/schlieren-optics

Sengpiel, E. (n.d.). Damping of Sound Level (Decibel dB) vs. Distance. Retrieved from http://www.sengpielaudio.com/calculator-distance.htm

Settles, G. S. (2013). *Schlieren and shadowgraph techniques: Visualizing phenomena in transparent media*. Berlin: Springer. doi:10.1007/978-3-642-56640-0

Young, H. D., Freedman, R. A., & Ford, A. L. (2016). *University physics with modern physics* (14th ed.). Harlow, Essex: Pearson.

8. Appendix

Appendix A:

Compressible Flow Experiment

In preparation for the creation and data analysis of a Shock Tube, we first worked to familiarize ourselves with the process of data collection across a two-tank system operating in real-time. In this system, the first air tank would release pressurized air through a valve into a smaller secondary tank that was open to the atmosphere via a nozzle. The experimental configuration of the experiment can be seen in Figure 1A.

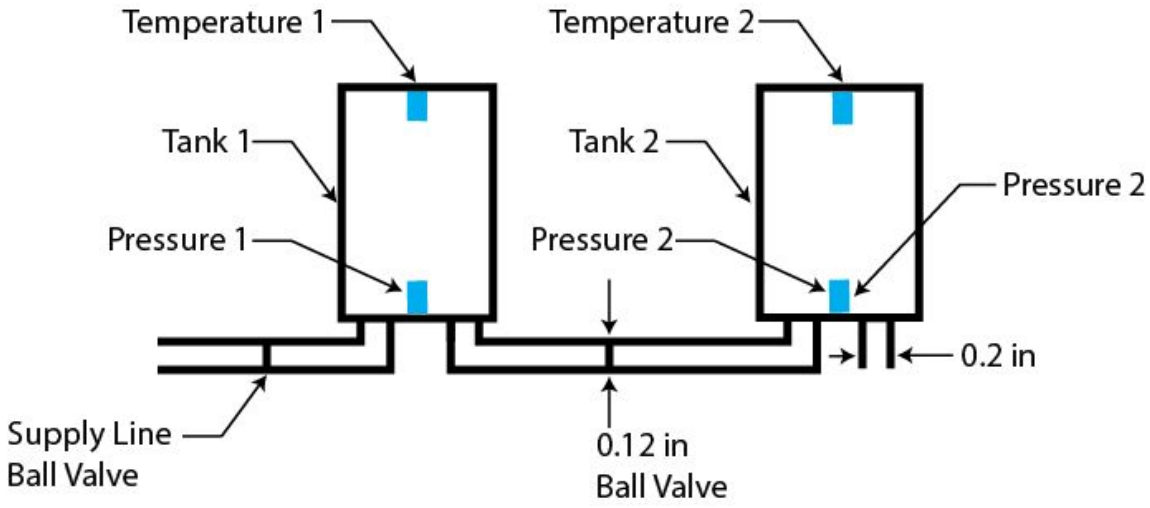

Figure 1A. Diagram of a two tank system where pressurized air is released via a nozzle into a second tank at atmospheric conditions

The following sections cover the necessary background and methodology to accomplish the two-tank analysis, as well as the influence the results had on our methodology and functional specifications for the final design.

Numerical Modeling in Matlab

We performed a numerical computational analysis using Matlab so that we could familiarize ourselves with the mathematical properties and thermodynamics of the system. A vital concept within these calculations was the relation of the critical pressure ratio to choked and unchoked flow. As seen in Equation 1A, the critical pressure ratio is the ratio of the pressure within the tank to the pressure into which the gas discharges, and this ratio corresponds to the maximum flow. The MatLab program evaluates the instantaneous pressure ratios as pressure moves from Tank 1 to

Tank 2, and compares this new pressure ratio to the critical pressure ratio. Using “if statements” within MatLab allows the program to determine whether it is necessary at that point in the system to use the choked or unchoked fluid equation for the mass flow rate. If the newly found pressure ratio is less than the critical pressure ratio, it is assumed that the flow is choked, and Equation 2A is implemented. If it is found to be greater than the critical pressure ratio, the flow is considered unchoked, and Equation 3A is implemented. It is important to note that the geometry of the nozzle used plays a critical role and can greatly affect the pressure ratio.

$$\frac{P_0{}^*}{P_t} = \left(\frac{2}{k+1}\right)^{\frac{k}{k-1}} \quad (1A)$$

$$\dot{m}_0 = 0.132902\pi \frac{C_1 {d_0}^2 p_{1_i}}{\sqrt{T_{1_i} + 459.67}} \quad (2A)$$

$$\dot{m}_0 = C A_0 p_t \left\{ \left(\frac{M g_c}{\Re\, T_t}\right)\left(\frac{2k}{k-1}\right) \times \left[\left(\frac{P_0{}^*}{P_t}\right)^{\frac{2}{k}} - \left(\frac{P_0{}^*}{P_t}\right)^{\frac{(k+1)}{k}} \right] \right\}^{1/2} \quad (3A)$$

After determining the mass flow rate in each of the tanks after the first time increment of 0.5 seconds, the program continues to solve for the mass of the air, pressures, and temperatures experienced within both tanks. Through an iterative process within MatLab, the pressures and temperatures that the two tanks experience are graphed across time intervals of 0.5 seconds. The graphs produced through this computational analysis can be seen in Figure 2A.

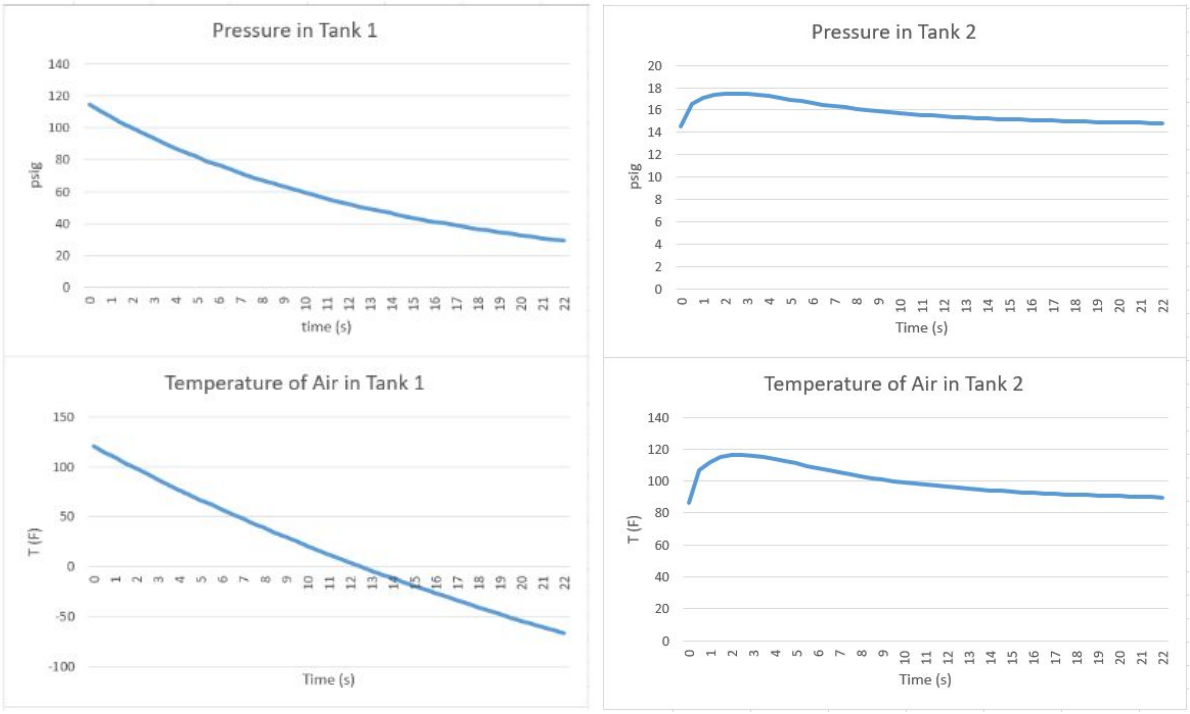

Figure 2A. Matlab Tank Pressures and Temperatures Results

Theoretical ANSYS Simulation

We used ANSYS to simulate the discharge of pressurized air from tank 1 to measure the temperature and pressure in the tank. These measurements will be compared to the experimental and analytical MatLab measurements from the compressible flow lab to determine if an ANSYS Simulation is a viable tool to use when designing a Shock Tube.

ANSYS is a finite element analysis simulation software often used to by engineers to reduce the number of physical prototypes and experiments needed during the design stage. Finite element analysis uses the finite element method to to numerically solve boundary value and partial differential equations. A finite element simulation consists of four basic parts; a base model, a mesh, a setup, and a solution. First a base mode, Figure 3A, is created using a computer aided design program to define the experimental region to be simulated. We used SOLIDWORKS surface modeling to model two tanks and an atmosphere. There is a 0.12 inch opening between tank 1 and tank 2 and a 0.2 inch opening between tank 2 and the atmosphere. There is also a 0.039 inch gap between the individual tanks and the atmosphere to represent the tank wall.

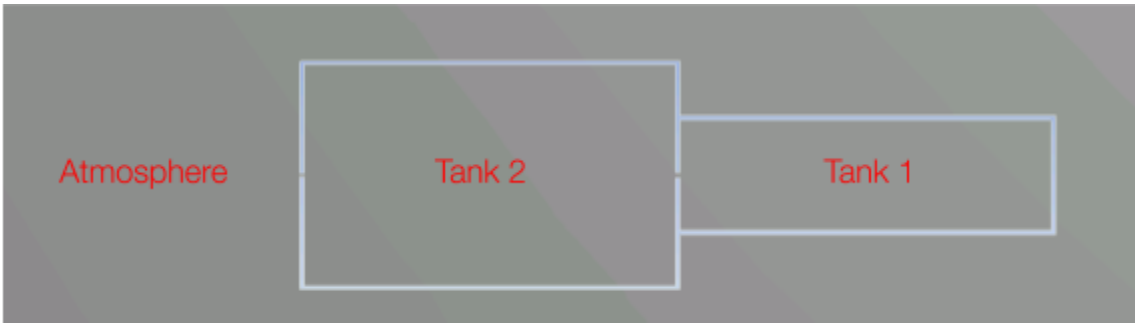

Figure 3A. Compressible Flow Base Model

Second the base model is preprocessed and turned into a mesh, a polygonal representation of the base model consisting of elements and nodes, Figure 4A and 5A. Each cell in the mesh is a local solution to the partial differential equation to be solved, the combination of each individual solution is the solution for the entire mesh. In general, the smaller the individual polygons are in a mesh, or the more dense a mesh is, the higher the accuracy of the simulation will be. However, the higher the density of a mesh, the more computational power required to run the simulation. The mesh in Figure 4A has 50,345 nodes and 49,336 elements with a default element size of 2E-6 m.

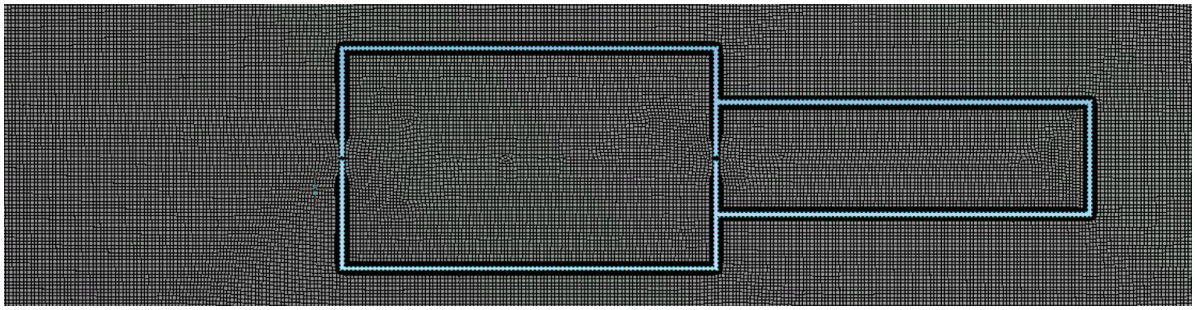

Figure 4A. Complete Compressible Flow Mesh

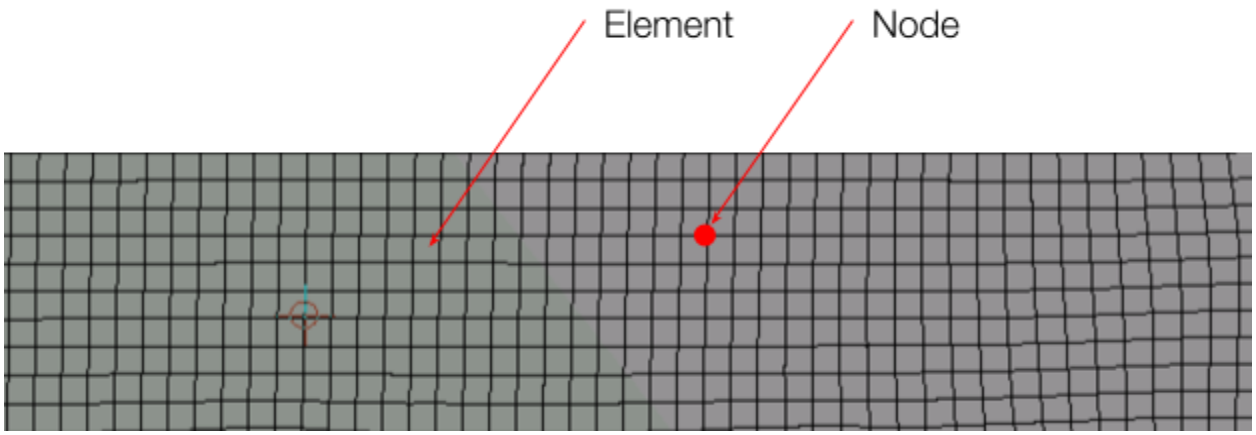

Figure 5A. Zoomed Compressible Flow Mesh

Once preprocessing is completed, the finite element analysis simulation is setup. In this simulation we used ANSYS Fluent, a computational fluid dynamics setup that uses the governing equations to solve fluid flow problems. We used a transient, density-based solver with a realizable k-epsilon energy and a broadband noise source model.

The ANSYS Fluent density-based solver solves the governing equations of continuity, momentum, and energy simultaneously. Each iteration contains four main steps. First the fluid properties of the model are updated based on the current or initialized solution. Second the continuity, momentum, and energy equations are solved simultaneously. Third the equations for scalars, such as turbulence and radiation, are solved for. Finally convergence is checked. Steps one through four are repeated until the convergence criteria of the governing equations are met (Density-Based Solver, 2006).

The realizable k-epsilon model is a turbulent flow model that satisfies the mathematical constraints on the Reynolds stresses (Realizable K-Epsilon Model, 2009). This model is particularly good at representing boundary layers under strong adverse pressure gradients. Equations 4A and 5A are the modeled transport equations for k and epsilon respectively.

$$\frac{\partial}{\partial t}(\rho k) + \frac{\partial}{\partial x_j}(\rho k u_j) = \frac{\partial}{\partial x_j}\left[\left(\mu + \frac{\mu_t}{\sigma_k}\right)\frac{\partial k}{\partial x_j}\right] + G_k + G_b - \rho\epsilon - Y_M + S_k \tag{4A}$$

$$\frac{\partial}{\partial t}(\rho\epsilon) + \frac{\partial}{\partial x_j}(\rho\epsilon u_j) = \frac{\partial}{\partial x_j}\left[\left(\mu + \frac{\mu_t}{\sigma_\epsilon}\right)\frac{\partial \epsilon}{\partial x_j}\right] + \rho C_1 S\epsilon - \rho C_2 \frac{\epsilon^2}{k + \sqrt{\nu\epsilon}} + C_{1\epsilon}\frac{\epsilon}{k}C_{3\epsilon}G_b + S_\epsilon \tag{5A}$$

The Broadband Noise Source Model is used in situations when the sound energy of acoustic waves produced by a turbulent flow are spread out over a range of frequencies. ANSYS Fluent uses Proudman's formula to approximate the measure of the local contribution to total acoustic power per unit volume in a turbulence field (Broadband Noise Source Models, 2006). Equation 6A gives the acoustic power due to isentropic flow in watts per cubic meter where u is the turbulence velocity, l is the length scale, a_0 is the speed of sound, α is a model constant, and ρ_0 is the fluid density. Equation 7A gives the conversion from acoustic power in watts per cubic meter to decibels. In Equation 7A, P_{ref} is the reference acoustic power equal to 10^{-12} watts per cubic meter.

$$P_A = \alpha\rho_0(u^3/l)(u^5/a_0{}^5) \quad (6A)$$

$$L_P = 10log(P_A/P_{ref}) \quad (7A)$$

Conducting Compressible Flow Experiment

In the images below, the tanks that were used for the Compressible Flow Experiment can be seen. As the diagram in Figure 6A demonstrated, the tanks were connected to each other with a hose. The first tank was connected to the wall-pressure source, while the second tank remained open to the atmosphere via a 0.2in diameter nozzle.

Figure 6A. Tanks 1 and 2 (left to right) Used in Compressible Flow Experiment

Tank 1 is a 3 gallon air tank outfitted with an Omega PX181B pressure transducer and a Type T thermocouple. Tank 2 is a 1.5 gallon air tank outfitted with an Omega PX181B pressure transducer and a Type T thermocouple.

Labview data collection began with the valve between Tank 1 and 2 initially closed, and Tank 1 pressurized at an estimated 100 psi. While the program continued to run and collect data, the valve was opened, suddenly releasing the air in Tank 1 as it flowed through the 0.12in opening. Labview recorded the pressures and temperatures of both tanks until the first tank finally reached atmospheric pressure. The pressure and temperature results of the two tanks can be seen in the following Figures.

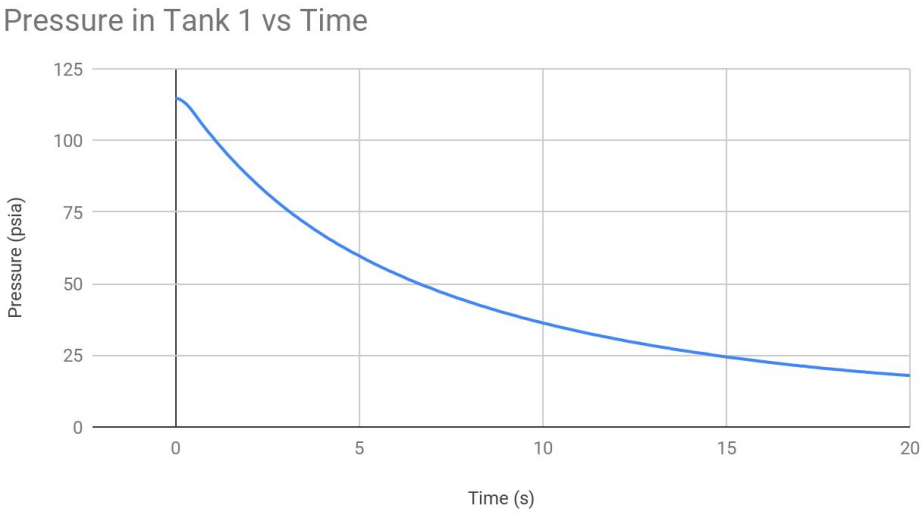

Figure 7A. Compressible Flow Lab - Tank 1 Pressure Results

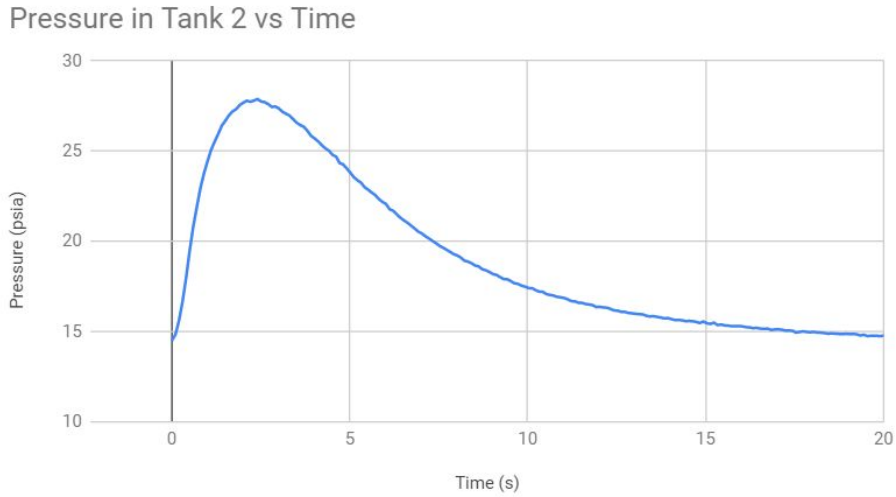

Figure 8A. Compressible Flow Lab - Tank 2 Pressure Results

The primary focus of this experiment was the pressure behavior in tank 1. The pressure results of the computational, theoretical, and physical experiments were graphed against each other for comparison purposes and can be seen below in the following Figure.

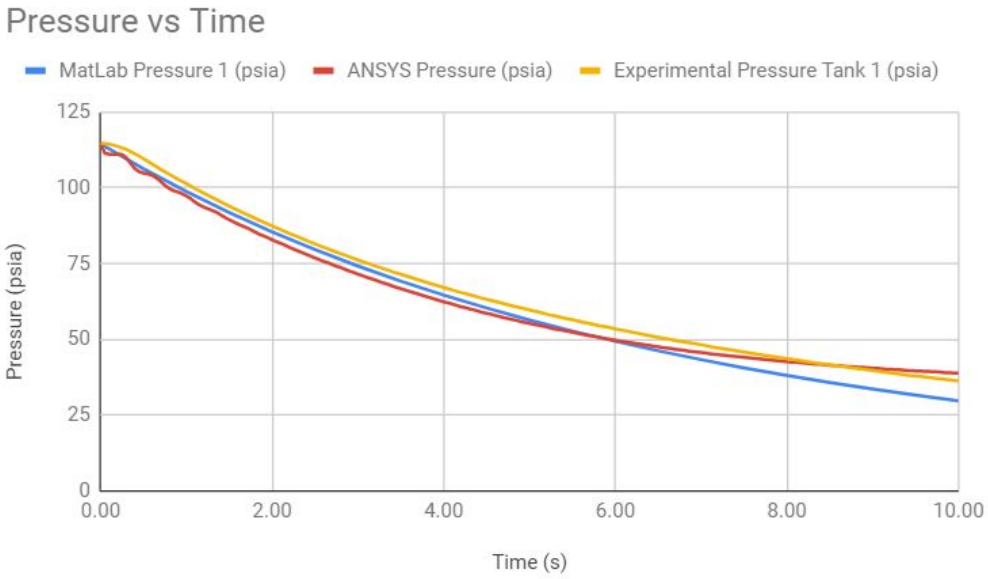

Figure 9A. Tank 1 Pressure Comparison

There were a number of reasons that caused the experimental temperature results to be off from the predicted computational and theoretical results. A primary reason for the differing results was due to the thermocouple placements within the tanks.The thermocouples within both pressure tanks were placed towards the back end of the tanks. With the x and exit nozzles being on the front end of both tanks, the greatest velocity of airflow remained close to a single side of the tank. Because of this, the thermocouple being placed in the most stagnant area of the tank did not allow the a reading of such drastic negative temperatures in the second tank, as the air is coldest at its point of highest velocity. The computational and theoretical results are idealized, so they also do not take into account the mixed air flow that exists within the system or the heat transfer experienced throughout the tanks.

For these reasons, the temperature results were discarded. The primary focus of the experiment was for familiarization with temperature and pressure data acquisition through Labview programming. This experience was obtained, but given the pre-existing tanks at WPI, optimization of the thermocouple placement was not possible, nor was it a focus as this was only for preliminary purposes. The pressure results were satisfactory which demonstrated that a firm understanding in MatLAB, ANSYS Fluent, and general experimental procedure was obtained.

MatLAB Simulation of Compressible Flow

```
%Parametric Evaluation
clc; clear all; close all;

k = 1.4;
M = 28.95;
```

```
Pa = 14.5;
t = 0;
dt = 0.5;
r = 1545.3;
g = 32.2;

fprintf('Please enter the values for the following parameters:\n');

%V1_prompt = 'V1 = ';
%V1 = input(V1_prompt);
%T1i_prompt = 'T1i = ';
%T1i = input(T1i_prompt);
%P1i_prompt = 'P1i = ';
%P1i = input(P1i_prompt);
%d01_prompt = 'd01 = ';
%d01 = input(d01_prompt);
%V2_prompt = 'V2 = ';
%V2 = input(V2_prompt);
%T2i_prompt = 'T2i = ';
%T2i = input(T2i_prompt);
%P2i_prompt = 'P2i = ';
%P2i = input(P2i_prompt);
%d02_prompt = 'd02 = ';
%d02 = input(d02_prompt);
%c_prompt = 'c = ';
%c = input(c_prompt);

V1 = 587.52;
fprintf('V1 = %.6f\n', V1);
T1i = 120.33;
fprintf('T1i = %.6f\n', T1i);
P1i = 114.5;
fprintf('P1i = %.6f\n', P1i);
d01 = .0621;
fprintf('d01 = %.6f\n', d01);
V2 = 884.736;
fprintf('V2 = %.6f\n', V2);
T2i = 86.33;
fprintf('T2i = %.6f\n', T2i);
P2i = 14.5;
fprintf('P2i = %.6f\n', P2i);
d02 = .1248;
fprintf('d02 = %.6f\n', d02);
```

```
c = .67;
fprintf('c = %.6f\n', c);

%loop here
%if (P1i/Pa == 1 && P2i/Pa == 1)
%run_condition = (P1i/Pa >= 1 && P2i/Pa >= 1);

Data = [];

while (round(P2i/P1i,0) == 1 && round(Pa/P2i,0) == 1) == 0

%for t = 0:.5:N
    %t = t + dt;
   % fprintf('t = %.6f\n', t);

    Prc = (2/(k+1))^(k/(k-1));

    A02 = pi*(d02/2)^2;

    A01 = pi*(d01/2)^2;

    %fprintf('Variables solved for along the way:\n');

    m1t = (M/r)*((P1i*V1)/(T1i+459.67))*(1/12);
    %fprintf('m1t = %.6f\n', m1t);

    m2t = (M/r)*((P2i*V2)/(T2i+459.67))*(1/12);
    %fprintf('m2t = %.6f\n', m2t);

    Pr1i = (P2i/P1i);

    %Critical Ratio Comparison
    if Pr1i <= Prc
        mdot01 = 0.132902*pi*((c*(d01)^2*P1i)/(sqrt(T1i+459.67)))
    else
        mdot01 =
(c*A01*P1i*(((M*g)/(r*T1i))*((2*k)/(k-1)))^(1/2))*(((Pa/P1i)^(2/k)-(Pa/P1i)^((k+1)/k))^(1/2));
    end

    m1_1 = m1t-mdot01*dt;
    %fprintf('m1_1 = %.6f\n', m1_1);

    Pr2i = Pa/P2i;
```

```
    %Critical Ratio Comparison
    if Pr2i <= Prc
        m0_2 = 0.132902*pi*((c*(d01)^2*P2i)/(sqrt(T2i+459.67)))
    else
        m0_2 = (c*A02*P2i*(((M*g)/(r*T2i))*((2*k)/(k-1)))^(1/2))*(((Pa/P2i)^(2/k)-(Pa/P2i)^((k+1)/k))^(1/2));
    end

    m2_1 = m2t + (mdot01 - m0_2)*dt;
    %fprintf('m2_1 = %.6f\n', m2_1);

    P1_1 = P1i*(m1_1/m1t)^k;
    %fprintf('P1_1 = %.6f\n', P1_1);

    T1_1 = (T1i+459.67)*(m1_1/m1t)^(k-1);
    %fprintf('T1_1 = %.6f\n', T1_1);

    P2_1 = P2i*(m2_1/m2t)^k;
    %fprintf('P2_1 = %.6f\n', P2_1);

    T2_1 = (T2i+459.67)*(m2_1/m2t)^(k-1);
    %fprintf('T2_1 = %.6f\n', T2_1);

    Pr1_1 = (P2_1/P1_1);

    %Critical Ratio Comparison
    if Pr1_1 <= Prc
        m01 = 0.132902*pi*((c*(d01)^2*P1_1)/(sqrt(T1_1+459.67)))
    else
        m01 =
(c*A01*P1_1*(((M*g)/(r*T1_1))*((2*k)/(k-1)))^(1/2))*(((P2_1/P1_1)^(2/k)-(P2_1/P1_1)^((k+1)/k))^(1/2));
    end

    m1_2 = m1_1-m01*dt;
    %fprintf('m1_2 = %.6f\n', m1_2);

    Pr2_2 = (Pa/P2_1);

    %Critical Ratio Comparison
    if Pr2_2 <= Prc
        mdot02 = 0.132902*pi*((c*(d02)^2*P2_1)/(sqrt(T2_1+459.67)))
    else
```

```
        mdot02 =
(c*A02*P2_1*(((M*g)/(r*T2_1))*((2*k)/(k-1)))^(1/2))*(((Pa/P2_1)^(2/k)-(Pa/P2_1)^((k+1)/k))^(1/2));
    end

    m2_2 = m2_1+(m01-mdot02)*dt;
    %fprintf('m2_2 = %.6f\n', m2_2);

    %fprintf('Solving for those values allowed us to come to this conclusion:\n');

    P1i = P1_1*(m1_2/m1_1)^k
    %fprintf('The pressure of Tank 1 at the second time increment is %.6f psig\n', P1_2);
    T1i = T1_1*(m1_2/m1_1)^(k-1) - 459.67
    %fprintf('The temperature of Tank 1 at the second time increment is %.6f Fahrenheit\n', T1_2);
    P2i = P2_1*(m2_2/m2_1)^k
    %fprintf('The pressure of Tank 2 at the second time increment is %.6f psig\n', P2_2);
    T2i = T2_1*(m2_2/m2_1)^(k-1) - 459.67
    %fprintf('The temperature of Tank 2 at the second time increment is %.6f Fahrenheit\n', T2_2);

    t = t+.5

    Data = [Data; t, P1i, T1i, P2i, T2i];

%     if (P1i/Pa == 1 && P2i/Pa == 1)
%         break
%     end
end
Figure;
subplot(411);plot(Data(:,1),Data(:,2))
title('Pressure in Tank 1 vs. Time')
xlabel('Time (s)')
ylabel('Pressure (psi)')
subplot(412);plot(Data(:,1),Data(:,3))
title('Temp in Tank 1 vs. Time')
xlabel('Time (s)')
ylabel('Temp (F)')
subplot(413);plot(Data(:,1),Data(:,4))
title('Pressure in Tank 2 vs. Time')
xlabel('Time (s)')
ylabel('Pressure (psi)')
subplot(414);plot(Data(:,1),Data(:,5))
title('Temp in Tank 2 vs. Time')
xlabel('Time (s)')
ylabel('Temp (F)')
```

Appendix B: Safety Protocol

HAZARD REVIEW

An analysis of all the ways in which this experiment may cause harm the researchers or lab.

Basic Experimental Procedure:

- A Shock Tube has been created in order to produce an adjustable and reproducible blast to be studied through Schlieren optics techniques. This blast apparatus will ultimately be used by researchers to study the fracture mechanics of biological samples, such as the human Tympanic Membrane. The Shock Tube will be split up into two sections: a driver and driven section, separated by a diaphragm of a chosen material that is expected to rupture within a specified pressure range. The driver section will be pressurized until the predicted rupture of the diaphragm. The rupture of the diaphragm will release the pressure rapidly into the driven section, where it will travel down the remaining two foot length of PVC pipe and release a blast. LabView will be running throughout the production of the blast, and will record once the trigger mechanism is initiated. The trigger mechanism will be initiated when the first dynamic pressure sensor reads above atmospheric pressure. A high speed camera will work to image the blast through the use of Schlieren photography methods, and will also be triggered by the same mechanism that LabVIEW is operating. After analysis is conducted on the overall behavior of the blast, researchers will work to apply the blast on samples. Another high speed camera will be used to image the application of the blast on samples and will be operating off of the same triggering mechanism. Ultimately, researchers hope to develop a blast within the range of Tympanic Membrane rupture, which is estimated to be around 150 dB SPL.

Potential Hazards:

- Desired blast designed for rupture of Tympanic Membrane- posing danger for the researchers conducting the test
    - Double up on ear protection. The researchers in the room will be wearing in-ear protection, in addition to earphones.
- Blast could potentially exceed desired db spl level
    - Researchers will use materials that will slowly work up to higher and higher db spl levels. We will initially use an aluminum sheet of 0.013in thickness which is predicted to rupture at 14.5 psig and create a dB SPL of 185 at peak overpressure (point blank range) and is reduced reduced to 150 dB SPL .5m away. We will continue from there with other materials, slowly escalating the scale of the desired blast. The driving section will not be operated over 14.5 (1 atm) psig.
    - Pressure will no longer be fed from the wall into the driver section. Pressure will be fed from a previously pressurized tank to ease in the monitoring of the supplied pressure. From the tank a pressure regulator will be used, feeding the air into the driver section. The driver section will have a static pressure sensor monitoring the

gradual increase of pressure. The researchers will be monitoring all of these safety-marks to prevent accidental overpressure of the driver section in the case that the diaphragm ruptures at a psi beyond what is expected.

- Recoil of Shock Tube
    - Four pipe clamps have been purchased and will be welded to metal plates. These metal plates will have slots machined along the sides of the clamps, so that they can then be secured onto the optics table. The expected recoil is estimated to be around 15-20 lbs maximum. These clamps are expected to provide more than enough security.
    - No pieces of equipment will be placed in the vicinity to be in any way affected by the unlikely failure of this mounting system.
- Direction of shock
    - The shock will in no way be directed towards any person or piece of equipment (except for the sample that is to be ruptured).

Appendix C: CAD of Diaphragm Mount

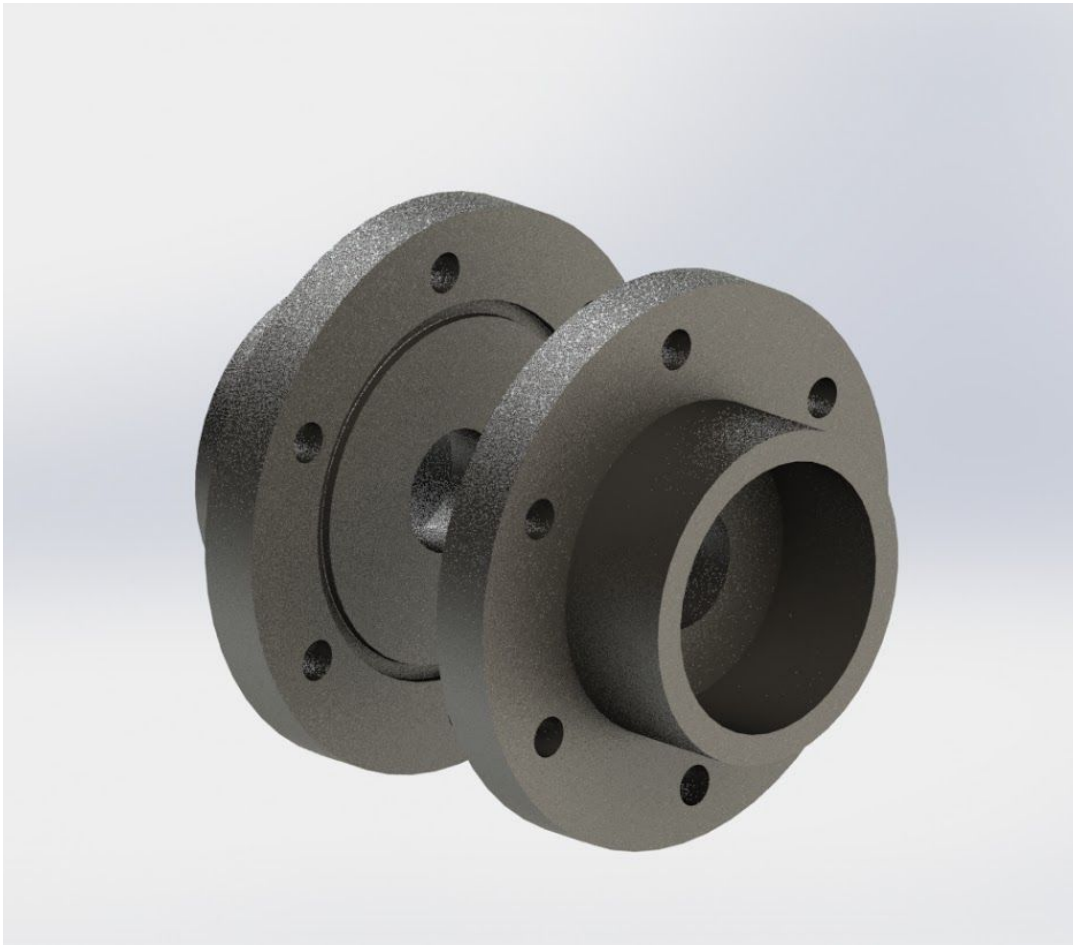

Figure 1C. CAD Render of Custom Diaphragm Mount

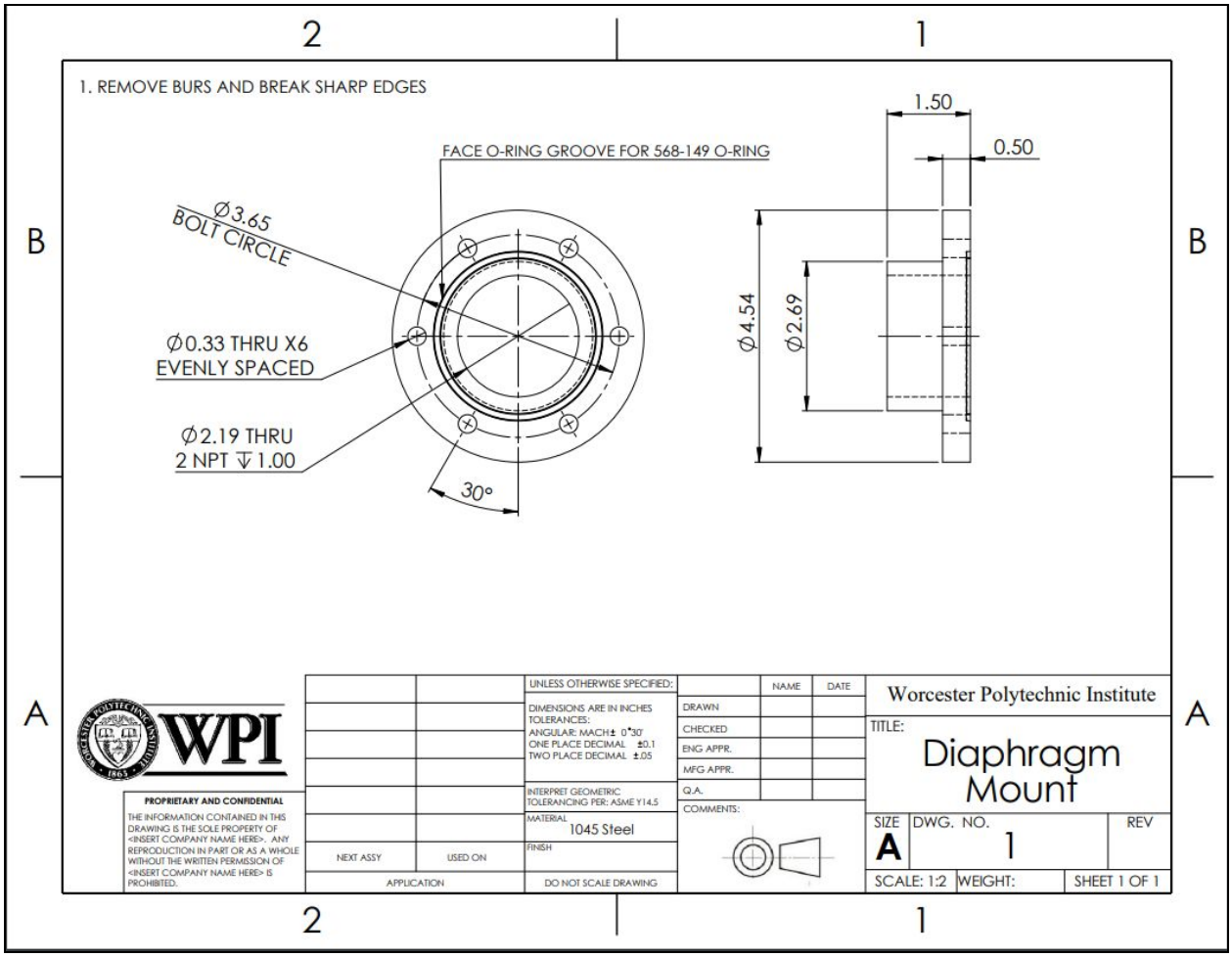

Figure 2C. Diaphragm Mount Machine Drawing

Appendix D: Diaphragm Insertion Instructions

1. Cut a piece of diaphragm material large enough to cover the entire surface of the flange opening, approximately 4in by 4in, as seen in Figure 1D.

Figure 1D. Diaphragm Material Square

2. Loosen and remove the bolts holding the driving section of the Shock Tube to the T-slotted framing to open the flange.
3. Slide the driving section of the Shock Tube back, as seen in Figure 2D.

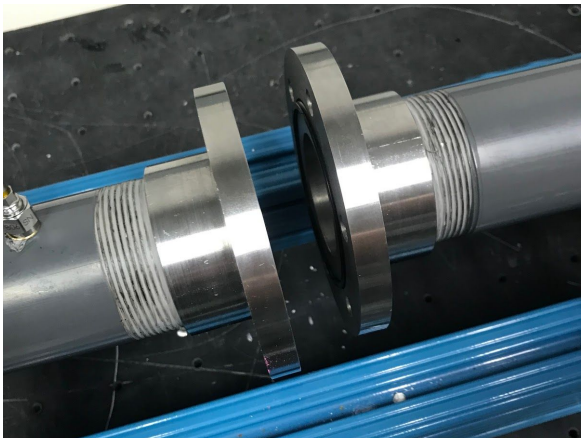

Figure 2D. Separated Driving and Driven Section

4. Insert the O-Ring into one side of the flange, as seen in Figure 3D.

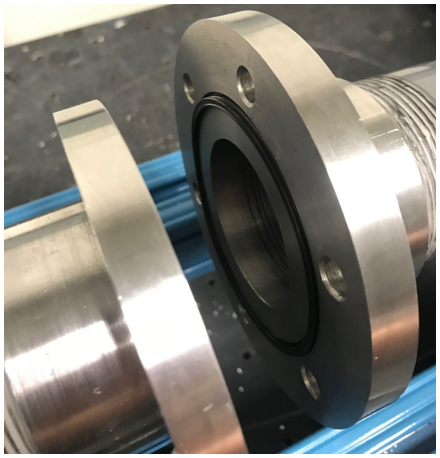

Figure 3D. O-Ring Insertion

5. Insert the diaphragm material.
6. Slide the flange together with the diaphragm material in place.
7. Insert the 6 screws into the holes in the flange, as seen in Figure 4D.

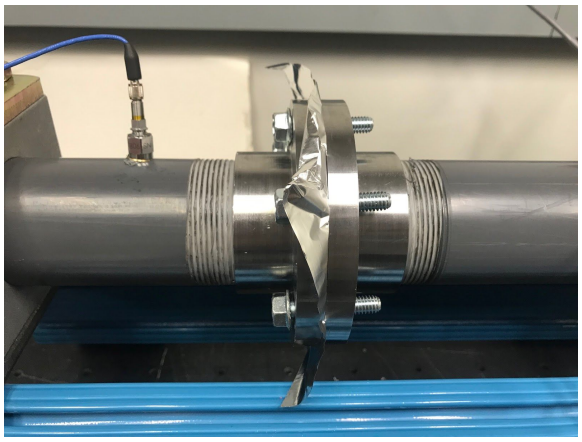

Figure 4D. Screw Insertion

8. Secure the screws in place with nuts.
9. Torque each screw to the same value. We used 120-130 in-lbs, as demonstrated in Figure 5D.

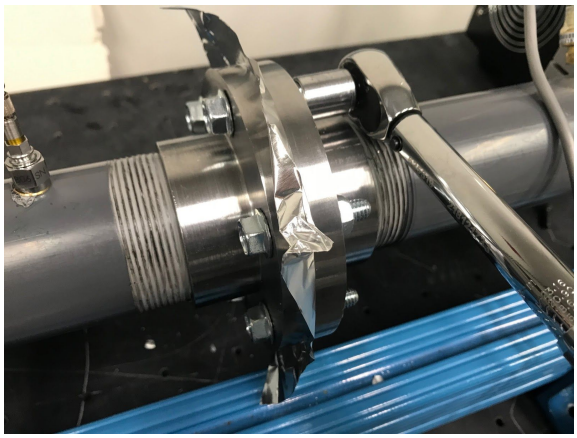

Figure 5D. Utilization of Torque Wrench

10. Secure the Shock Tube to the T-slotted framing.
11. After bursting the diaphragm, undo the nuts and remove the screws.
12. Remove the burst diaphragm.

Appendix E: LabVIEW of Pressure Calibration

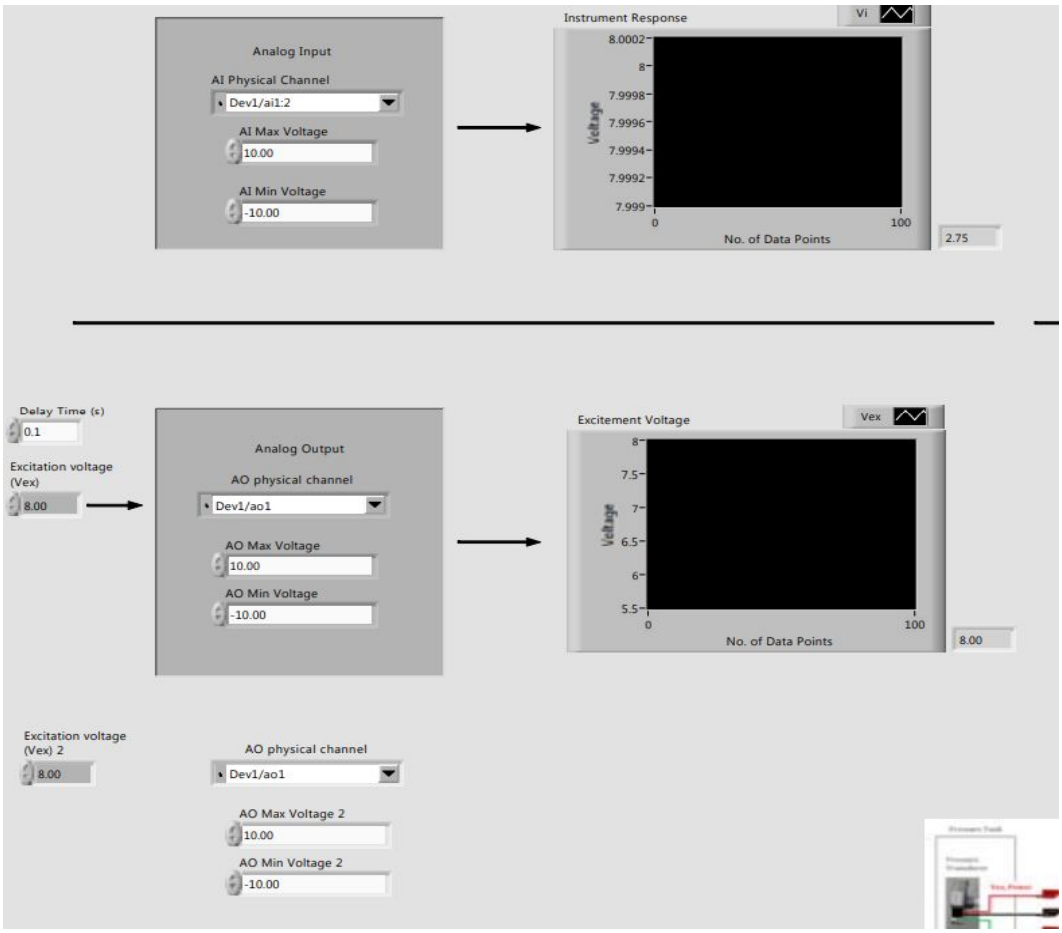

Figure 1E. Front Panel VI Channel Assignment for Static Pressure Transducer

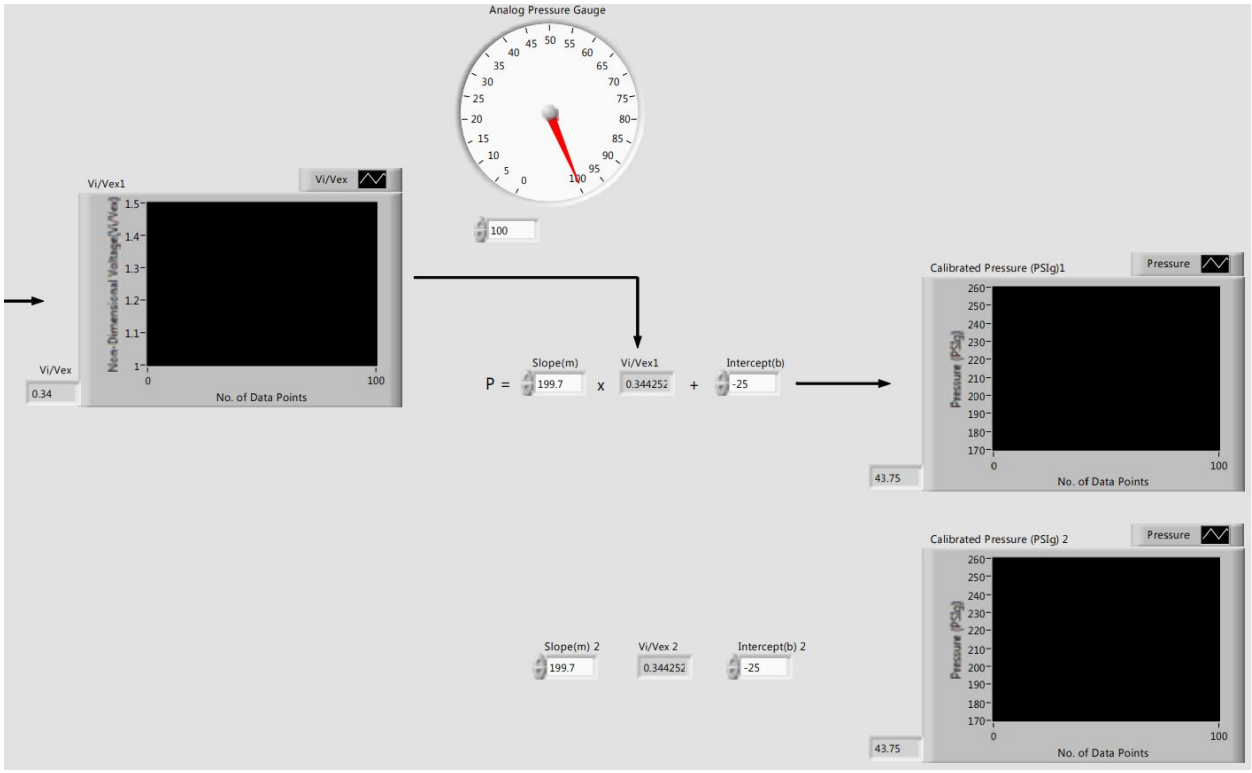

Figure 2E. Front Panel VI Slope Intercept Calibration

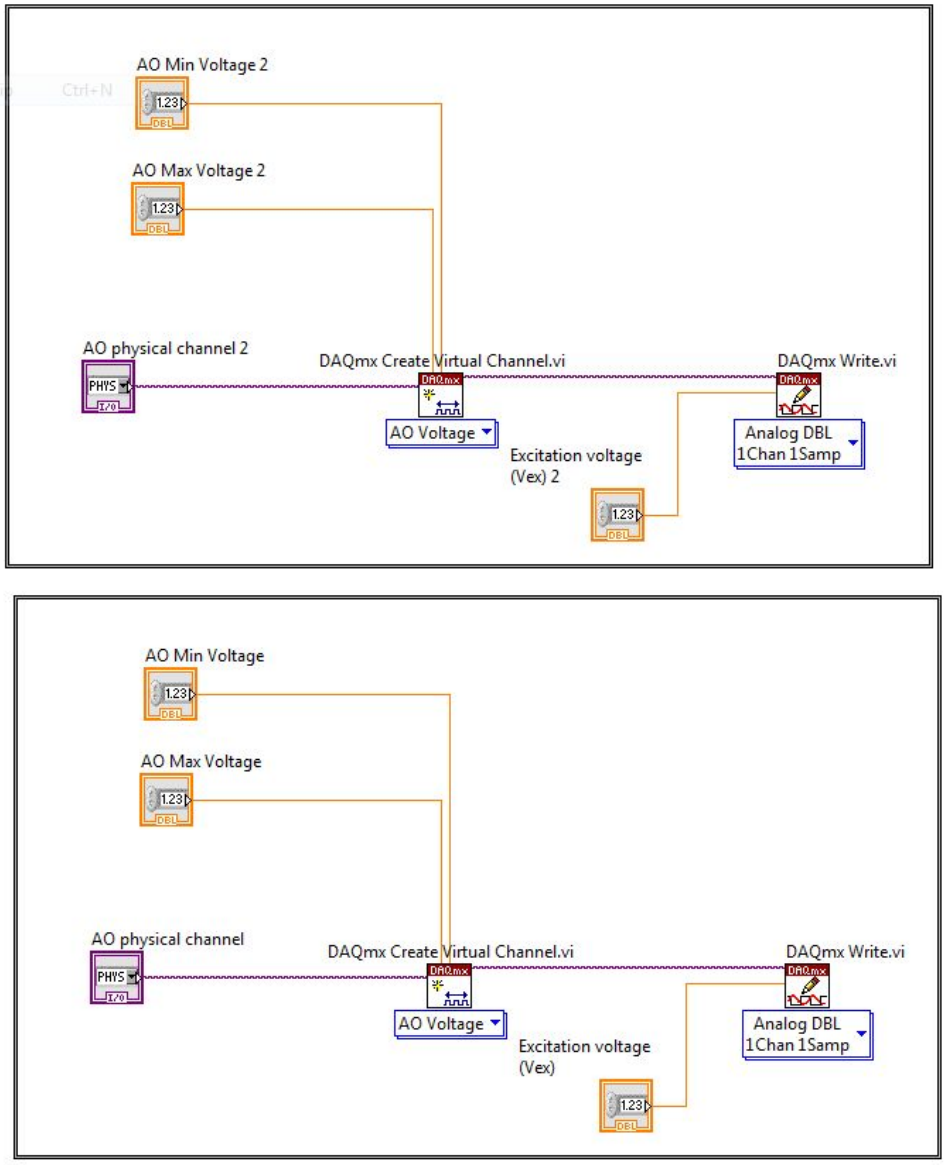

Figure 3E. BD Output Channels for Static Pressure Calibration

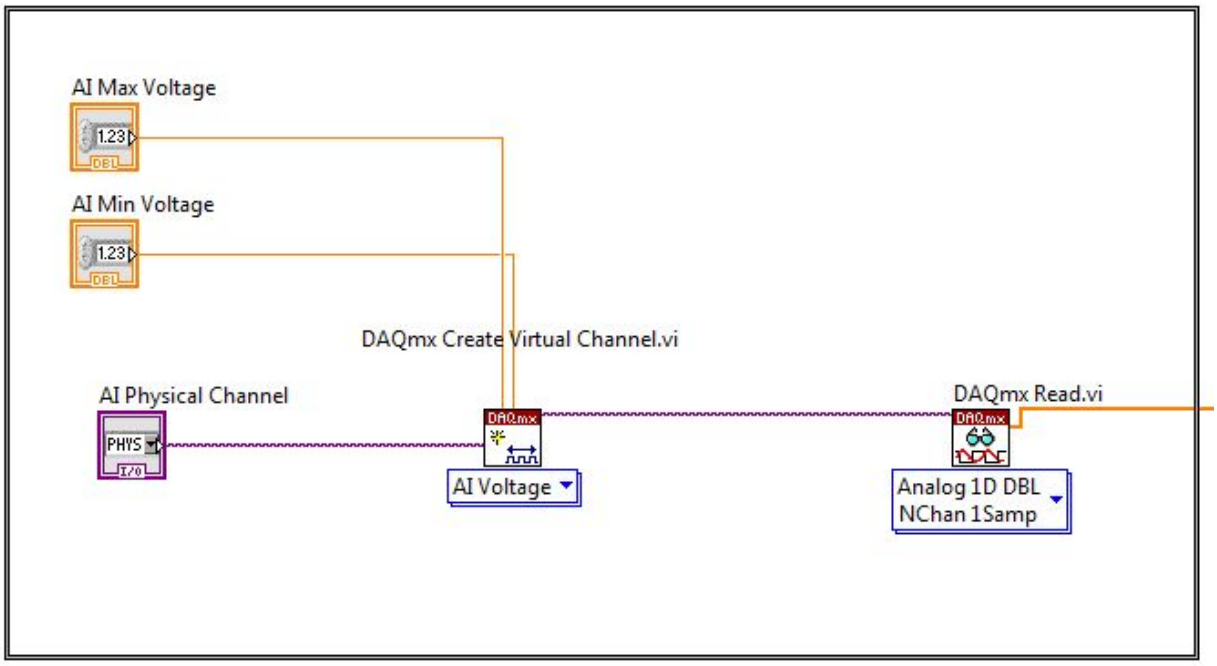

Figure 4E. BD Input Channels for Static Pressure Calibration

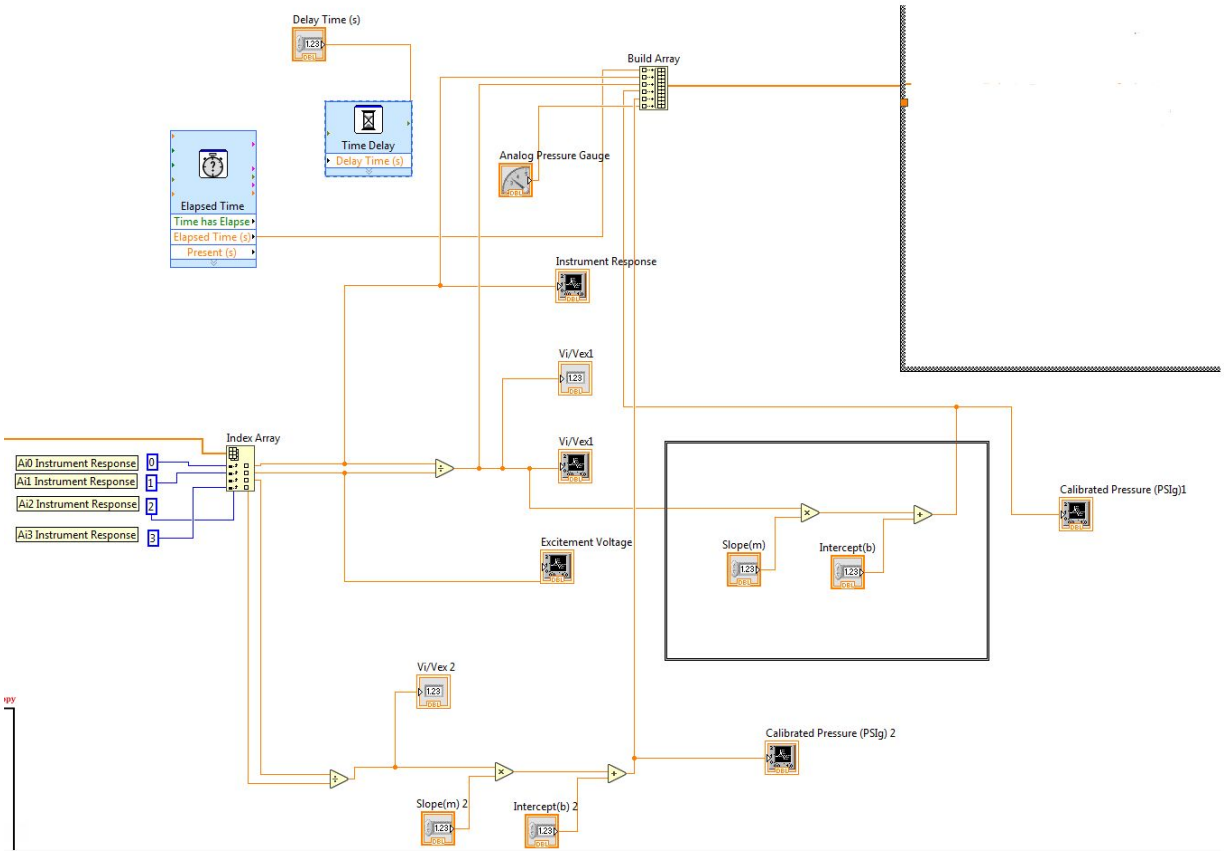
Delay Time (s)
Time Delay
Delay Time (s)
Elapsed Time
Time has Elapse
Elapsed Time (s)
Present (s)
Build Array
Analog Pressure Gauge
Instrument Response
Vi/Vex1
Vi/Vex1
Index Array
Ai0 Instrument Response
Ai1 Instrument Response
Ai2 Instrument Response
Ai3 Instrument Response
0
1
2
3
Excitement Voltage
Slope(m)
Intercept(b)
Calibrated Pressure (PSIg)1
Vi/Vex 2
Calibrated Pressure (PSIg) 2
Slope(m) 2
Intercept(b) 2

Figure 5E. BD

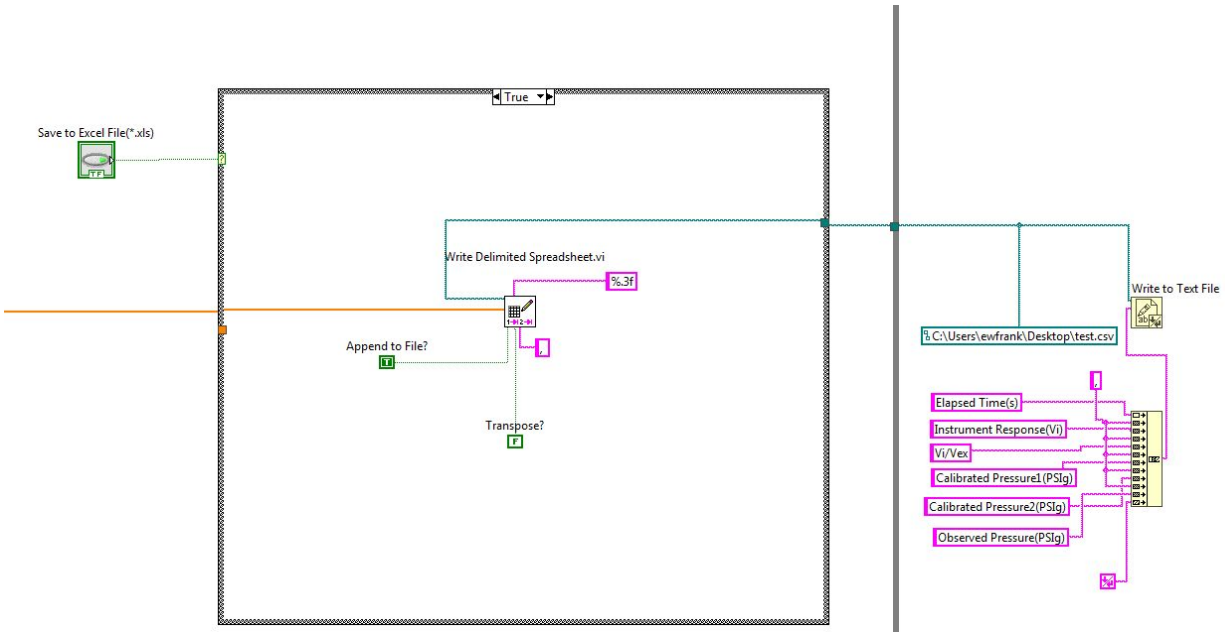

Figure 6E. Writing File

Appendix F: Shock Tube Labview Code

The camera trigger Labview, Figure 1F, was used to record and export the pressures values of P1-P4 and trigger a Photron camera based voltage level of P2. The voltage trigger level can be controlled through user input. If the P2 voltage is below the voltage trigger level, the false case structure shown in Figure 2F is executed and there is no voltage output to the trigger of the Photron camera. If the P2 voltage is above the voltage trigger level, the true case structure shown in Figure 2F is executed and a 5 volt DC pulse is outputted to the trigger chanel of the Photron camera.

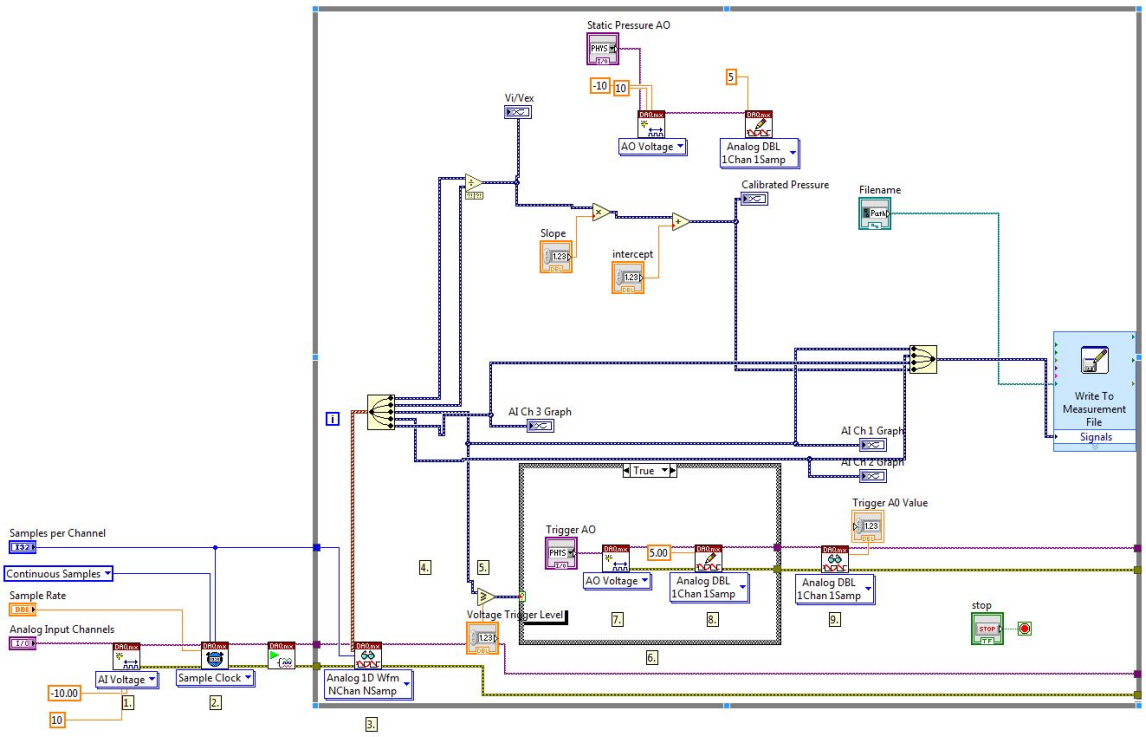

Figure 1F. Camera Trigger Labview

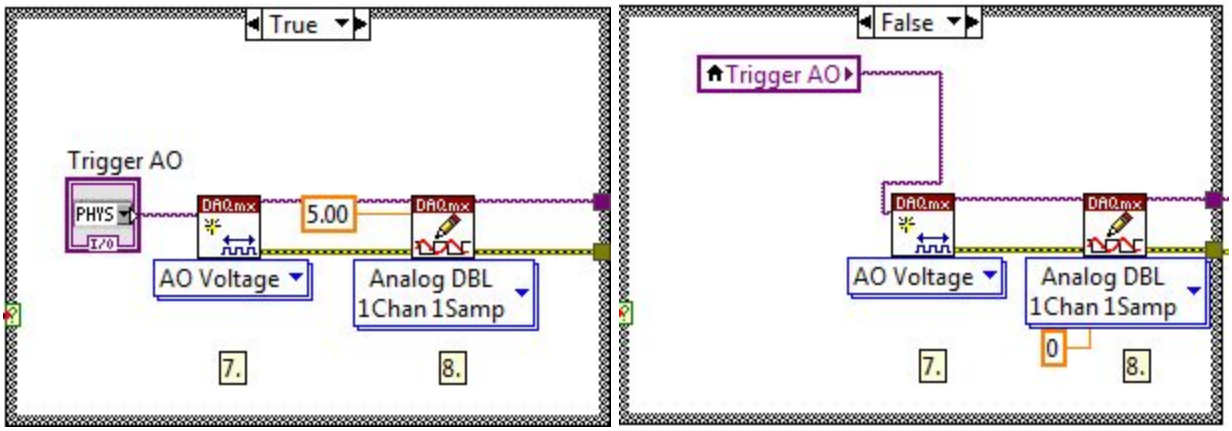

Figure 2F. Detailed case structure True False

The high sampling rate Labview, Figure 3F and 4F, was used to record and export the pressure values of two analog input channels at a high sampling rate.

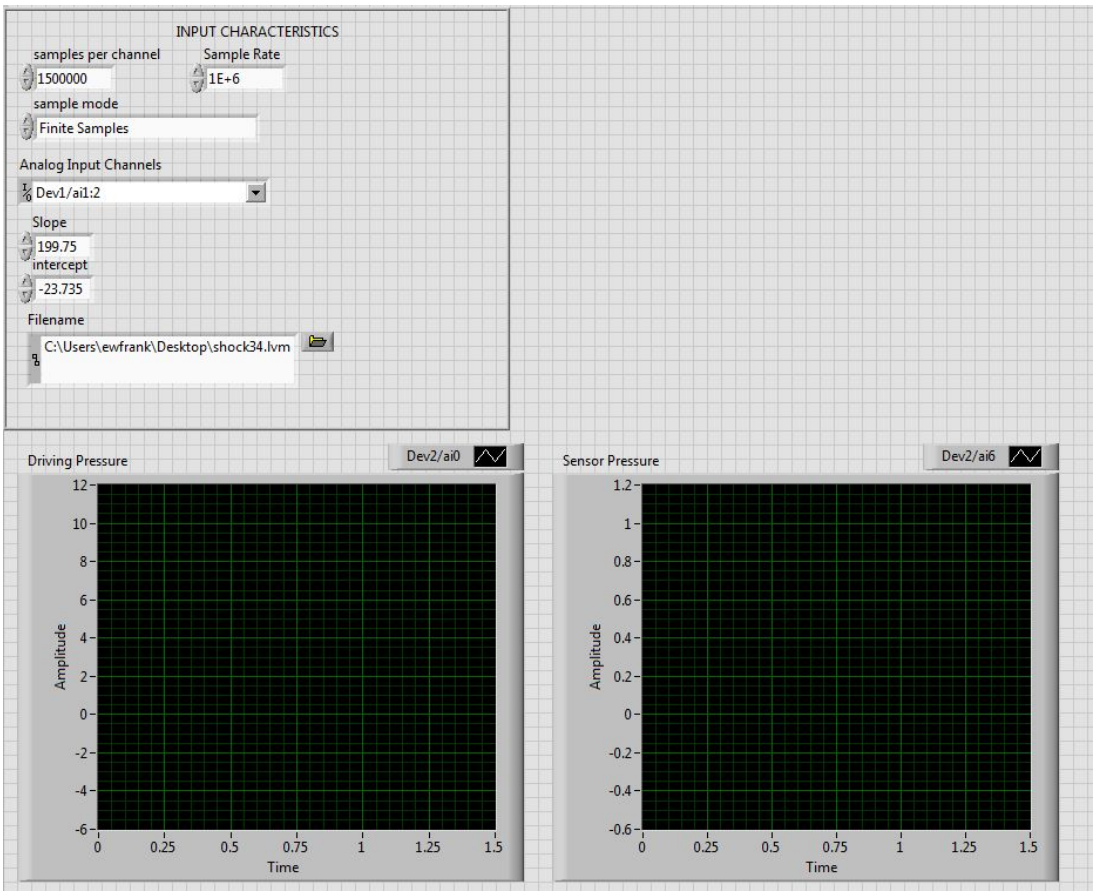

Figure 3F. High Sampling Rate Labview Front Panel

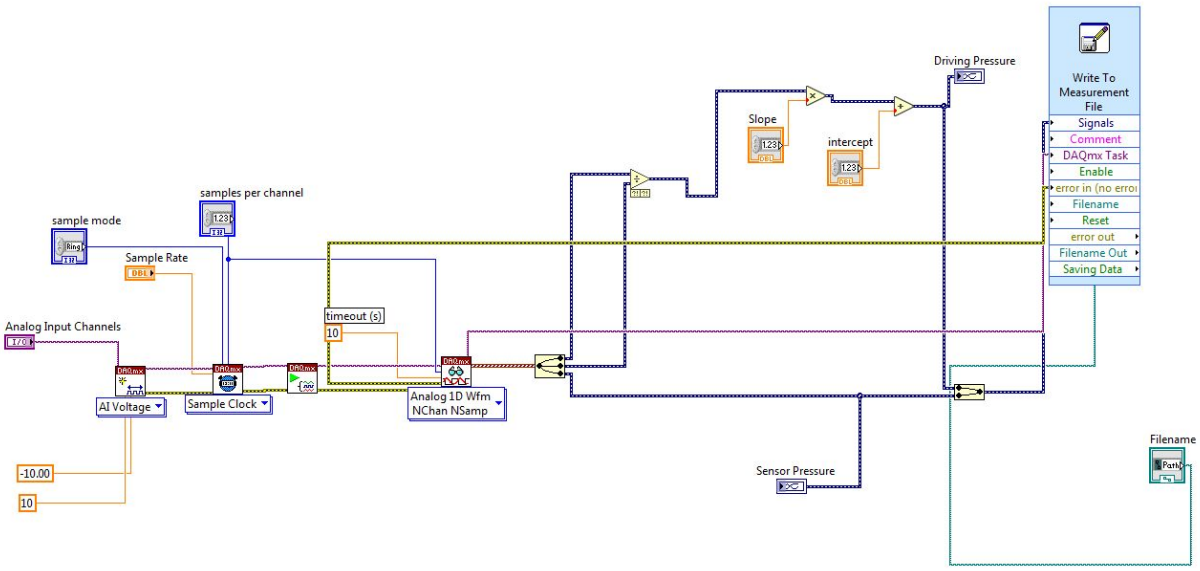

Figure 4F. High Sampling Rate Labview Block Diagram

Appendix G: Operating Procedure

The experimental operating procedure is separated into five sections: Data Acquisition, Shock Tube, Schlieren Imaging, Rupture Imaging, and Experimental. Once the five systems are in place, experiments may take place.

Data Acquisition

1. Connect High Speed Camera trigger channel and pressure sensors (P1-P4) to the NI DAQ as detailed in section 3.5.1.
2. Turn on PCB signal conditioner and NI DAQ
3. Open Labview program and enter in user inputs described in section 3.5.2.
4. Connect High Speed Camera to computer
5. Turn on High Speed Camera
6. Open PFV software and enter user inputs described in section 3.5.2.

Schlieren Imaging (Detailed in sections 3.1 and 3.5.2)

1. Determine the focal length of the spherical mirror that will be used for Schlieren
2. Once the mirror is placed in desired position, orient the high speed camera so that it is twice the focal length away from the mirror
3. Place a sharp knife edge in front of the camera
4. Place a point light source next to the camera so that the light hits the mirror, focuses on the knife edge, and passes into the center of the camera
5. Connect camera to Photron PFV software and the analog trigger (TT1) to the DAQ
6. Use the PFV software to adjust to desired shading, frame rate, shutter speed, and resolution.

Rupture Imaging

1. Place the sample at desired distance outside of the Shock Tube

2. Orient and focus the High Speed Camera on the sample

Experimental Procedure

1. For each run, insert a diaphragm into the flange of the shock tube following the procedure detailed in Appendix D
2. Fill pressure holding tank
3. Put PFV in endless recording mode
4. Simultaneously start Labview program and open ball valve connected to the pressure holding tank
5. After rupture, stop data acquisition
6. Analyze data